1994

The Initial Interaction Of Water Vapour With Magnesium And Magnesium Alloy Surfaces

Steven Joseph Splinter

THE INITIAL INTERACTION OF WATER VAPOUR WITH MAGNESIUM AND MAGNESIUM ALLOY SURFACES

by

Steven Joseph Splinter

Department of Materials Engineering
Faculty of Engineering Science

submitted in partial fulfillment
of the requirements for the degree of
Doctor of Philosophy

Faculty of Graduate Studies
The University of Western Ontario
London, Ontario
March 1994

ISBN 0-315-90582-4

ABSTRACT

The initial interaction of water vapour with polycrystalline magnesium and magnesium alloy surfaces has been quantitatively followed from the earliest stage using Auger electron spectroscopy (AES) and X-ray photoelectron spectroscopy (XPS). The fitting of AES data to theoretical models suggested that a three-stage oxidation behaviour was operative on pure Mg surfaces: (1) dissociative chemisorption during doses up to $\approx$ 0.7 langmuir (L) (1L = 1.3×10^{-4} Pa·s); (2) oxide nucleation and growth which is complete by $\approx$ 5L at an average island height of four monolayers; and (3) bulk thickening after coalescence of the oxide islands. The bulk thickening stage was adequately described by a logarithmic-type growth law and was found to be controlled by the movement of metal cations from the metal/oxide interface to the oxide/gas interface. Hydrogen (deuterium) was determined by nuclear reaction analysis (NRA) to be present in the film only in small relative amounts.

The effect of Ar^+ ion bombardment on the interaction of water with pure Mg surfaces was systematically studied by AES. The effect was most pronounced for the oxide nucleation and growth stage. The dissociative adsorption and bulk thickening stages were only weakly affected by prior ion bombardment. The results have been interpreted based on the assumption of competition between the effects of radiation defects (vacancies, vacancy clusters, dislocation loops) and implanted argon atoms on the oxidation process.

Water interactions with Mg-Al alloy surfaces (Mg-3.0Al, Mg-8.5Al) resulted in

enhanced oxide nucleation and growth at low exposures as compared to pure Mg. At longer exposures, Al^{+3} cations were incorporated into the growing oxide, resulting in a pronounced decrease in the rate of bulk oxide thickening.

Water adsorption and oxide growth on dilute Mg-Fe alloy surfaces (120 to 700 wt ppm) was shown to be retarded during the very early stages. The growth rate at longer exposures was unaffected by the iron content. Segregation of iron into the oxide film was, however, detected by static secondary ion mass spectrometry (SSIMS). Finally, the saturated oxide films formed on Fe-containing magnesium specimens were shown by XPS to be more "defective" than those formed on pure magnesium.

ACKNOWLEDGEMENTS

I would like to express my deepest gratitude to my advisor and mentor, Dr. Stewart McIntyre, for his guidance, support and encouragement during the course of my academic tenure at Western. Stewart allowed me the intellectual freedom to pursue curiosity-driven research while providing the advice and direction necessary to maintain a clear path towards a practical goal. It has been both a pleasure and an honour to have worked with him.

To my wife, Liisa, I extend my most heart-felt appreciation and adoration. She is a kindred spirit whose path in life is inexorably linked to my own.

I would like also to personally thank each member of Surface Science Western. It is certain that, at one time or another, everyone has helped me in some way. Special thanks are, however, extended to Suzanne Hicks and Sue Brown for their tireless administrative assistance, to Gary Good and Dietmar Fichter for their invaluable technical assistance in numerous matters, and to Sridhar Ramamurthy, Gary Mount, Igor Bello, Leo Lau, Liji Huang and Paul van der Heide for their assistance and advice in all matters scientific.

To my fellow graduate students, past and present, thank you all very much. Extra special thanks are extended to Wayne Chang, Shifeng Lu, Perry Spevack and Jay Mycroft for befriending me in my early days at Surface Science. I will always remember meals in the hospital cafeteria, although perhaps with more fondness than is rightly justified.

I would like to thank Dr. Vesna Mitrovic-Scepanovic and the Metals Technology Laboratories (MTL) of the Canada Centre for Mineral and Energy Technology (CANMET), for supplying all of the materials used in this thesis. I also thank Dr. Keith Griffiths and Dr. Willy Lennard of Interface Science Western for their capable help in performing and interpreting the NRA experiments and Dr. Gino Palumbo of the Ontario Hydro Research Laboratories in Toronto for his help in collecting and interpreting the EBSD patterns.

Finally, I wish to thank Surface Science Western for financial support in the form of a Research Assistantship, the Department of Materials Engineering for support in the form of several Teaching Assistantships and the Faculty of Graduate Studies of the University of Western Ontario for support in the form of a Graduate Research Award and a Graduate Research Fellowship.

"They may say what they like; everything is organized matter"

-Napoleon Bonaparte
(1769-1821)

TABLE OF CONTENTS

LIST OF FIGURES

LIST OF TABLES

CHAPTER 1

INTRODUCTION

Magnesium was first isolated by Davy in 1808, yet it remained a laboratory curiosity until the early 1920's when practical melting and refining techniques became available [1.1]. Magnesium occurs as dolomite ores and in brine and sea water and is the sixth most abundant element in the earth's surface. It is extracted commercially either by the thermal reduction of calcined dolomite (the Pidgeon process) or by the fused salt electrolysis of either hydrous or anhydrous magnesium chloride. Until recently, Canada had only one primary magnesium producer, the small Timminco plant in Haley, Ontario. However, the recent start-up of Norsk-Hydro's Bécancoeur, Quebec and Magcan's High River, Alberta facilities have transformed Canada into a major magnesium producer. In fact, if Norsk-Hydro and Magcan's ambitious expansion plans are realised, Canada could easily become the world's largest single producer.

World production of magnesium in 1989 exceeded 250,000 tonnes [1.2]. The largest share of the world magnesium market (more than half of the total production) comes from the aluminum industry, where it is used as an alloying element to increase the tensile strength, hardness and weldability of aluminum-base alloys. A further 50,000 tonnes is employed in various chemical applications, including use as a desulphurising agent in the production of steel, copper and nickel alloys and as a reducing agent to produce zirconium and titanium metal (the Kroll process). Of the remainder, the largest single use is in magnesium-base structural engineering alloys.

Magnesium is by far the lightest of the commonly available metals, thus making magnesium-base alloys extremely attractive for engineering applications where light weight is important (e.g. aerospace industries, transportation industries). In fact, magnesium alloys are similar in weight to many engineering plastics, yet they possess greater stiffness, impact resistance, dimensional stability and machinability. In addition, the weight advantages of magnesium are further enhanced by its very high strength-to-weight ratio [1.3]. Despite their competitive mechanical properties, however, magnesium alloys remain among the lesser members of the metals family in terms of world consumption. This is partially due to the fact that there has traditionally not been a strong pro-magnesium lobby to counteract the promotion that aluminum, zinc and plastics have enjoyed. This situation is rapidly being corrected, however, under pressures from such bodies as the International Magnesium Association (IMA), the European Magnesium Research Association (EEIG) and the Institute of Magnesium Technology, which opened in Quebec as recently as September, 1990. These associations are actively striving to make the benefits of magnesium alloys more widely known.

The principal challenge to the widespread use of magnesium alloys in engineering applications is their need for improved corrosion resistance. Magnesium sits at the extreme anodic end of the galvanic series [1.4] and is thus the most active of all the structural metals. The development of more corrosion-resistant alloys has been directed mainly towards the processing of high-purity alloys with heavy metal contaminants (e.g. iron, nickel and copper) below certain tolerance limits in order to avoid micro-galvanic effects due to the presence of cathodic second phases [1.5]. Additions of aluminum and

manganese have improved the tolerance limits and, in addition, improved corrosion resistance has been reported in Mg-Al base alloys [1.6,1.7]. Nevertheless, the mechanisms and limits of these improvements are poorly understood. It is clear, therefore, that fundamental research is needed to understand the significance of alloying constituents for the corrosion of magnesium alloys.

1.1 Scope of the present investigation

The resistance of a metal to attack by aggressive solutions or gases is primarily related to the protective properties of the surface oxide film. In order to control these properties to impart optimum corrosion/oxidation resistance to a given material, it is necessary to know the mechanisms and processes underlying the growth of the film itself. The extreme complexity of these processes has prevented thus far the development of a general theory capable of predicting *a priori* the optimum alloy composition for a given service condition. Nevertheless, significant progress is being made towards developing a more fundamental understanding of these processes, particularly through the use of modern surface analytical techniques and associated ultra-high vacuum (UHV) technology. In recent years a vast number of studies have been devoted to understanding the adsorption of oxygen and water on metal surfaces, the development of two-dimensional adsorption structures and the bonding state of oxygen and water on many pure metal and alloy systems [1.8, 1.9]. Less is known about the nucleation of surface oxide; even the role of surface defects is not clear. For the case of alloy oxidation, it

is the nucleation and subsequent growth of oxide that is very important for controlling corrosion processes and the formation of protective layers. For example, at a recent international workshop dealing with critical issues concerning high temperature corrosion [1.10], there was agreement among the panel of leading corrosion scientists from Europe and North America that it is the *initial* stages of reaction between oxygen and water and metal surfaces, especially the nucleation of surface oxide, that are of fundamental importance in many cases for the ultimate structure and protectiveness of the films.

In this thesis, the initial stages of oxide formation occurring on polycrystalline magnesium and magnesium alloy surfaces exposed to low partial pressures of water vapour at room temperature have been examined in detail. Various surface analytical techniques have been employed, including: Auger electron spectroscopy (AES); X-ray photoelectron spectroscopy (XPS); nuclear reaction analysis (NRA) and secondary ion mass spectrometry (SIMS). The technological significance of such a study is clear based on the above discussion. It should be pointed out, however, that the interaction of water vapour with magnesium surfaces is also of significant scientific interest in its own right. Magnesium is a simple metal (i.e. no d electrons) and can be considered as one of real life's closest approximations to the theoretical *jellium* wherein positive ions are embedded in a Fermi sea of conduction electrons [1.11]. The H_2O-Mg interaction should therefore represent a relatively simple system and may contribute to the understanding of water-surface interactions in general. Such interactions are of fundamental importance to the understanding of corrosion-passivation chemistry, electrochemistry and heterogeneous catalysis [1.9].

The thesis is structured as follows: Chapter 2 outlines the experimental methods used throughout this study. The results obtained from a study of the initial interaction of water vapour with pure magnesium surfaces are then presented in Chapter 3. Chapter 4 describes the results of a systematic investigation of the effects of Ar^+ ion bombardment on the initial reaction of water with pure magnesium surfaces. It was important to understand the effects of inert gas ion bombardment on the initial oxidation processes in order to facilitate comparison with magnesium samples containing very low-level alloying elements, for which no post-sputtering annealing stage was desirable. The results were, moreover, of more general interest to the understanding of the role of point defects and defect clusters on oxide growth. The room temperature interaction of water vapour with two Mg-Al alloy surfaces, Mg-3.0wt% Al and Mg-8.5wt%Al, is described in Chapter 5. Chapter 6 concerns the effect of very low concentrations of iron (120 to 700 ppm by weight) on the early stages of oxide growth. Finally, a summary of all the results obtained is presented in Chapter 7.

References

[1.1] G.V. Raynor, The physical metallurgy of magnesium and its alloys (Permagon Press, New York, 1959).

[1.2] P.D. Caton, Materials and Design 12 (1991) 309.

[1.3] E.F. Emley, Principles of Magnesium Technology (Permagon Press, New York, 1966).

[1.4] M.G. Fontana and N.D. Greene, Corrosion Engineering, 2nd Edition (McGraw-Hill, New York, 1978).

[1.5] J.D. Hanawalt, C.E. Nelson and J.A. Peloubet, Trans. AIME 147 (1942) 273.

[1.6] C.B. Baliga and P. Tsakiropoulos, in E.W. Lee and N.J. Kim (Eds.), Lightweight Alloys for Aerospace Applications II (TMS, Warrendale, 1991) p.439.

[1.7] G.L. Makar, J. Kruger and A. Joshi, in H. Paris and W. Hunt (Eds.), Proc. Advances in Magnesium Alloys and Composites (TMS, Phoenix, 1988) p.105.

[1.8] G.A. Somorjai, Chemistry in two dimensions: surfaces (Cornell University Press, Ithaca, 1981).

[1.9] P.A. Thiel and T.E. Madey, Surf. Sci. Rep. 7 (1987) 211.

[1.10] A. Rahmel, G.C. Wood, P. Kofstad and D.L. Douglass, Oxid. Met. 23 (1985) 251.

[1.11] S.A. Flodström, L.G. Petersson and S.B.M. Hagström, J. Vac. Sci. Technol. 13 (1976) 280.

CHAPTER 2

EXPERIMENTAL METHODS

2.1 Introduction

The following section outlines the experimental methods used in this study. The level of detail is intended to provide sufficient information in order to adequately understand the experimental results. Any variations from the general descriptions given here will be discussed in Chapters 3 to 6, as required. In describing the analytical methods employed, attention is focussed primarily on Auger electron spectroscopy (AES) and X-ray photoelectron spectroscopy (XPS), since these techniques account for the bulk of the experimental results obtained. Less attention is correspondingly afforded to nuclear reaction analysis (NRA) and secondary ion mass spectrometry (SIMS).

2.2 Vacuum Considerations

In order to investigate adequately the very early stages of the interaction of water vapour with magnesium and magnesium alloy surfaces, ultra-high vacuum (UHV) is required. This vacuum requirement arises from the need to maintain a clean surface prior to performing a controlled experiment. According to the elementary kinetic theory of gases, the flux of molecules of mass m striking a surface is given by:

$$Q = \frac{P}{(2\pi mkT)^{1/2}} \qquad (2.1)$$

where Q is the flux of impinging molecules (collisions/cm^2/s); P is the pressure (Pa); k is Boltzmann's constant and T is the temperature (K). For example, if we consider that water is a common residual gas in UHV systems, then the flux of water molecules striking the surface at 298 K is found to be:

$$Q = (3.60\times10^{18})\cdot P \qquad (collisions/cm^2/s) \qquad (2.2)$$

Now, if it is assumed that every molecule that strikes the surface sticks (i.e. the sticking coefficient is unity), then a partial pressure as low as 3.1×10^{-4} Pa would result in an accumulation of water, in one second, equal to the surface atom density of magnesium, $\approx 1.1 \times 10^{15}$ atoms/cm^2. The surface would thus be completely contaminated. The time to contamination can, however, be extended to almost one hour by reducing the partial pressure, P, to below 1×10^{-7} Pa. This is generally sufficient time to perform measurements on freshly cleaned surfaces.

2.3 Sample Preparation

Polycrystalline magnesium substrates of 99.997 at% nominal purity and of rectangular shape ($\approx$ 10 × 10 × 2 mm) were used throughout the study. The specimens were provided by the Metals Technology Laboratories (MTL) of the Canada Centre for Mineral and Energy Technology (CANMET), Ottawa, Ontario. Table 2.1 shows the major impurities in atomic parts per million (ppma), determined by spark source mass spectrometry.

Table 2.1: Major impurities in magnesium specimens.

Element	B	N	O	F	Al	Si	P	S	Cl
Conc. (ppma)	0.3	2	6	< 2	3	5	0.2	0.3	0.8
Element	K	Ca	V	Mn	Fe	Zn	Ga	As	Y
Conc. (ppma)	0.1	0.2	0.3	0.3	4	3	0.2	0.3	0.1

The samples were mechanically polished to a 0.05 μm Al_2O_3 finish and degreased ultrasonically before being mounted in a Perkin-Elmer PHI-600 scanning Auger microprobe (SAM) (see section 2.6.1). The base pressure of the SAM was approximately 1 × 10^{-7} Pa. Auger spectra of the specimen surfaces as mounted showed the presence of carbon and oxygen as the principal contaminants. Surface cleaning in

vacuum was achieved by sputtering with 3 keV Ar^+ ions, having a current density of ≈ 16 $\mu A/cm^2$ and incident angle with respect to the surface normal of $\theta_i \approx 45°$. Argon was dynamically evacuated by a turbomolecular pump. After sputtering, the Auger spectra revealed only the presence of metallic magnesium (Figure 2.1). In addition, the sputtering process resulted in the removal of the polishing damage layer thus revealing the grain contrast of the specimens (Figure 2.2). It should be noted that no annealing stage was performed. However, it was found that by keeping the total ion dose low ($< \approx 1 \times 10^{17}$ ions/cm^2) the creation of heavily disordered crystal planes could be avoided. The effect of ion bombardment on the initial uptake of oxygen on pure magnesium surfaces has been examined in detail and the results are presented in Chapter 4.

2.4 Grain Orientation Determination

Absolute surface crystallographic orientations of numerous grain faces were determined using the electron back-scattering diffraction technique (EBSD) [2.1-2.4], in order to allow AES measurements to be made on grains of known orientation. In this technique, a stationary electron probe is focussed on the grain face of interest, creating a divergent source of inelastically scattered electrons. Diverging beams which strike crystallographic planes at the corresponding Bragg angles become diffracted, producing cones of intense radiation. An imaging device close to the specimen then records the resulting array of lines (Kikuchi diffraction patterns), which can be analysed with appropriate software to yield the crystallographic orientation of the grains in question.

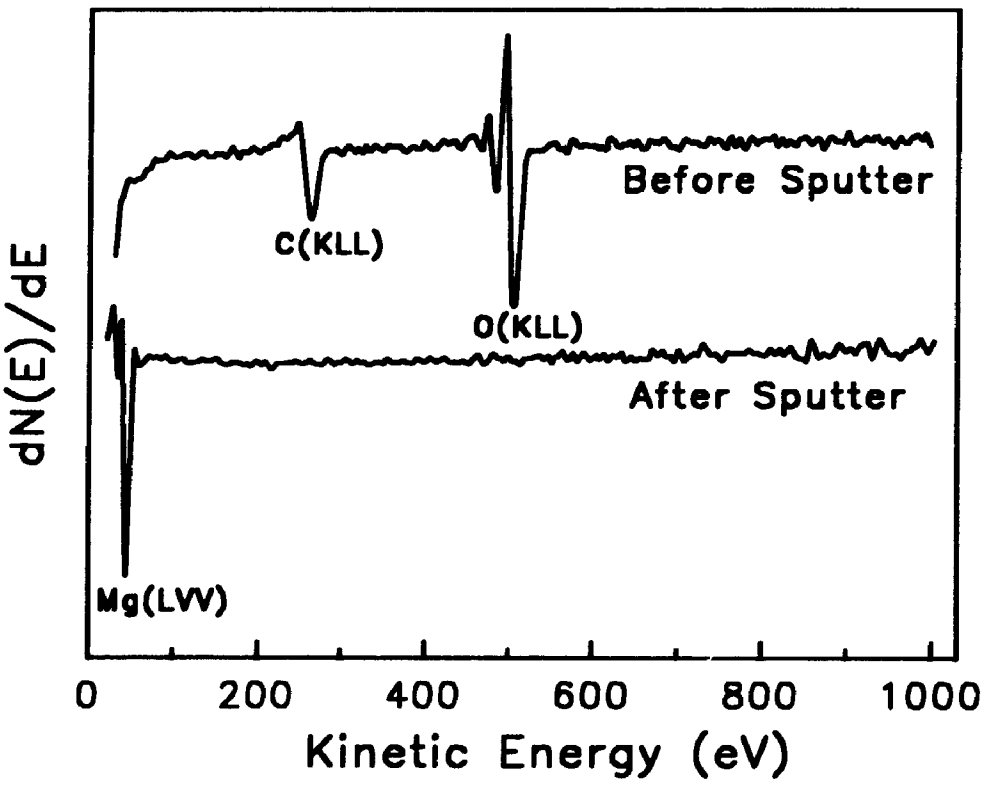

Figure 2.1: Representative Auger survey spectra of magnesium surfaces before and after cleaning by sputtering with 3 keV Ar^+ ions (dose $\approx 1 \times 10^{16}$ ions/cm^2).

Figure 2.2: Scanning electron micrograph of magnesium surface after Ar^+ sputtering.

The EBSD experiments were performed using a JEOL 840 scanning electron microscope equipped with a commercially available EBSD package at Ontario Hydro Research Laboratories, Toronto, Ontario. The specimens were mounted at a high tilt (70 to 80°) in order to shorten the path length of the backscattered electrons, thus decreasing the fraction of the signal that is absorbed by the specimen. The resulting Kikuchi patterns were viewed in real time using a low-light TV camera interfaced to a phosphor screen and analysed using dedicated software devised by Dingley [2.2,2.3]. Two issues were involved in determining the grain orientations: the orientation of the diffraction pattern with respect to the recording plane and the orientation of the recording plane with respect to the specimen. These issues were dealt with via a calibration routine whereby a standard Si(001) single crystal was mounted on a holder inclined at precisely the same angle used to mount the specimen. This arrangement ensured identical geometry with respect to the camera and allowed for absolute grain orientations to be made once the major poles in the Kikuchi patterns were recognised.

It was found that grains which exhibited dark secondary electron contrast (Figure 2.2) were preferentially sputtered to a relatively large depth and all showed nearly identical electron backscattering diffraction patterns (EBSDP's). Analysis revealed these grains to have surface normals very near the basal Mg(0001) pole. The angle between the specimen normal and the [0001] direction, φ, for these grains never exceeded five degrees. Grains exhibiting bright secondary electron contrast, on the other hand, were raised with respect to the basal grains and resulted in EBSDP's further removed from the Mg(0001) pole ($15° \leq \varphi \leq 30°$), representing relatively more open-packed, higher index

faces. Grain faces were then chosen for detailed study of oxygen uptake on the basis of widely differing contrast in their secondary electron images.

2.5 Gas Exposure Procedure

Clean surfaces were exposed in vacuum to calibrated doses of deuterated water vapour at 298 K for exposures ranging from 0.1 to 1 $\times$ 10^6 langmuir (L) (1 L = 1.33 $\times$ 10^{-4} Pa·s). The D_2O was obtained from MSD Isotopes, Ltd. and contained > 99 at% deuterium. The partial pressure of D_2O was measured using a Dycor Electronics quadrupole mass spectrometer. D_2O was used in place of H_2O for two reasons: (1) the mass spectrometer used for partial pressure measurements was more sensitive to D_2O than to H_2O and (2) it was possible to measure hydrogen (deuterium) present in the oxide film originating from the reactant gas using nuclear reaction analysis (NRA) (see section 2.6.3). The D_2O vapour was maintained in a stainless steel bottle and was degassed by performing several freeze-pump-thaw cycles. The major gaseous impurity detected by the mass spectrometer was hydrogen (H_2). Its presence is not, however, expected to affect the adsorption behaviour of water on magnesium to any appreciable degree, since previous studies reported that hydrogen did not interact with the clean magnesium surface [2.5]. The partial pressure of hydrogen in the vacuum chamber was estimated to be less than 10% of the water signal; the partial pressure of oxygen was estimated to be less than 5% of the water signal.

Exposures were completed by backfilling the vacuum chamber with D_2O via a leak valve. Exposures ranging from 0.1 to 100 L were performed *in situ* in the Auger analytical chamber. The actual exposure values for this range were determined by measuring the partial pressure of D_2O ($+H_2O$) with the quadrupole mass spectrometer and subsequently calibrating the leak valve for a given number of turns. Figure 2.3 shows a typical calibration curve obtained in this fashion. The exposure value in langmuir was then obtained by integrating the area under the curve in Figure 2.3 for a given time interval and applying appropriate conversion factors. This calibration procedure was repeated frequently to ensure reproducibility of the measured exposure values. For exposures exceeding 100 L, X-ray photoelectron spectroscopy (XPS) was used (see section 2.6.2). In these cases, exposure to D_2O was performed in a separate custom designed/constructed preparation chamber attached to the XPS spectrometer. Exposure values were determined by backfilling the vacuum chamber to a desired partial pressure of D_2O, measured by an ion pressure gauge, for a desired period of time. The accurate calibration procedures described above for the shorter exposures were not as critical for these experiments since the uncertainties incurred by the pressure transients following the valve openings and closings represented a correspondingly smaller percentage of the total exposure values. For all exposures involving backfilling of the vacuum chambers, it was necessary to wait for a sufficient time period between experiments ($\approx$ 30 min.) in order to prevent the chambers from retaining a *memory* of the reactant gas. Finally, for experiments performed using nuclear reaction analysis (NRA) (see section 2.6.3), D_2O exposures were performed using a capillary array doser

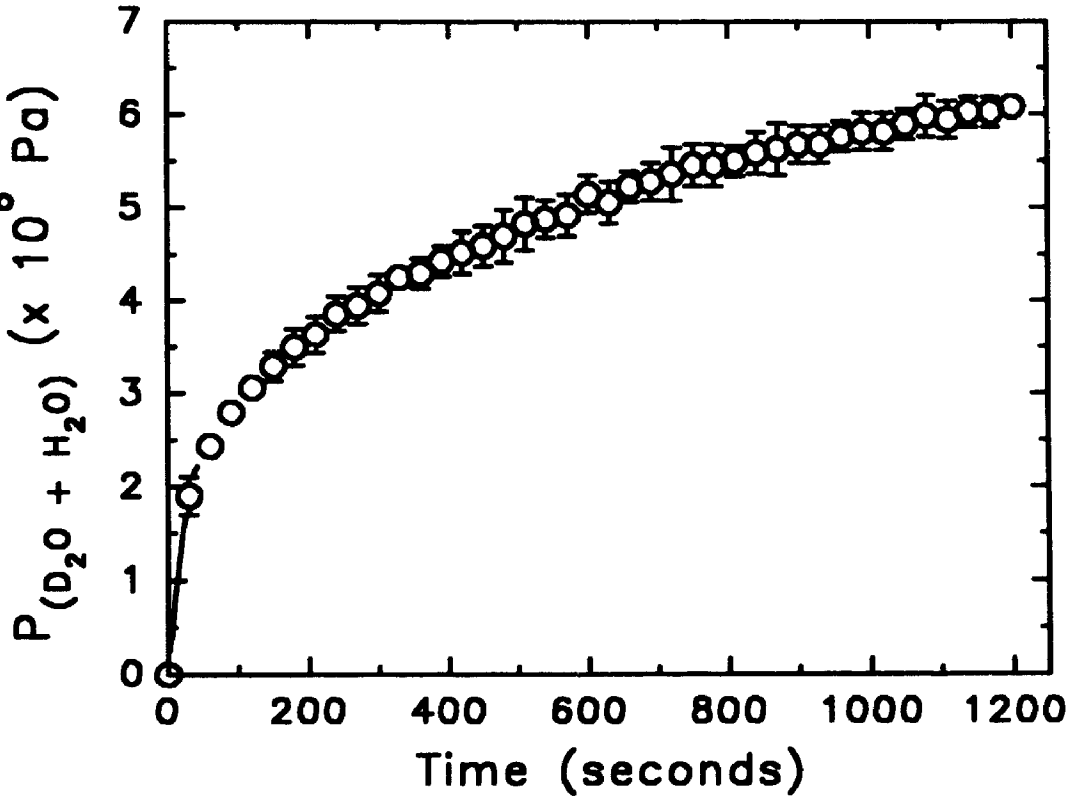

Figure 2.3: Typical calibration curve for the determination of water vapour exposure values. The calibration is for two full turns of the leak valve. The vertical error bars represent the standard deviation from three separate experiments.

[2.6] to minimise hydrogen exchange with the chamber walls. It was not possible to measure the exposure value directly using this method; therefore, concurrent Auger measurements were performed *in situ* in order to correlate the exposure values with those obtained earlier.

2.6 Analytical Methods

2.6.1 Auger Electron Spectroscopy (AES)

When an atom is bombarded by incident photons, electrons or ions, a vacancy may be created in one of the inner shells. The resulting excited atom subsequently relaxes by filling the core hole with an electron from an upper level. Removal of excess energy then occurs either by emission of a photon (the basis of X-ray fluorescence spectroscopy) or by emission of another shallowly bound electron. This latter process, known as the Auger process [2.7], is illustrated schematically in Figure 2.4 for an arbitrary KL_1L_{23} Auger transition [2.8]. The convention used to describe Auger transitions is based on the nomenclature employed by X-ray spectroscopists. In this system, the major quantum levels are designated K, L, M, N and O, and spin-orbit splitting of sub-shells is designated L_1, L_{23}, etc. For the Auger process illustrated in Figure 2.4, the initial state had a hole in the K shell, de-excitation occurred from the L_1 level and the Auger electron was emitted from the L_{23} level. Auger emission from the overlapping valence band levels are usually designated KLV, LVV, etc.

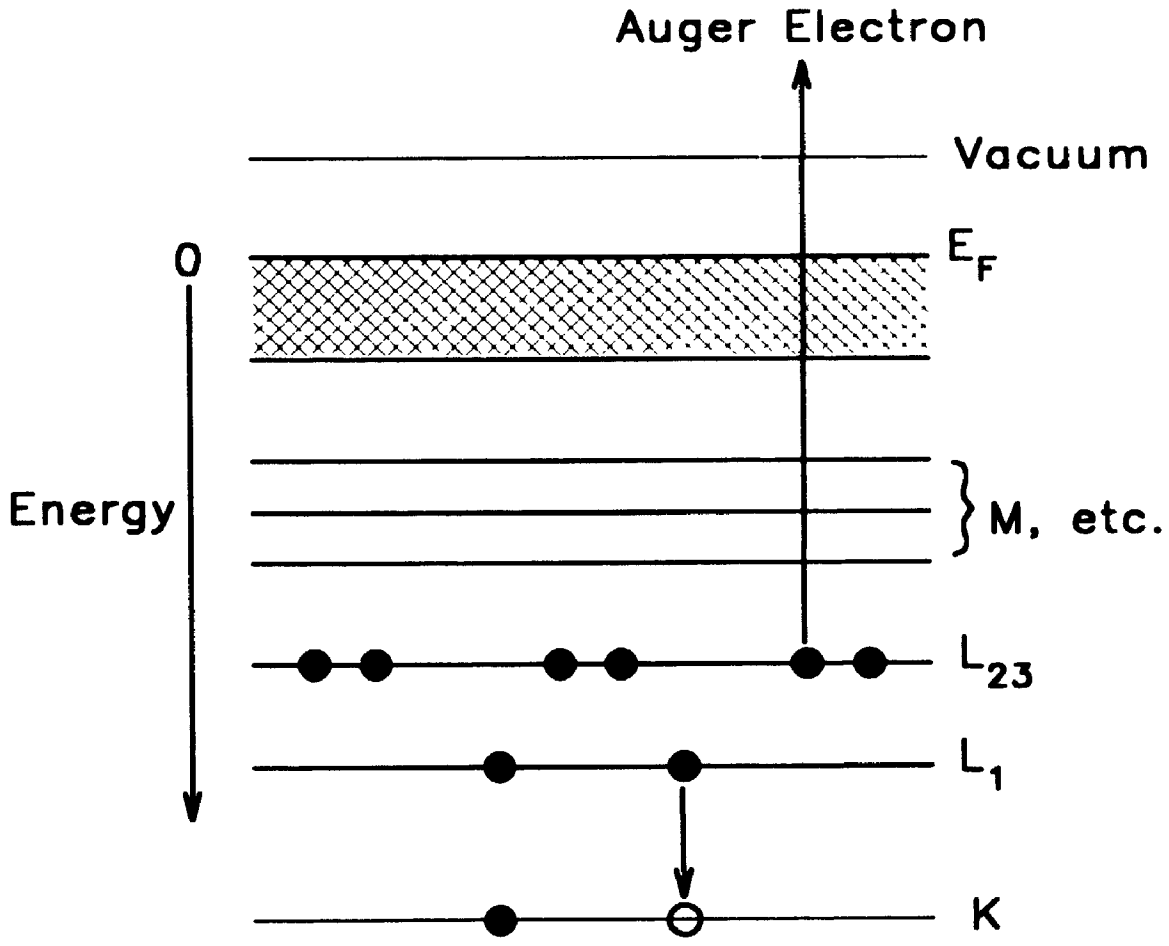

Figure 2.4: Schematic representation of an arbitrary KL_1L_{23} Auger process. (E_F ≡ Fermi level). (Adapted from ref. [2.8]).

The kinetic energy of the ejected Auger electron, E_A, depends upon the transitions which occur and can be estimated from the binding energies of the atomic energy levels involved. In simplified terms, the energy of the Auger electron in Figure 2.4 is given by:

$$E_A = E_K - E_{L_1} - (E_{L_{23}} + \delta) \qquad (2.3)$$

where E_i are the binding energies of the ith atomic energy levels. The term δ represents the relaxation energy arising from the additional screening of the atomic core when there is a hole in a core level [2.9]. Equation (2.3) shows that the Auger energy is a function of the atomic energy levels only, so that there is an unique set of Auger energies for each atom in the Periodic Table. All elements above helium produce characteristic Auger spectra in the 0 to 2000 eV energy range. The assignment of Auger lines is generally performed empirically using standard spectra derived from pure elements or simple compounds [2.10].

In some cases, the exact energy of a given Auger transition can be affected by the chemical environment of the atom in question. These effects can originate from the same source as the well-known "chemical shift" in XPS (see section 2.6.2), i.e. the binding energy of the core electrons with the nucleus is affected by the local density of valence states, leading to shifts in the measured Auger energies. Such shifts are not as easy to interpret as those observed in XPS, however, because of the two-electron nature of the

Auger process. The analysis of Auger peak shifts has nevertheless been used successfully in numerous oxidation and corrosion studies [2.11].

AES is a surface sensitive technique, meaning that it is capable of detecting changes that occur in the surface region of a specimen. The reason for this lies in the fact that the emitted Auger electrons are of relatively low kinetic energy ($\leq$ 2000 eV). Intense inelastic scattering occurs for electrons in this energy range, i.e. their inelastic mean free path (IMFP) is very short (0.5 to 2.0 nm). The IMFP is defined as the average distance which an electron can travel through a solid before 1/e (36.8%) of the electrons suffer significant energy loss due to inelastic collisions. The effective escape depth of an ejected Auger electron from the surface, λ, is subsequently determined by the IMFP, λ_o, and the angle of emission, θ, of the detected electrons with respect to the surface normal:

$$\lambda = \lambda_o \cos\theta \tag{2.4}$$

The probability that an electron emitted from a distance d from the surface will escape without energy loss is thus given by: [2.12]

$$p \propto \exp(-\frac{d}{\lambda}) \tag{2.5}$$

Consequently, only those electrons which originate from the outermost atomic layers of a solid survive to be ejected and contribute to the spectrum.

One fundamental drawback of AES is that the inelastically backscattered electrons create a very intense background count. The intensities of the characteristic Auger peaks are weak relative to the background, leading to a poor signal-to-noise ratio. It was shown by Harris in the 1960's, however, that the signal-to-noise ratio could be enhanced by taking the first derivative of the direct signal, thus recording the dN(E)/d(E) rather than N(E) spectra [2.13]. Differentiated plots can be obtained either electronically during data collection via a lock-in amplifier or by computer differentiation of stored direct spectra. In this work, the Auger spectra have been computer differentiated. Assuming that the Auger peak shapes of the direct spectra do not vary markedly between standard and unknown, the distance between the positive and negative excursions of the differentiated peaks (i.e. the peak-to-peak heights) can be used as a measure of the intensity of various Auger signals.

A typical AES system consists of a UHV system, an electron gun for specimen excitation and an energy analyzer for detection of Auger electrons. The Auger spectrometer used in this study was a Perkin-Elmer model PHI-600 scanning Auger microprobe (SAM). This is a dedicated AES instrument with an attached secondary electron detector for SEM imaging. The system incorporates an electromagnetically focussed electron gun utilising a lanthanum hexaboride (LaB_6) filament mounted down the centre of a single-pass cylindrical mirror analyzer (CMA) (Figure 2.5). This coaxial geometry has the advantage of reducing shadowing problems on rough surfaces. The

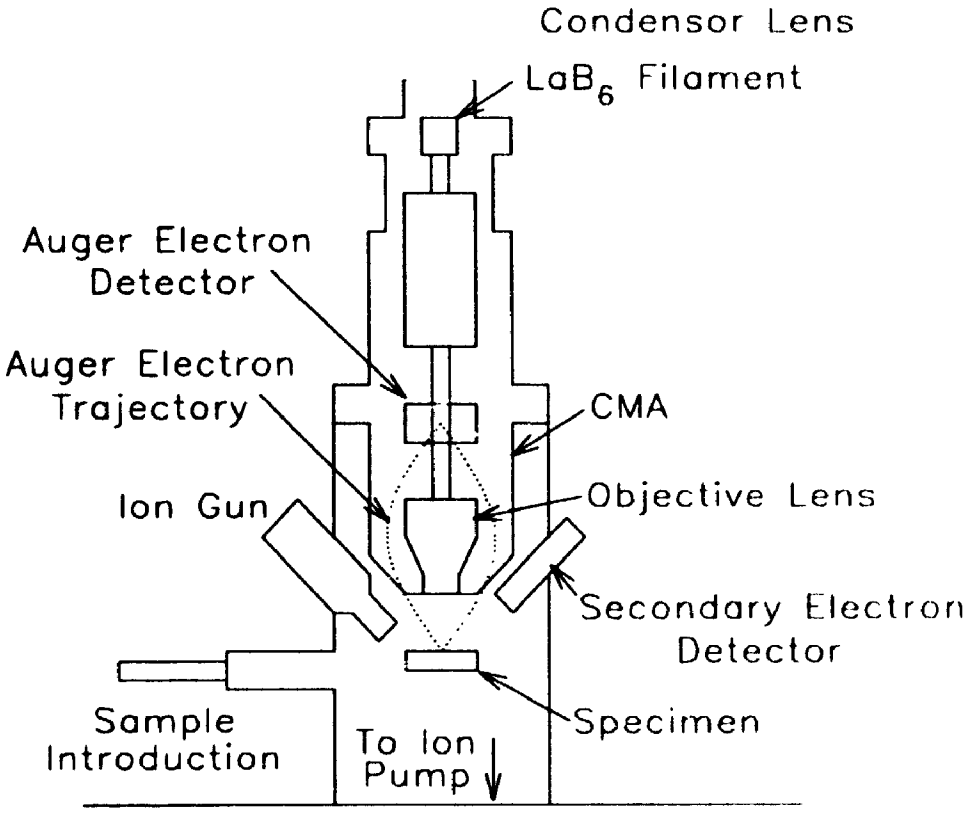

Figure 2.5: **Schematic representation of the experimental system used for scanning Auger microscopy (SAM).**

CMA has a large electron acceptance solid angle and an optimum relative energy resolution of $\Delta E/E = 0.6\%$. For a relative resolution of 0.6%, the instrumental contribution to the experimental peak width is 0.3 eV at an electron energy of 50 eV and 6 eV at an electron energy of 1000 eV. A further description of the operation of a CMA can be found elsewhere [2.8, 2.14]. Further details regarding the instrumental conditions (beam energy, beam current, etc.) used in this study are provided in Chapters 3 to 6, as required.

2.6.2 X-ray Photoelectron Spectroscopy (XPS)

X-ray photoelectron spectroscopy (XPS) is a surface sensitive technique capable of providing chemical composition and chemical state information of surface constituents, similar to AES. The main advantage in XPS lies in the well-defined variations in elemental binding energies (the chemical shifts) used to identify the chemical state of the materials being analysed (see below). The XPS experiment itself involves measuring the kinetic energy of electrons photoejected by the interaction of a monoenergetic beam of soft x-rays with a molecule. Figure 2.6 shows a schematic of the process for the emission of an arbitrary 2p photoelectron [2.8].

The basis of the technique is the photoelectric effect, explained by Einstein in 1905 [2.15]. According to Einstein, all of the energy of the impinging photon is expended in the ejection of a bound electron. As a consequence, an exact energy definition of the final state of the system can be obtained if the energy of the ejected

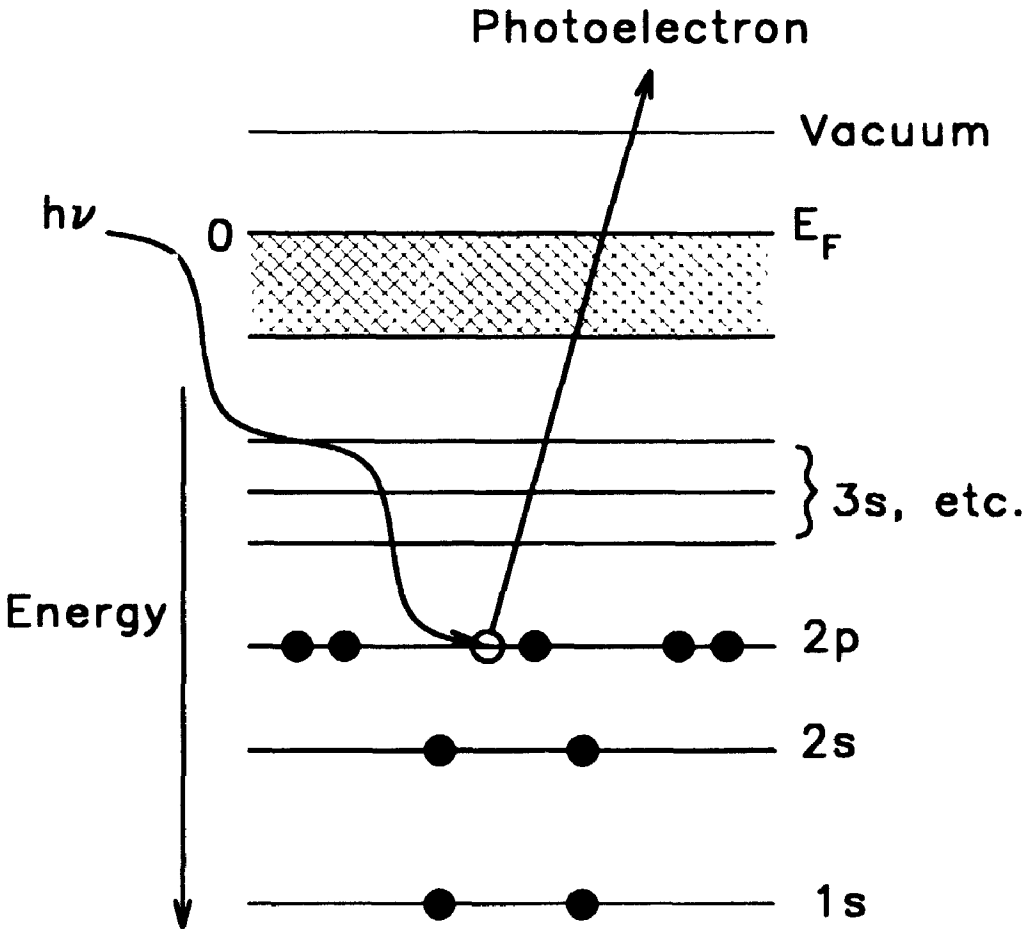

Figure 2.6: Schematic representation of the process leading to the emission of an arbitrary 2p photoelectron. ($E_F \equiv$ Fermi level). (Adapted from ref. [2.8]).

photoelectron is known for a given quantum of excitation put into the system. The basic equation is therefore given by:

$$BE = h\nu - KE - \phi \tag{2.6}$$

where BE is the binding energy of the photoelectron for the particular element and its chemical environment; $h\nu$ is the photon energy; KE is the kinetic energy of the ejected photoelectron; and ϕ is the work function of the specimen. When dealing with conductive samples in good electrical contact with the spectrometer, however, the Fermi levels of the sample and spectrometer are the same (Figure 2.7). Therefore, an electron being ejected from the sample will have to overcome the work function of the sample, ϕ, but when it enters the analyzer chamber, it will adjust to the work function of the spectrometer, ϕ_s. The kinetic energy of the ejected photoelectron measured by the analyzer, KE^*, will thus be different than the actual kinetic energy of the photoelectron leaving the sample, KE, because of the contact potential difference (ϕ_s-ϕ). From Figure 2.7, it is evident that the binding energy, referenced to the Fermi level, can be obtained from the *measured* photoelectron kinetic energy according to:

$$BE = h\nu - KE^* - \phi_s \tag{2.7}$$

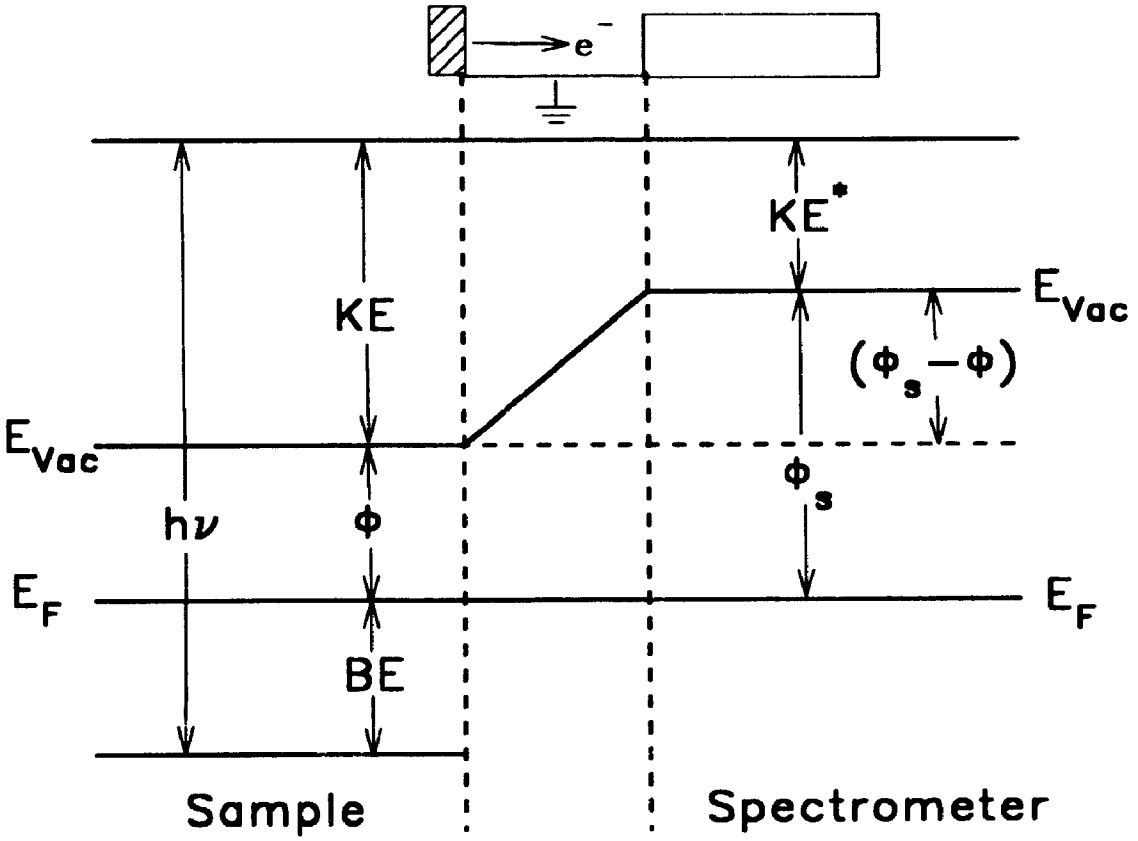

Figure 2.7: Schematic energy level diagram for sample and spectrometer in electrical contact. ($h\nu \equiv$ photon energy; BE $\equiv$ binding energy; KE $\equiv$ kinetic energy; $\phi \equiv$ work function; $E_{vac} \equiv$ vacuum level; $E_F \equiv$ Fermi level). (Adapted from ref. [2.16]).

The value for ϕ_s is constant for a given spectrometer and will remain the same regardless of the sample being analysed. For this reason, binding energies are always referenced to the Fermi level when dealing with solids.

Because there is a unique set of binding energies for each element in the Periodic Table, XPS can be used to identify the elements present on the surface. As with AES, elemental identification is achieved via the use of standard spectra combined with insight concerning the material under investigation [2.17]. Small changes in the measured binding energies can also be used to identify the chemical state of the elements present on a surface. These changes, or "chemical shifts", are the result of varying valence electron densities for different chemical environments. Valence electrons tend to shield the core electrons and reduce their interaction (i.e. Coulombic potential) with the atom nucleus. If the valence electron density is decreased, therefore, the interaction of the core electrons with the nucleus is increased and the binding energy increases. This is the case when the oxidation state of an element is increased (e.g. $Mg^0 \rightarrow Mg^{2+}$). Conversely, when the oxidation state of an element is decreased (e.g. $O^- \rightarrow O^{2-}$), the binding energy of the core electrons measured by XPS is correspondingly decreased.

XPS can also be used to determine the relative concentrations of the various constituents in the surface of a specimen. Methods are available for providing semi-quantitative analyses using measured XPS intensities (peak areas) of the elements in question and their appropriate sensitivity factors [2.17]. Quantification of XPS data is complicated by several factors, including the need to use spectral fitting routines to

extract individual peak intensities from overlapping spectra and the need to account for differing IMFP's for photoelectrons of differing kinetic energy [2.18].

The XPS instrument used throughout this work was a Surface Science Laboratories SSX-100 spectrometer, featuring a monochromatic Al Kα (1486.6 eV) X-ray source [2.19]. The system was modified "in-house" to include a custom designed/built UHV preparation/reaction chamber. Figure 2.8 shows a schematic drawing of the major components. The instrument functions are controlled using a Hewlett-Packard Model 9836 microcomputer with SSL-supplied software for data acquisition and spectral analysis. Differentially pumped ion guns are situated in both the preparation and analytical chambers for specimen cleaning and depth profiling. UHV conditions are maintained in all chambers by turbomolecular and ion pumps in suitable configurations.

The SSX-100 spectrometer makes use of a concentric hemispherical analyser (CHA) for measuring the kinetic energies of photoelectrons emitted from a sample. This is an energy dispersive instrument wherein only those electrons having a kinetic energy within a certain window are allowed to traverse the analyser and be counted. All incoming electrons are retarded to a constant energy, the pass energy, before entering the focal plane of the analyser. By fixing the pass energy, a constant absolute energy resolution can be realised. This instrument affords a choice of pass energies ranging from 150 eV down to 25 eV, providing progressively increasing energy resolution. The choice of analysing parameters depends on the information sought for a particular sample. All of the high resolution ("narrow" scan) spectra presented in this thesis were

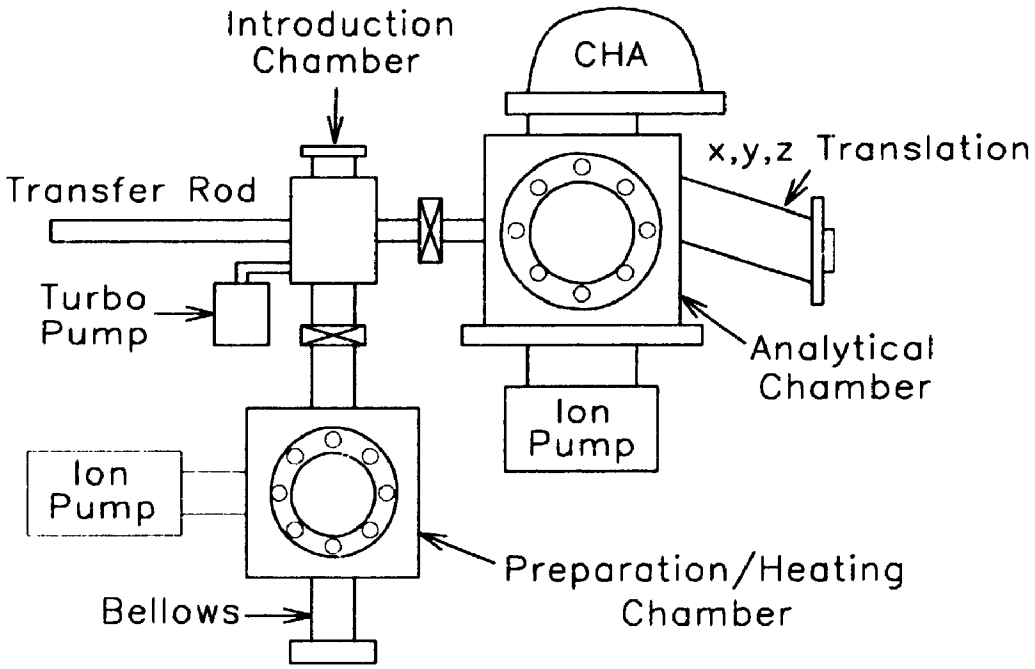

Figure 2.8: **Schematic representation of the custom designed/built UHV system incorporating the SSX-100 XPS spectrometer.**

obtained using a pass energy of 50 eV, giving a constant energy resolution (FWHM/count rate) of ≈ 0.70 eV/1.3×10^3 counts/min. Further details regarding instrumental conditions are again provided in Chapters 3 to 6, as required.

2.6.3 Nuclear Reaction Analysis (NRA)

Absolute surface coverages of deuterium were measured for the reaction of D_2O with pure magnesium surfaces using nuclear reaction analysis (NRA) (Chapter 3). This section provides a brief overview of the technique; a detailed description is considered to be beyond the scope of this thesis. For a more complete treatment of NRA, the reader is referred to the literature [2.6, 2.16].

In general, NRA makes use of specific nuclear reactions in order to measure absolute surface coverages of adsorbates on surfaces. The technique is highly surface sensitive, with detection limits approaching 1×10^{13} atoms/cm^2 (≈ 0.01 ML). The nuclear reactions themselves are of the form:

$$X + a \rightarrow Y + b + Q' \qquad (2.8)$$

where X and Y are heavy nuclei; a and b are light nuclei; and Q' is an energy balance term. In this scheme, an incident particle a interacts with a target nucleus X, via the nuclear force, creating a high energy transition state. This *compound nucleus* subsequently decays, yielding a product nucleus Y and an ejected particle b. It is

necessary that the incident particles possess sufficient energy to overcome the nuclear barrier ($\approx$ 1 MeV for light nuclei) and cause the required nuclear changes [2.16]. For this reason, a high energy particle accelerator is required. The absolute adsorbate coverage is then determined by measuring the yield of emitted *b* particles, Y_s, according to:

$$Y_s = N_s \sigma(E,\theta) \Omega Q_s \tag{2.9}$$

where N_s is the areal density of emitting atoms (atoms/cm^2); $\sigma(E,\theta)$ is the nuclear cross section for the event, itself dependent upon the energy of the incident particles (E) and the measuring geometry (θ); Ω is the detection solid angle; and Q_s is the flux of incident *a* particles. In practice, the measurement of surface adsorbate coverages is greatly facilitated by the use of a reference standard of known elemental content [2.16,2.20-2.23]. By placing the sample and standard in identical geometry, the need to measure the cross section and detection solid angle is obviated.

Equation (2.8) can be abbreviated to X(a,b)Y. In the present work, deuterium coverages were measured by counting the energetic protons, *p*, from the D(^{3}He,p)^{4}He nuclear reaction which has a resonance in the cross section at 630 keV incident $^3He^+$ ion energy. The experiments were performed in a separate UHV chamber (base pressure $\approx$ 4 $\times$ 10^{-8} Pa) which is interfaced to an HVEC 2.5 MV Positive Ion Van de Graaff machine in the Department of Physics at the University of Western Ontario. The ion flux was determined by integrating the ion beam current measured by an external transmission Faraday cup which intercepted the beam at periodic intervals. The protons

were counted by a silicon charged particle detector [2.6,2.24]. The proton yields were compared to a stoichiometric Ta_2O_5 standard, 26.7 nm in thickness and containing 1.463 $\times$ 10^{17} ^{16}O atoms/cm^2, using the $^{16}O(D,p)^{17}O$ reaction. It was possible to use this standard to measure absolute deuterium coverages because the ratio of the cross sections $\sigma[D(^3He,p)^4He)]$:$\sigma[^{16}O(D,p)^{17}O]$ was measured previously for various incident energies [2.25,2.26].

2.6.4 Secondary Ion Mass Spectrometry (SIMS)

SIMS is a surface analytical technique capable of detecting all elements in the Periodic Table with unparalleled sensitivity, in the low parts per million and in some cases parts per billion range. For this reason, SIMS was used in the present work to detect and image the presence of very low (ppm) levels of iron deliberately introduced into magnesium specimens (Chapter 6). This section provides a brief description of the technique; a more thorough discussion can, once again, be found in the literature [2.27,2.28].

The SIMS experiment involves the production, extraction and detection of ionized sample atoms and molecules. These so-called *secondary* ions are usually generated by sputtering with a *primary* ion beam of between a few and tens of keV kinetic energy. During the sputtering process, most of the ejected atomic and molecular species are neutral. A small portion is, however, ionised. These ions are easily extracted from the specimen surface by means of an electromagnetic field, mass separated according to their

mass to charge ratio (*m/q*) and detected by one of several charged particle counting systems. Because of the inherent sputtering action of the primary ion beam, the intensity of secondary ions can be collected from successively deeper layers, thus creating a concentration versus depth profile. In some instruments, the spatial integrity of the secondary ions from the sample surface can be maintained, enabling the formation of two-dimensional images of ion intensities from the specimen. If these images are then collected and stored in a computer as a function of sputtering time, three-dimensional image depth profiles showing both the lateral and depth location of elements in the surface can be formed.

There are two general modes of SIMS operation: dynamic SIMS (DSIMS) and static SIMS (SSIMS). In the former, higher primary ion beam current densities (of the order of several mA/cm^2) are used to achieve high sensitivity depth profiles for several μm's into the surface. In SSIMS, on the other hand, the primary beam current densities are lowered to such an extent that the rate of erosion is only a fraction of a monolayer per minute, thus providing greatly enhanced surface sensitivity. Both modes of operation were employed in this work. DSIMS was used to image the distribution of iron atoms in magnesium samples doped with up to 700 ppma Fe and SSIMS was used to search for the presence of these iron atoms in the thin oxide films formed on the surfaces (Chapter 6). The dynamic SIMS images were generated using a Cameca IMS-3f ion microscope which has been modified to record secondary ion images digitally during a depth profile. This instrument makes use of a magnetic sector mass analyser and possesses high sensitivity and unmatched mass resolution [2.28]. The imaging system and the associated

software was developed "in house" and has been discussed in detail elsewhere [2.29, 2.30]. The SSIMS experiments were performed using a modified Vacuum Generators (VG) ZAB-2F high performance mass spectrometer at the Scientific Research Laboratories of the Ford Motor Company, Dearborn, Michigan. This instrument is routinely operated at primary ion beam current densities as low as 150 to 500 pA/cm^2, thus significantly increasing the lifetime of monolayer coverages on the surface. The instrumental modifications and capabilities are discussed in detail elsewhere [2.31].

References

[2.1] J.A. Venables and C.J. Harland, Phil. Mag. 27 (1973) 1193.

[2.2] D.J. Dingley, Scanning Electron Microsc. IV (1984) 273.

[2.3] D.J. Dingley, Scanning Electron Microsc. II (1981) 569.

[2.4] V. Randle, Microtexture determination and its applications (The Institute of Materials, London, 1992).

[2.5] S.A. Flodström, L.G. Petersson and S.B.H. Hagström, J. Vac. Sci. Technol. 13 (1976) 280.

[2.6] S.J. Bushby, Ph.D. Thesis (The University of Western Ontario, London, 1992).

[2.7] P. Auger, J. Phys. Radium 6 (1925) 205.

[2.8] D. Briggs and J.C. Rivière, in D. Briggs and M.P. Seah (Eds.) , Practical Surface Analysis, Volume 1, Second Edition (J. Wiley and Sons, Chichester, 1990) p.85.

[2.9] D.A. Shirley, Chem. Phys. Lett. 17 (1972) 312.

[2.10] L.E. Davis, N.C. MacDonald, P.W. Palmberg, G.E. Riach, R.E. Weber and G.E. Muilenberg, PHI Handbook of Auger Electron Spectroscopy (Physical Electronics Industries, Ltd., Eden Prairie, MN, 1976).

[2.11] N.S. McIntyre and T.C. Chan, in D. Briggs and M.P. Seah (Eds.), Practical Surface Analysis, Volume 1, Second Edition (J. Wiley and Sons, Chichester, 1990) p.485.

[2.12] S. Hofmann, in D. Briggs and M.P. Seah (Eds.), Practical Surface Analysis, Volume 1, Second Edition (J. Wiley and Sons, Chichester, 1990) p.

[2.13] L.A. Harris, J. Appl. Phys. 39 (1968) 1419.

[2.14] T.A. Carlson, Photoelectron and Auger Spectroscopy (Plenum Press, New York, 1975).

[2.15] A. Einstein, Ann. Phys. 17 (1905) 132.

[2.16] L.C. Feldman and J.W. Mayer, Fundamentals of Surface and Thin Film Analysis (Elsevier Science Publishing Co., New York, 1986).

[2.17] J.F. Moulder, W.F. Stickle, P.E. Sobol and K.D. Bomben, Handbook of X-ray Photoelectron Spectroscopy (Perkin-Elmer Corporation, Minnesota, 1992).

[2.18] M.P. Seah, in D. Briggs and M.P. Seah (Eds.), Practical Surface Analysis, Volume 1, Second Edition (J. Wiley and Sons, Chichester, 1990) p.201.

[2.19] R.L. Chaney, Surf. Interface Anal. 10 (1987) 36.

[2.20] G. Amsel, J.P. Nadai, C. Ortega, S. Rigo and J. Sieka, Nucl. Instr. Meth. 149 (1978) 705.

[2.21] G. Amsel, J.P. Nadai, C. Ortega and J. Sieka, Nucl. Instr. Meth. 149 (1978) 713.

[2.22] J.A. Davies and P.R. Norton, Nucl. Instr. Meth. 168 (1980) 611.

[2.23] P.R. Norton, J.A. Davies and T.E. Jackman, Surf. Sci. 122 (1982) L593.

[2.24] B.J. Flinn, Ph.D. Thesis (The University of Western Ontario, London, 1992).

[2.25] D. Phillips and J.P.S. Pringle, Nucl. Instr. Meth. 135 (1976) 389.

[2.26] T.E. Jackman, K. Griffiths, W.N. Unertl, J.A. Davies, K.H. Gürtler, D.A. Harrington and P.R. Norton, Surf. Sci. 179 (1987) 297.

[2.27] D. Briggs and M.P. Seah, Practical Surface Analysis, Volume 2, 2nd Edition (J. Wiley and Sons, Chichester, 1992).

[2.28] A. Benninghoven, F.G. Rüdenauer and H.W. Werner, Secondary Ion Mass Spectrometry (J. Wiley and Sons, New York, 1987).

[2.29] S. Lu, M.Sc. Thesis (The University of Western Ontario, London, 1992).

[2.30] S. Ramamurthy, T.L. Walzak, S.F. Lu, T.C. Lipson and N.S. McIntyre, Surf. Interface Anal. 17 (1991) 834.

[2.31] D. Schuetzle, T.J. Prater, S. Kaberline, J.E. deVries, A. Bayly and P. Vohralik, Rev. Sci. Instrum. 60 (1989) 53.

CHAPTER 3

THE INITIAL INTERACTION OF WATER VAPOUR WITH PURE MAGNESIUM SURFACES

3.1 Introduction

The interaction of water vapour with metal surfaces is of fundamental importance to the understanding of such processes as corrosion-passivation chemistry, electrochemistry and heterogeneous catalysis [3.1]. In this chapter, the initial oxide formation occurring on polycrystalline pure magnesium surfaces exposed to low partial pressures of water vapour at room temperature has been examined in detail using Auger Electron Spectroscopy (AES), X-ray Photoelectron Spectroscopy (XPS) and Nuclear Reaction Analysis (NRA). The oxidation behaviour of magnesium and magnesium alloys is of particular interest in view of their increasing use in structural applications where light weight is important (e.g. aerospace industries, automotive industries).

The interaction of oxygen with pure magnesium surfaces has been investigated extensively in other laboratories; previous groups have studied magnesium single crystals [3.2-3.10], foils [3.11] and evaporated films [3.12-3.16]. It has generally been agreed that the initial oxidation of magnesium with oxygen proceeds in three stages: (1) oxygen chemisorption below the topmost magnesium layer; (2) formation of an oxide layer and (3) oxide thickening. The details of the first two stages have been the focus of most studies, using various surface analytical techniques including AES, XPS, UPS, LEED,

HREELS, ELS, ellipsometry and work function measurements. Little attention has been given to the bulk thickening process. In earlier investigations in the 1960's, however, oxidation studies of evaporated magnesium films were conducted at low pressures and room temperature. Cohen [3.17] found a logarithmic-type rate dependence for the bulk thickening stage using the Wagener flow method, leading to a limiting oxide thickness in O_2 of approximately 2.5 nm ($\approx$ 12 monolayers (ML) of MgO). Addiss [3.18] studied the same process using a quartz microbalance and concluded that the data could be equally well fitted by inverse logarithmic or logarithmic-type expressions. Under these experimental conditions, however, the very early stages of the oxidation process, up to a few monolayers of oxide, could not be characterised.

The interaction of water vapour with magnesium has received less attention. Fuggle et al. [3.12] studied the reaction of clean polycrystalline magnesium films with H_2O and O_2 by XPS. It was concluded that magnesium formed oxidised layers with water vapour as with oxygen. The rate of reaction was, however, much slower with water vapour, with a maximum in the reaction rate occurring as the layer of oxide became nearly complete. In addition, it was concluded that the oxide film resulting contained relatively large amounts of hydroxyl or hydroxide species, based on the appearance of the core-level oxygen O(1s) XPS line. The mechanism of early oxide formation and continued thickening was not examined. Peng and Barteau [3.10] studied H_2O interactions with Mg(0001) and also detected hydroxyls according to XPS and UPS measurements. No kinetic data were presented. Finally, Schultz et al. [3.19] investigated the chemisorption of H_2O, O_2 and CH_3OH on polycrystalline magnesium by

time-of-flight analysis of directly recoiled surface atoms produced by pulsed Ar^+ irradiation. It was concluded that reactions with water caused hydroxyl species to assume positions above the outermost magnesium layer. A surface stoichiometry consistent with $Mg(OH)_2$ was calculated.

In the present work, AES was carried out on individual microcrystalline grain faces of known orientation to elucidate the mechanism of early oxide formation. It was found that the initial interaction with water vapour resulted in a three stage oxidation behaviour similar to that observed for oxygen interactions with magnesium. Continued oxide growth was monitored by XPS and a logarithmic-type growth behaviour was confirmed for exposures up to 1×10^6 langmuir (L). The oxide film stoichiometry was found to be mainly MgO. Hydrogen (deuterium) was determined by NRA to be present in the film only in small relative amounts, likely as hydroxyl groups trapped at the metal/oxide interface.

3.2 Experimental

The specimens and cleaning procedures used in this study are described in section 2.3. Clean surfaces were exposed in vacuum to calibrated doses of deuterated water vapour at room temperature for exposures ranging from 0.1 to 1×10^6 L., as described in section 2.5. Auger spectra of the clean and water-dosed surfaces were then obtained using a 3 keV electron beam energy and electron currents $\leq$ 30 nA to minimise electron beam-induced oxidation [3.20]. Electron beam effects were further minimised by

disabling all filaments, except the ion pressure guage, during water dosing. The peak-to-peak value of the derivative spectrum was used as a measure of intensity before normalization by the elastic peak intensity. The uptake of oxygen on the clean surfaces was monitored *in situ* by following the changes in the intensity of the metallic $Mg(L_{23}VV)$, the oxidised $Mg(L_{23})O(L_{23})O(L_{23})$ and the $O(K_1L_{23}L_{23})$ Auger lines. Using the instrumental conditions listed above, the signal-to-noise ratio (S/N) was measured to be $S/N \geq 370:1$ for the Mg(LVV) signal and $S/N \geq 165:1$ for the O(KLL) signal.

For exposures greater than 100 L the continued growth of oxide was monitored by XPS (see section 2.6.2). Oxide thicknesses were determined by monitoring the changes occurring in the high kinetic energy Mg(2p) photoelectron line during exposure to D_2O. Changes in the oxide film chemistry were followed by monitoring the core-level O(1s) photoelectron line. The spectrometer was calibrated to give a $Cu(2p_{3/2})$-$Cu(3p_{3/2})$ energy separation of 857.1 eV and the binding energy scale was referenced to a $Au(4f_{7/2})$ line position of 83.93 ± 0.05 eV for metallic gold. The pass energy of the hemispherical analyser was maintained at 50 eV giving a constant energy resolution (FWHM/count rate (counts/min)) of ≈ 0.70 eV/1.3K. Quantitative ratios of oxidized magnesium to oxygen atoms in the thin oxide films were obtained by correction of the integrated spectral intensities with the photoelectron cross-sections [3.21] using software developed by Surface Science Laboratories Inc. These cross-sections were corrected to account for the different inelastic mean free paths (IMFP) for photoelectrons of differing kinetic energies. For lines of differing kinetic energy it was also necessary to ensure that their intensities were measured using a pass energy high enough ($>$ 100 eV) so that the x-ray

spot was accepted entirely into the spectrometer. Exposure to D_2O was performed in a separate, custom-constructed preparation chamber (base pressure $\approx$ 1 x 10^{-7} Pa) and transfer to the analytical chamber was performed under UHV conditions.

Absolute surface coverages of deuterium were determined by Nuclear Reaction Analysis (NRA), as described in section 2.6.3. Results of several preliminary experiments showed no evidence for beam-induced desorption.

3.3 Results and Discussion

Figure 3.1 shows the changes in the derivative Auger spectra of magnesium in the 15 to 60 eV range for increasing exposures to D_2O up to 100 L. The spectra were collected from a grain face that exhibited dark secondary electron contrast (i.e. near-basal plane orientation, section 2.4). The spectrum labelled "clean" is characteristic of the clean sputtered magnesium surface in agreement with the literature [3.8,3.15,3.22] and is characterised by the main metallic $Mg(L_{23}VV)$ transition at 45 eV kinetic energy and the overlapping surface and bulk plasmon loss satellites at 34 eV. Exposing the clean surface to increased doses of D_2O results in an attenuation of the metallic 45 eV signal and a growth of the 34 eV signal. The latter also represents the main oxide $Mg(L_{23})O(L_{23})O(L_{23})$ Auger transition. From Figure 3.1 it is also evident that exposure to D_2O leads to the development of a new peak at 27 eV. This signal has been attributed to an interfacial $Mg(L_{23})O(L_1)Mg(V)$ transition, or a cross-transition at the oxide-metal interface involving levels from the oxide as well as the metal [3.22]. The variation of

Figure 3.1: Representative Auger spectra of clean magnesium (near-basal plane orientation) and the same surface exposed to the indicated exposures of D_2O. (45 eV ≡ main metallic $Mg(L_{23}VV)$ transition; 34 eV ≡ main oxide $Mg(L_{23})O(L_{23})O(L_{23})$ transition; 27 eV ≡ interfacial $Mg(L_{23})O(L_1)Mg(V)$ transition).

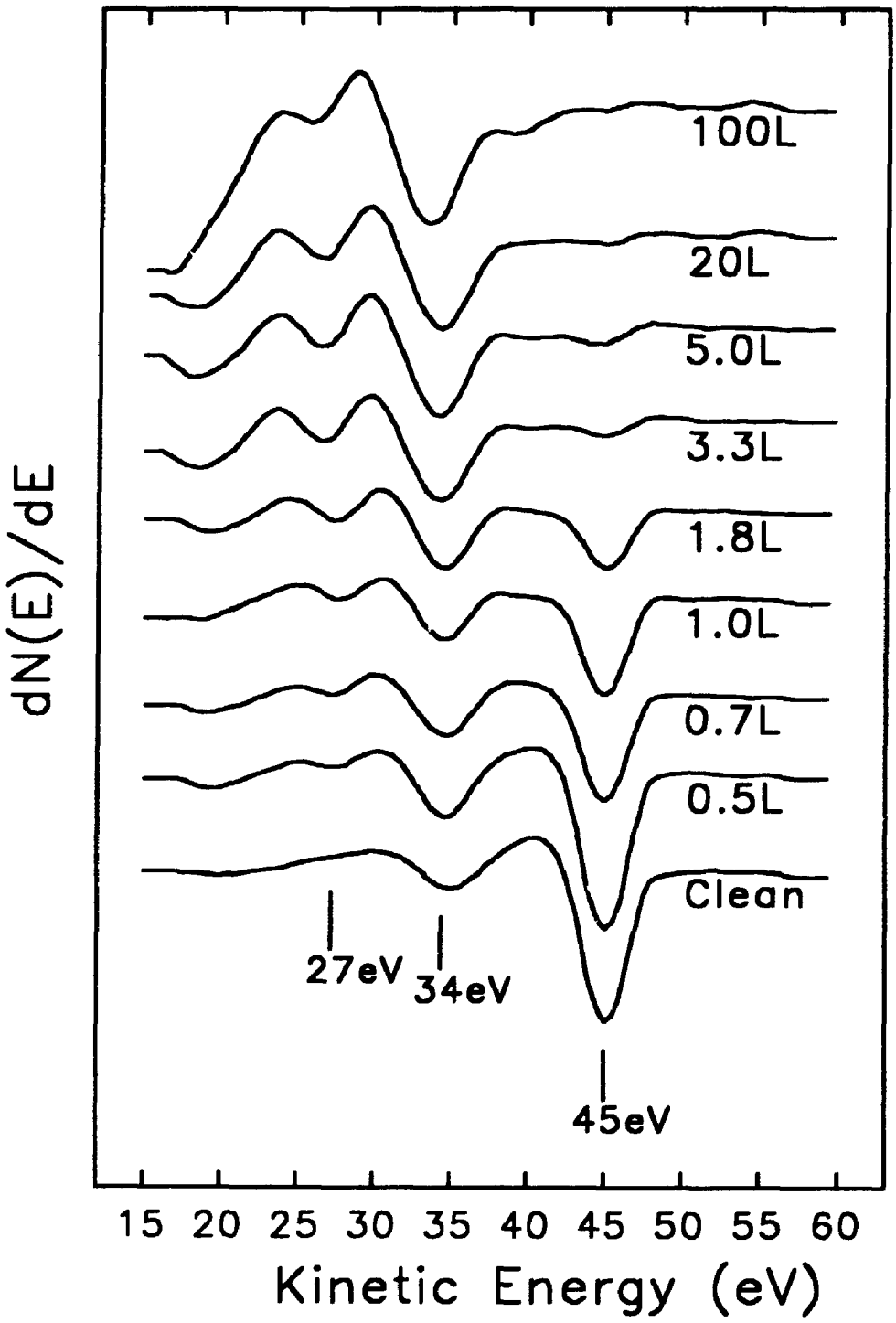
100L
20L
5.0L
3.3L
1.8L
1.0L
0.7L
0.5L
Clean
27eV
34eV
45eV
dN(E)/dE
15 20 25 30 35 40 45 50 55 60
Kinetic Energy (eV)

the peak-to-peak intensities of the three low-energy magnesium AES signals with D_2O exposure is shown in Figure 3.2.

The presence of the interfacial 27 eV AES peak at exposures as low as 0.5 L indicates that there is true chemical bonding between the oxygen present on the surface and the magnesium substrate. In addition, since the 27 eV line represents an interfacial transition, it is expected that it would appear with maximum intensity when the surface is covered with a thin oxide layer, but before bulk thickening begins. This is in fact observed in Figures 3.1 and 3.2, where the intensity of the 27 eV line reaches a maximum at an exposure of approximately 5 L; this observation suggests that bulk thickening of the oxide layer commences above this exposure value. These changes were accompanied by the simultaneous appearance and growth of an $O(K_1L_{23}L_{23})$ transition at 510 eV (not shown), which indicates that, at room temperature, water vapour dissociates on clean magnesium leading to the formation of MgO. Complete dissociation of the water molecule on magnesium surfaces at room temperature is also predicted by thermodynamic arguments [3.1].

In order to follow the initial oxygen uptake kinetics on magnesium in a more quantitative fashion, the attenuation of the metallic 45 eV Auger line intensity with increasing exposure to D_2O has been carefully monitored. Figure 3.3(a) shows the AES peak-to-peak intensity of the $Mg(L_{23}VV)$ transition, Mg, normalised to the clean magnesium signal, Mg^{clean}, for increasing exposures to D_2O. The data were collected from several grain faces exhibiting dark secondary electron contrast. The equivalent O(KLL) AES peak-to-peak intensities, normalised to the intensity near saturation (100

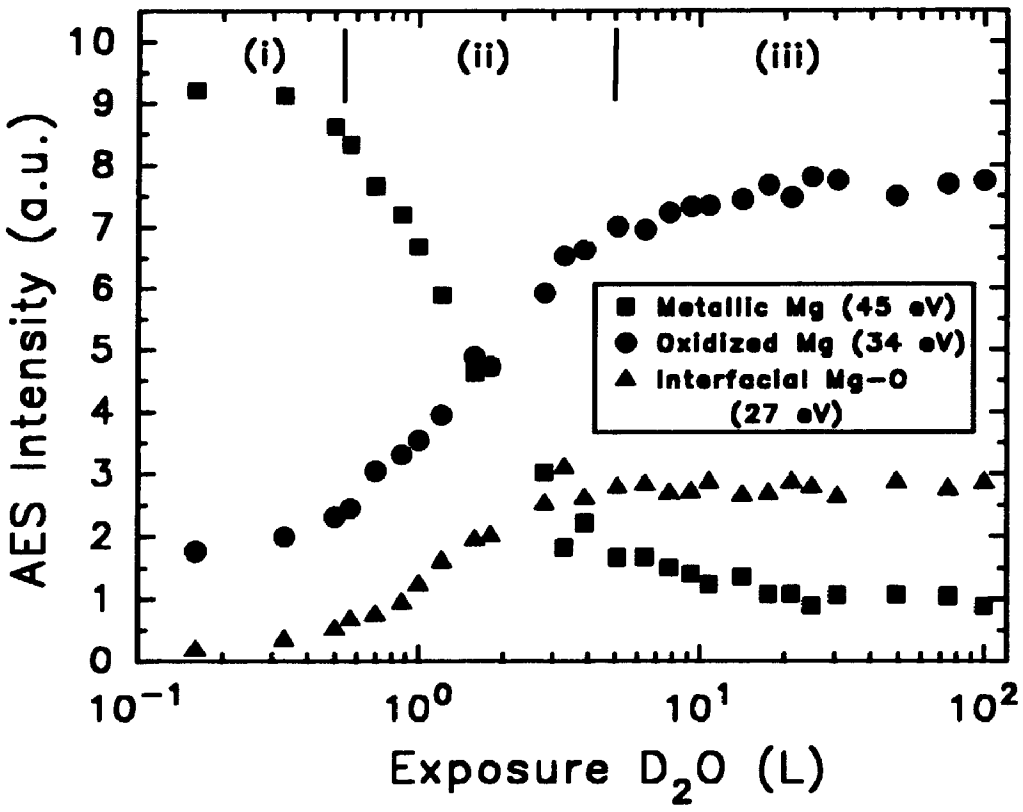

Figure 3.2: The evolution of the peak-to-peak intensities of the metallic Mg (45 eV), the oxidised Mg (34 eV) and the interfacial Mg (27 eV) AES signals as a function of D_2O exposure for near-basal grains of pure magnesium. The three-stage behaviour of oxygen uptake on magnesium is evident.

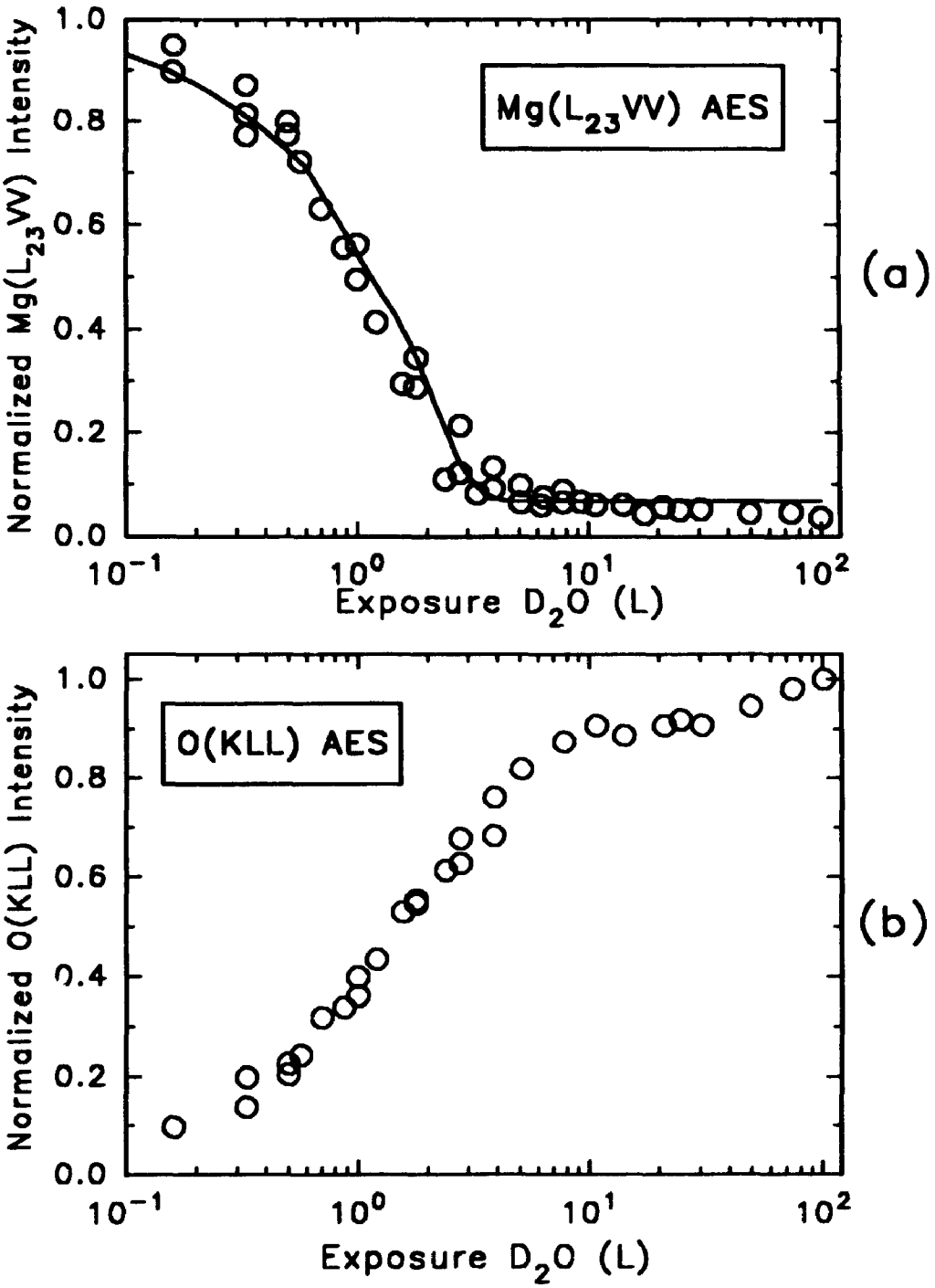

Figure 3.3: The growth of oxide on near-basal grains of magnesium. (a) The attenuation of the metallic Mg(LVV) AES signal where the solid line represents the best-fit line of equations (3.3) and (3.6) with the parameters of Table 3.1. (b) The increase in the normalised O(KLL) AES signal with exposure to D_2O.

L) are shown in Figure 3.3(b). From the figure, it is evident that there are three distinct regions of oxygen uptake on magnesium; both curves show a change towards a larger slope at about 0.75 L exposure and a change towards a smaller slope at about 5 L exposure. This three-stage behaviour has been observed for other metals [3.23-3.27] and has been interpreted as being due to the following general sequence in the oxidation process: (i) chemisorption; (ii) oxide nucleation and growth by islands until coalescence; and (iii) thickening of the oxide film by transport of the reactive species through the oxide. Although the limited accuracy of the experimental data do not allow it to be unambiguously established, it is proposed here that the three regions observed in Figure 3.3 correspond to these three stages of oxide growth.

The kinetics of th first two stages of the oxidation process can be described by the model proposed by Holloway and Hudson [3.24] and Mitchell et. al [3.25] for the oxidation of nickel. The first stage is represented by a non-activated dissociative Langmuirian chemisorption equation [3.24-3.27]:

$$\theta = 1 - \exp(-KL) \tag{3.1}$$

where θ is the oxygen coverage ($0 \leq \theta \leq 1$); L is the exposure value in langmuir (L); and K is a constant relating the gas impingement rate to the number of adsorption sites (L^{-1}). The observed metallic Mg(LVV) AES signal from a substrate partially covered by an oxygen overlayer one monolayer (ML) thick is then given by [3.28]:

$$\frac{Mg}{Mg^{clean}} = (1-\theta) + \theta \cdot \exp(-1/\lambda) \qquad (3.2)$$

where λ is the escape depth of the measured Auger electrons in (ML) (see below). Substituting equation (3.1) into equation (3.2) yields:

$$\frac{Mg}{Mg^{clean}} = \exp(-KL)+[1-\exp(-KL)][\exp(-1/\lambda)] \qquad (3.3)$$

The model used to describe the second stage is one of simultaneous oxide nucleation at a fixed number of sites, resulting in the formation of oxide islands which grow laterally until coalescence. Reaction at the nuclei perimeter is assumed to be the rate-controlling step, either by direct impingement from the gas phase or by diffusion of surface species to the perimeter [3.24,3.25]. The equation representing this type of process is:

$$\theta_{isl} = 1 - \exp[-C(L-L_o)^2], \quad for\ L>L_o \qquad (3.4)$$

where θ_{isl} is the coverage of islands ($0 \le \theta_{isl} \le 1$); C is a parameter related to the density of nuclei (L^{-2}); and L_o is the exposure value at which oxide nuclei first appear (L). Now, the AES intensity of metallic Mg(LVV) Auger electrons coming from a substrate covered with one monolayer of chemisorbed oxygen and partially (θ_{isl}) covered by islands of oxide is given by:

$$\frac{Mg}{Mg^{clean}} = \exp(-1/\lambda) + \theta_{isl} \cdot [\exp(-n/\lambda) - \exp(-1/\lambda)] \qquad (3.5)$$

where n is the average height of the oxide islands (ML). Combining equations (3.4) and (3.5) yields:

$$\frac{Mg}{Mg^{clean}} = \exp(-1/\lambda) + [\exp(-n/\lambda) - \exp(-1/\lambda)][1 - \exp(-C(L - L_o)^2)] \qquad (3.6)$$

Equations (3.3) and (3.6) thus describe the first two stages of the oxidation process, respectively.

It should be noted here that the above expressions make use of the well-known exponential attenuation of emitted electron intensity from solids (equation 2.5, Chapter 2), and consequently the *escape depth* of the Auger electrons (see section 2.6.1). In this thesis, the escape depths of the various Auger and photoelectrons of interest were calculated using the inelastic scattering model of Tanuma et. al [3.29] and are included in Appendix A. The calculated escape depths were then converted to equivalent monolayers of oxide using a value of 0.211 nm as the thickness of one monolayer of MgO. This value represents the average Mg-O bond distance in MgO [3.8].

Equations (3.3) and (3.6) were fitted to the experimental data of Figure 3.3(a) using non-linear regression. The solid line in Figure 3.3(a) represents the line of best fit obtained for the parameter values given in Table 3.1. The *best-fit* value for the escape

depth of the measured 45 eV electrons, λ, was determined to be 1.5 ML of MgO. This value closely matches that estimated using the empirical expressions of Tanuma et al. [3.29], viz. 1.6 ML for the instrument geometry (see Appendix A). Consequently, the parameter estimates provided in Table 3.1 are deemed to be reasonably accurate.

Table 3.1: Best-fit parameter estimates for calculation of curves in Figures 3.3(a) and 3.4 after equations (3.3) and (3.6).

	λ (ML)	L_o (L)	n (ML)	K (L^{-1})	C (L^{-2})
Near-basal	1.5	0.70	4.2	1.6	0.41
Higher-index	1.6	0.43	4.2	2.7	1.3

These parameter estimates then permit a semi-quantitative description of the first two stages of oxide growth on pure magnesium surfaces. It is apparent that the interaction of water vapour with pure magnesium at 298 K consists of rapid dissociation of the water molecule with concurrent chemisorption of the oxygen atoms, followed by oxide nucleation at approximately 0.7 L exposure. This initial stage is followed by oxide island growth, with coalescence of the islands occurring after the islands have reached an average thickness of about four monolayers. Beyond this stage ($\approx$5 L exposure, Figure 3.3(b)), a diffusion-controlled logarithmic growth of oxide appears to dominate.

The initial oxygen uptake on grain faces of high-purity magnesium exhibiting bright secondary electron contrast has been followed in an identical fashion. Figure 3.4 shows the normalised metallic Mg(L_{23}VV) Auger intensity for increasing exposure to D_2O. Again, the data were collected from several grain faces showing similar contrast levels. The data were also fitted to equations (3.3) and (3.6) using non-linear regression and the solid line in Figure 3.4 represents the line of best fit (the line of best fit for the previous dark grain data is included in the figure for comparison). The best-fit parameters are presented in Table 3.1.

From Figure 3.4 and the parameter estimates of Table 3.1 it is evident that the rate of initial oxygen uptake on clean magnesium surfaces exposed to water vapour is faster on the more open-packed grain faces (bright contrast), compared to those showing dark contrast, particularly in the second (oxide nucleation and growth) stage. Several observations lead to this conclusion. First, oxide nucleation was observed to occur more rapidly on bright grains than on dark grains (ie. at $\approx$0.4 L exposure compared to $\approx$0.7 L exposure). In addition, the parameter K in equation (3.1) is a constant relating the gas impingement rate to the number of adsorption sites on the surface and is given by:

$$K = \frac{1}{(2\pi mkT)^{1/2}\, N_o^{nucl}} \tag{3.8}$$

where m is the mass of the oxygen atom; kT is the thermal energy of the gas; and N_o^{nucl} is the number of occupied sites at the end of the chemisorption stage.

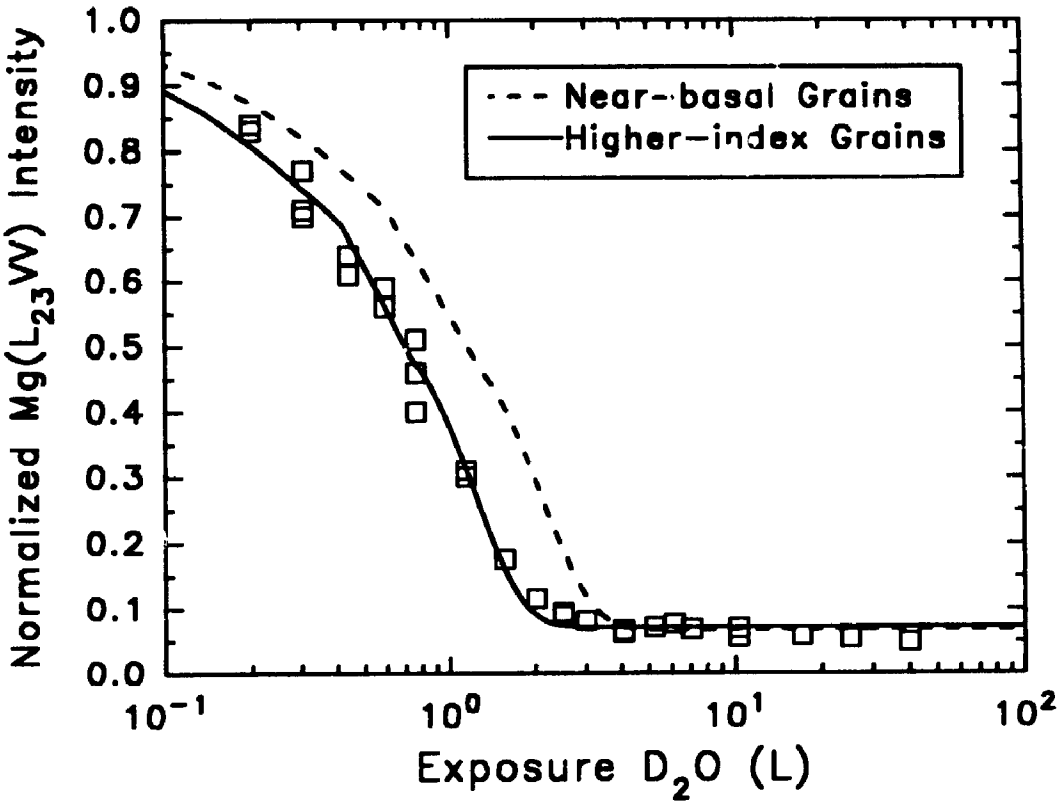

Figure 3.4: The attenuation of the metallic Mg(LVV) AES signal for higher-index grains of magnesium. The solid line represents the line of best fit for equations (3.3) and (3.6) with the parameters of Table 3.1. The rate of oxygen uptake is faster on higher-index grains compared to near-basal grains.

Thus, for the values of K given in Table 3.1, we obtain $N_o^{nucl} \approx 3.2 \times 10^{14}$ cm^{-2} for dark grains and $N_o^{nucl} \approx 1.9 \times 10^{14}$ cm^{-2} for bright grains. That is, on the more close-packed grain faces (dark contrast) it appears that the surface is covered with more occupied sites at the end of the chemisorption stage than on those showing bright contrast. Finally, the parameter C is directly proportional to the density of oxide nuclei on the surface after the chemisorption stage [3.24]; thus, the higher value for C for bright grains points to a higher oxide nuclei density on the surface after the chemisorption stage. In summary, then, the kinetic data and theoretical modelling results presented here suggest that initial nucleation of oxide is faster on grains of magnesium that show bright secondary electron contrast, i.e. on relatively more open-packed high index planes. There are fewer occupied adsorption sites at the end of the chemisorption stage on these faces compared with those of the dark, close-packed near-Mg(0001) grains and, consequently, a higher oxide nuclei density.

The initial dissociation of the water molecule and subsequent chemisorption of oxygen is expected to be isotropic with respect to the clean surface. Besides macroscopic surface roughness, there also exists roughness on an atomic scale, in the form of kinks, steps, etc. These defect sites are then expected to act as "preferential sites" for dissociation and chemisorption [3.1,3.30]; since they are randomly distributed, chemisorption is also assumed to be random. This assumption is supported by the results of Thiry et al. [3.6,3.7] who observed identical vibrational energies for oxygen chemisorption on both Mg(0001) and Mg($1\bar{1}00$) surfaces by HREELS and concluded that the adsorption sites were identical for each surface. The subsequent ordering of the

chemisorbed species into oxide nuclei then appears to be dependent upon the crystallographic orientation of the particular grain presented to the impinging water molecules. The nucleation of oxide is faster on the more open-packed faces, where the surface atom coordination number is smaller. It is possible that the initial interaction of water vapour with such surfaces destroys their symmetry, thus enhancing the oxidation process. Similar observations were made for oxygen interactions with Mg($1\bar{1}00$) [3.2,3.6,3.7]. The close-packed near-Mg(0001) faces, on the other hand, retain their symmetry and high coordination during the initial interaction with water vapour, despite the strength of the metal-oxygen bond in relation to the metal-metal bond. This likely then leads to a retardation of oxide nucleation.

It is worth noting that the observed differences in oxygen uptake behaviour on various grain faces were found to disappear when the surface had been sputtered with excessive doses of Ar^+ ions ($> 1 \times 10^{17}$ ions/cm^2). The rate of oxygen uptake was lowered for all grain faces after excessive sputtering. It is likely, therefore, that the high ion beam doses cause significant defects to dominate the surface reactivity. The effect of Ar^+ ion bombardment on the surface reactivity has been examined in detail and the results are presented in Chapter 4.

Beyond about five monolayers oxide thickness, the low-energy magnesium Auger signal is almost completely extinguished (Figure 3.3(a)). Therefore, in order to follow the oxidation processes on high-purity magnesium to much higher exposures, X-ray Photoelectron Spectroscopy (XPS) was employed. By monitoring the changes occurring in the core-level Mg(2p) photoelectron line, it was possible to detect changes in oxide

thicknesses to much higher exposure values. This is the case since the IMFP of the energetic photoelectrons is much longer than that of the low-energy Mg(L_{23}VV) Auger electrons (Appendix A).

Figure 3.5 shows the changes in the Mg(2p) core-level photoelectron spectra for increasing exposures to D_2O up to 1×10^6 L. The clean metal magnesium 2p peak is narrow (FWHM $\approx$ 0.85 eV) and has an asymmetric line shape, with a significant tail to higher binding energies. This is consistent with observations made by previous investigators [3.5,3.16]. Asymmetric broadening of core-level metal photoelectron peaks has been attributed to the production of a positive potential site which scatters the conduction electrons across the Fermi level, providing a continuous range of allowed one-electron excitation energies [3.31]. Upon exposure to water vapour, a shoulder develops shifted approximately 1.6 eV to higher binding energy. This new structure had a broader width of 1.5 to 2.0 eV and was gaussian in shape. This new peak is due to magnesium atoms which have reacted with oxygen and is identical in binding energy to that observed for heavily oxidised magnesium and for bulk MgO [3.32,3.33].

The thickness of the oxide layer formed on magnesium at various exposures was determined by measuring the intensity ratios of the metallic and oxidic Mg(2p) peaks and using the expression developed by Strohmeier [3.34]. Assuming a uniform overlayer, the oxide thickness, d (ML), is given by:

Figure 3.5: High-resolution Mg(2p) core-level XPS spectra of the clean magnesium surface and the same surface exposed to the indicated exposures of D_2O. Increasing exposures leads to a growth of the oxidic component (binding energy $\approx$ 51.35 eV) at the expense of the metallic component (binding energy $\approx$ 49.74 eV).

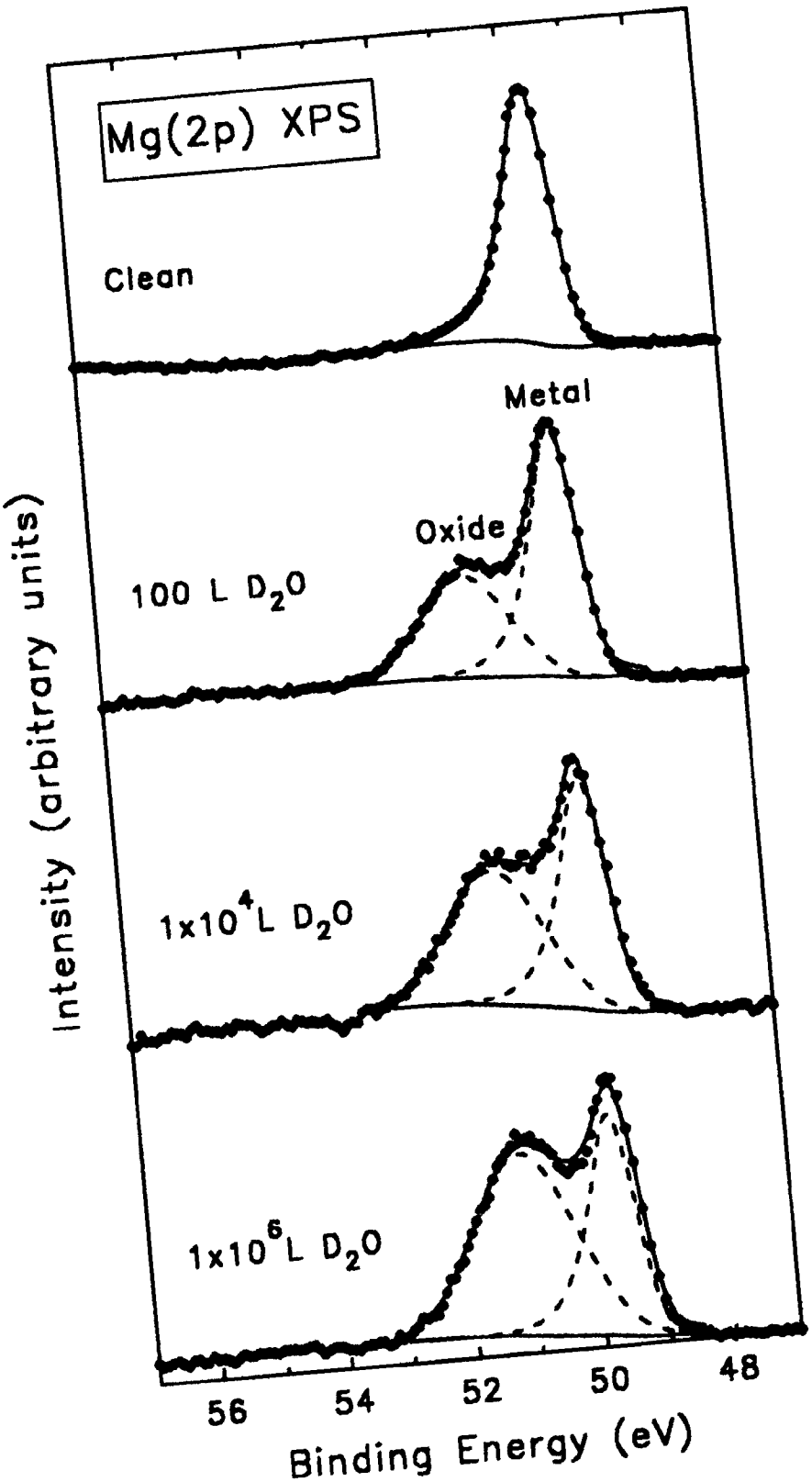
Mg(2p) XPS
Clean
Metal
Oxide
100 L D_2O
$1x10^4$L D_2O
$1x10^6$L D_2O
Intensity (arbitrary units)
56
54
52
50
48
Binding Energy (eV)

$$d = \lambda_o \sin\theta \cdot \ln\left(\frac{N_m}{N_o}\,\frac{\lambda_m}{\lambda_o}\,\frac{I_o}{I_m} + 1\right) \qquad (3.9)$$

where: N_m, N_o are the volume densities of metal atoms in the metal and oxide, respectively (cm^{-3}); λ_m, λ_o are the IMFPs of the appropriate photoelectrons in the metal and oxide, respectively (ML); θ is the electron take-off angle; and I_m, I_o are the measured intensities (peak areas) of the metal and oxide photoelectron peaks, respectively.

Estimated densities for MgO yield an N_m/N_o ratio of ≈ 0.8 to 1.0 [3.35]. The density of the oxide film will vary, depending on the degree of hydration. In this study, a constant value of $N_m/N_o = 1.0$ was used. Calculations of IMFP's were performed using the empirical expressions of Tanuma et al. [3.29] and indicated that, for the photoelectrons of interest, the IMFP's in magnesium oxide and magnesium metal were ≈ 14.7 and 16.4 ML MgO respectively (Appendix A). The measurements were made at several electron take-off angles to ensure that the metallic Mg signal did in fact originate from the magnesium substrate and not from any metallic magnesium atoms present in the oxide film. Identical thickness determinations for differing take-off angles confirmed the former assertion.

To measure the intensity ratios of the metal and oxidic Mg(2p) photoelectron peaks, the spectra were fitted with a least-squares routine using a 70% gaussian peak shape for the metallic component and a 100% gaussian shape for the oxidic component. A 35% asymmetry was used on the metallic peak and constraints were placed on the peak

separation and FWHM for each line. A Shirley correction was made to the background under all fitted peaks. Excellent fits of experimental peak shapes were obtained by this method. It should be noted that any lost emission intensity in the main 2p peak because of intrinsic satellites [3.36] has not been taken into account and, consequently, the measured intensity ratios should be considered an upper limit.

The measured I_o/I_m ratios have been used with equation (3.9) to monitor quantitatively the increase in the oxide film thickness for pure magnesium up to an exposure of 1×10^6 L. The results are presented as open squares in Figure 3.6. The previous Auger data have been used to calculate an equivalent oxide film thickness for the early stages of oxide growth. For an homogenous film of thickness d covering the surface, the signal intensity is given by:

$$Mg = Mg^{clean} \cdot \exp(-d/\lambda) \qquad (3.10)$$

Equation (3.10) has been used with the Mg/Mg^{clean} data of Figure 3.3(a) and the fitted escape depth, $\lambda = 1.5$ ML, to calculate the approximate oxide thickness, d, for increasing exposures to D_2O. The results are included as open circles in Figure 3.6. Equation (3.10) assumes that the metal is covered with an uniform, homogeneous oxide layer. Although this is not exactly the case here, as discussed above, useful information can still be obtained. Consequently, the full oxidation behaviour on pure magnesium is realised over almost seven orders of magnitude exposure to D_2O in Figure 3.6. The good agreement between the Auger and XPS results is apparent in the 100 L range.

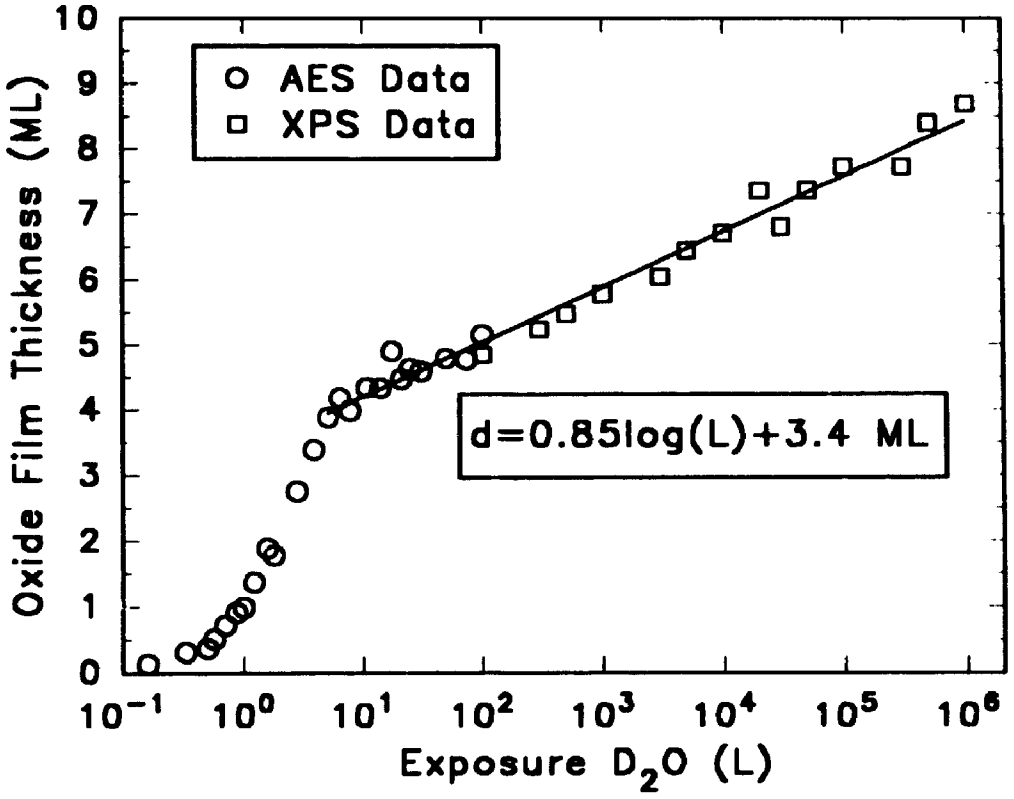

Figure 3.6: The growth of oxide on magnesium exposed to D_2O monitored by AES(○) and XPS(□). The good agreement between the two techniques is apparent in the 100 L range. A logarithmic-type growth expression is realised for exposures ranging from ≈ 5 L to 1×10^6 L D_2O.

From Figure 3.6 it is evident that the logarithmic nature of the slow growth stage after coalescence of the oxide islands has been confirmed for exposures ranging from ≈5 to 1×10^6 L D_2O. These data have been fit by linear regression to yield the following expression:

$$d = 0.85 \log(L) + 3.4 \quad ML \tag{3.11}$$

where L is the exposure in langmuir. Extrapolation of equation (3.11) to 1×10^9 L yields a estimated limiting oxide thickness in water vapour of approximately 11 monolayers of MgO.

In order to gain further insight into the mechanism of oxide growth during the logarithmic regime, the effect of pressure on the growth of oxide on pure magnesium has been studied. Figure 3.7 shows the effect of varying the D_2O partial pressure from 1.3×10^{-4} Pa to 1.3×10^{-2} Pa for increasing exposure times up to 1×10^4 seconds. From Figure 3.7 it is apparent that pressure has little effect on the rate of initial oxidation of magnesium by water vapour at room temperature. This observation suggests that the oxidation process is controlled by the movement of cations through the oxide film from the metal/oxide interface to the oxide/gas interface rather than by the movement of anions in the opposite direction. The reasoning by which this conclusion is drawn is described below.

It is assumed that electron tunneling from the metal/oxide interface to the oxide/gas interface is fast and that it is the ionic processes which occur during low-

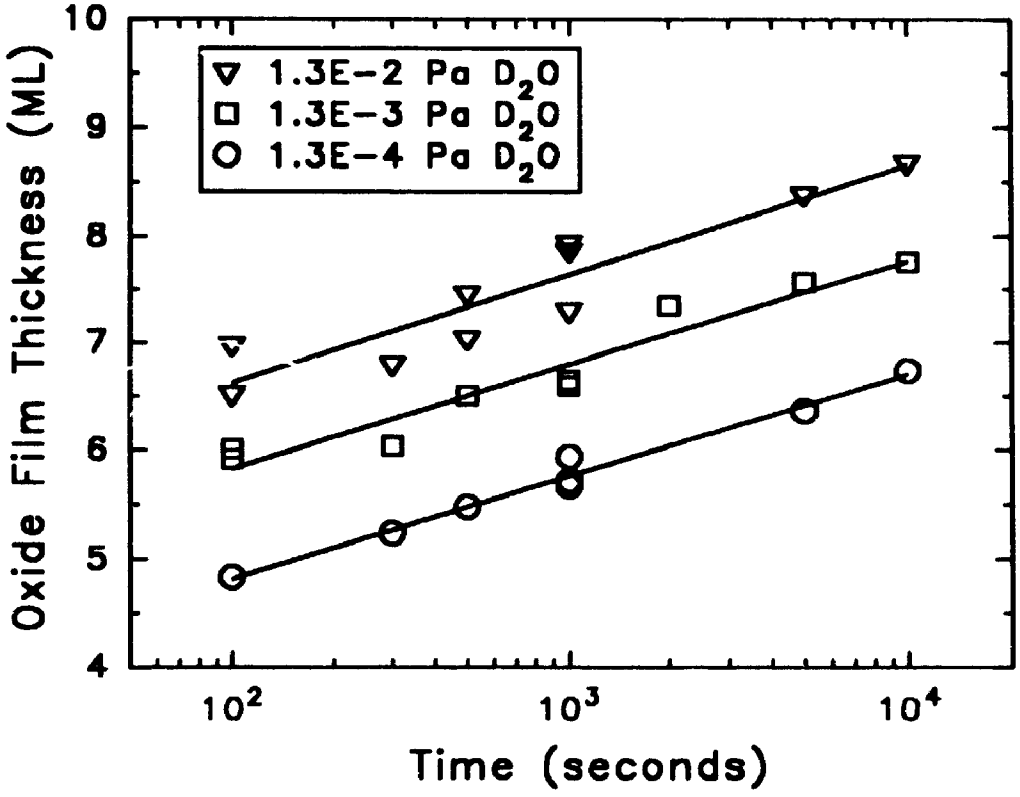

Figure 3.7: The effect of pressure on the growth rate of oxide on magnesium exposed to D_2O. The fact that the rate of bulk oxide thickening is not a strong function of the oxidant partial pressure suggests that the slow growth process is controlled by the movement of cations through the film, from the metal/oxide interface to the oxide/gas interface.

temperature oxidation which are rate-limiting. This assumption is supported by calculations by Fromhold and Cook [3.37] which show that electron transfer in a one-step tunneling process occurs easily for oxide thicknesses less than ≈ 3 nm (≈ 14 ML MgO). If anion movement dominates, a dependence of reaction rate on pressure should be observed. An increased pressure would lead to an increased anion population at the oxide/gas interface and thus an increased number of potentially mobile anions.

The present results point to a negligible pressure dependence. According to elementary gas kinetics, the connection between *exposure* (i.e. pressure × time) and the actual *collision number*, n_s, (collisions/cm^2) is:

$$n_s = \int Q\, dt = \int \frac{P}{(2\pi mkT)^{1/2}}\, dt \qquad (3.12)$$

where Q is the flux of impinging gas molecules (collisions/cm^2/sec); P is the pressure (Pa); m is the mass of the impinging molecule; k is Boltzman's constant and T is the temperature (K). For D_2O at 298 K, we obtain:

$$n_s = 3.42 \times 10^{18}\, Pt \quad (collisions/cm^2) \qquad (3.13)$$

or

$$n_s = 4.55 \times 10^{14} \quad (collisions/cm^2/langmuir) \qquad (3.14)$$

In order to obtain a given exposure value in langmuir, one can either dose the surface at a higher pressure (higher impinging flux) for a shorter time or at a lower pressure (lower impinging flux) for a longer time. If anion movement dominates, it is expected that the higher flux for shorter times would lead to a greater oxide film thickness than the lower flux for longer times (i.e. anion movement would be fast and the rate of thickening would be determined by the anion population, or flux to the oxide/gas interface). This behaviour was, in fact, not observed. For example, an exposure value of 1×10^4 L achieved by dosing at 1.3×10^{-4} Pa for 1×10^4 seconds, at 1.3×10^{-3} Pa for 1×10^3 seconds and 1.3×10^{-2} Pa for 1×10^2 seconds all resulted in comparable oxide thicknesses. It is concluded, therefore, that the oxidation process proceeds by cation movement through the oxide film, with the reaction front being the oxide/gas interface. This conclusion is supported by the TEM results of Deacon et al. [3.38], which demonstrated that dislocation loops at the metal/oxide interface grew in magnesium foils during oxidation. This observation was attributed to the injection of a counterflow of vacancies into the metal as cations were incorporated in the oxide film at the interface.

The fact that transport in the thin MgO film occurs by cation movement is not surprising if one considers that MgO is classified as a network-modifying oxide [3.39]. Network modifiers show little structural near-order and the most mobile defects are slightly bound cations. Network-forming oxides, on the other hand, tend to have a vitreous structure wherein there is a reasonably high degree of short-range order but a lack of long-range order. Such oxides consequently have strongly bound cations and

transport of atoms is mainly accomplished by anions. What *is* surprising, however, is that a logarithmic rate dependence was in fact observed. Generally, it is found that network-modifying oxides tend to form crystalline oxides and it is thus expected that the diffusion of ions would occur rapidly along grain boundaries where the activation energy for movement is less, leading to faster-than-logarithmic kinetics. It is possible here that it is the presence of hydrogen in the film that may play a role in oxide disordering and consequently produce the observed oxidation kinetics. This will be discussed more thoroughly below.

The chemistry of the oxide films grown on magnesium during increasing exposures to D_2O was monitored by carefully examining the changes in the core-level O(1s) XPS signal (Figure 3.8). From Figure 3.8 it is clear that the oxygen atoms in the thin-film oxide are present in at least two different chemical environments. A similar observation has been reported for other magnesium oxidation studies [3.5,3.10-3.13]. The low binding energy (LBE) peak at approximately 531.0 eV has been attributed to lattice MgO oxygen atoms [3.5,3.10-3.13]. The high binding energy (HBE) component at 533.2 eV is more ambiguous but has been attributed to hydroxide [3.12] or hydroxyl [3.13] species or to atoms acting as precursors to further oxide growth [3.5]. The possibility that this HBE peak is due to molecularly adsorbed water is unlikely, since such species usually exhibit an O(1s) peak $\approx$ 4 eV above the O(1s) peak from oxide surfaces [3.12,3.40].

It is interesting to note that the relative contribution from the HBE O(1s) component increases with increasing exposure to D_2O (Figure 3.8). The LBE peak

Figure 3.8: Representative high-resolution O(1s) core-level XPS spectra of the clean magnesium surface and the same surface exposed to the indicated exposures of D_2O. Two distinct types of oxygen are observed. The low binding energy (LBE) component at 531.0 eV is assigned to lattice MgO oxygen atoms and the high binding energy (HBE) component at 533.2 eV is ascribed to oxygen in a "defective" chemical environment.

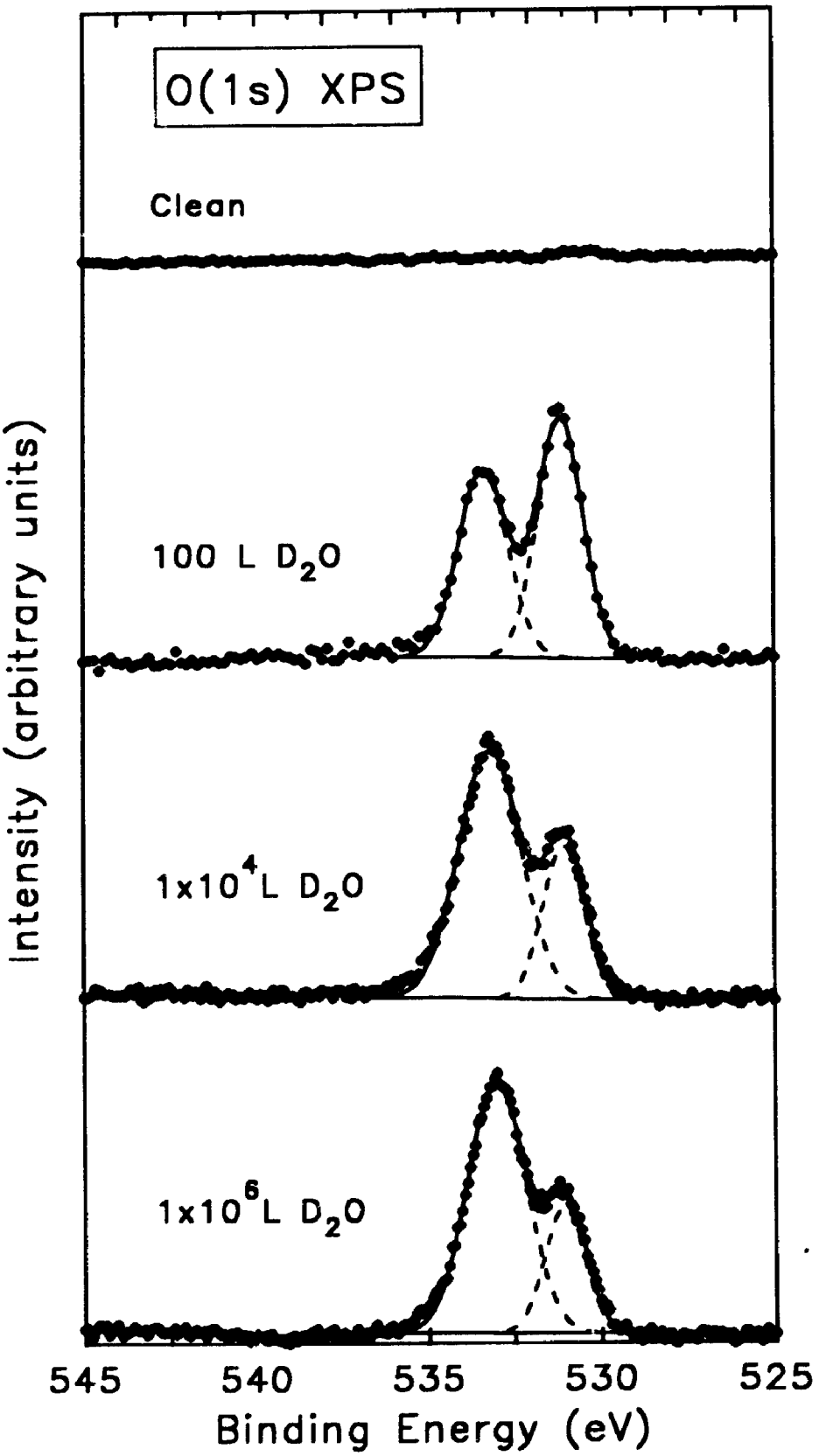
O(1s) XPS
Clean
100 L D_2O
$1x10^4$L D_2O
$1x10^6$L D_2O
Intensity (arbitrary units)
545
540
535
530
525
Binding Energy (eV)

remains narrow (FWHM ≈ 1.3 eV) with increasing exposure whereas the HBE peak exhibits some broadening, from FWHM ≈ 1.6 eV at 100 L D_2O to FWHM ≈ 2.2 eV at 1×10^6 L D_2O exposure. The intensity ratio, I_{HBE}/I_{LBE} increases from 0.8 to 3.0 across this range. There were no detectable shifts in the binding energy positions of either peak.

It is possible that the increasing HBE contribution is due to the development of increasing hydroxyl or hydroxide contributions with exposure to water vapour However, when the ratios of oxidised magnesium/oxygen atoms were measured using the corrected intensity ratios it was found that they fell within a ratio of oxidized Mg/O = 1.15 ± 0.07, independent of exposure. Any significant hydroxide or hydroxyl presence would be expected to produce a ratio of oxidized magnesium to oxygen atoms of less than one [3.41].

In order to obtain further information concerning the role of hydrogen in the oxide film, absolute surface coverages of deuterium were measured by NRA for increasing exposures to D_2O. The results are presented in Figure 3.9. From Figure 3.9 it is evident that the uptake of deuterium (hydrogen) in the oxide film with exposure to D_2O follows the same general trend as that of oxygen (Figure 3.3(b)). The uptake is rapid until approximately 5 L D_2O exposure, beyond which a logarithmic type uptake profile dominates. However, when these data were compared to the corresponding calculated surface concentrations of oxygen atoms (using a value of 1.13×10^{15} oxygen atoms/cm^2 per monolayer of MgO [3.13]) it was found that the deuterium levels in the film were not nearly sufficient to account for the large HBE O(1s) XPS component.

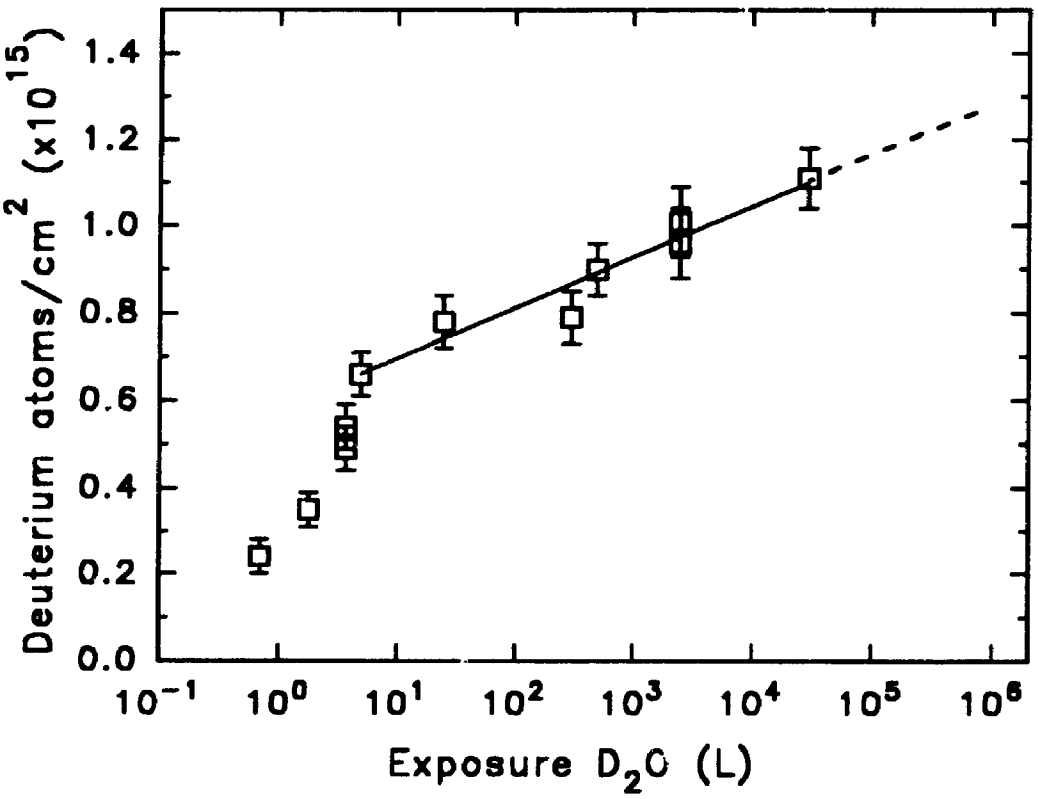

Figure 3.9: The absolute surface concentration of deuterium atoms on magnesium during increasing exposures to D_2O as determined by Nuclear Reaction Analysis (NRA).

Figure 3.10 shows the ratio of deuterium to oxygen atoms (D/O) in the oxide film for increasing exposures to D_2O. The ratio was found to drop rapidly from D/O = 0.30 at $\approx$0.75 L D_2O to D/O = 0.15 at $\approx$5 L D_2O. The deuterium to oxygen ratio then remained essentially constant during longer exposures. It is apparent, therefore, that the HBE O(1s) XPS component, which increased with increasing exposure to D_2O, cannot be due to a significant extent to the presence of hydroxide or hydroxyl species in the oxide film. If this were indeed the case, the ratio of deuterium to oxygen would be expected to increase with increasing exposures, approaching a limiting value of D/O $\approx$ 1.0.

Some other interesting observations were made when the specimen was allowed to oxidise slowly under a low partial pressure of residual water vapour in the XPS analytical chamber (Figure 3.11). Figure 3.11 shows that the LBE O(1s) component develops ahead of the HBE peak at an initial binding energy of 530.5 eV. The development of the LBE peak prior to the HBE peak has also been observed for Mg(0001) surfaces exposed to O_2 [3.5]. The binding energy of the LBE component was found to increase with exposure to the limiting value of 531.0 eV. This observation suggests that initially the LBE component likely represents the chemisorbed oxygen atoms originating from the dissociated water molecules that first strike the clean surface. The fact that their binding energy is very close to that of the bulk oxide suggests that the initially adsorbed oxygen atoms may penetrate and be incorporated into the magnesium substrate. Since both Mg and MgO have hcp symmetry, a similar chemical state is

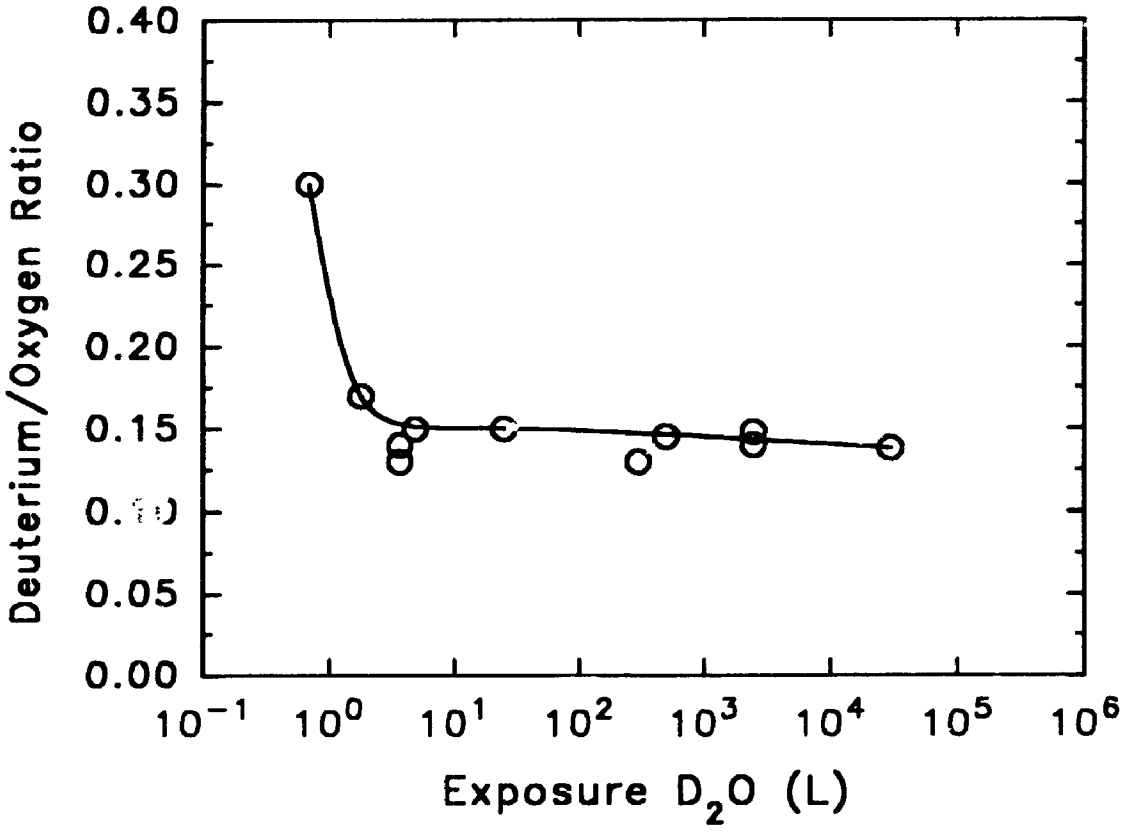

Figure 3.10: The ratio of deuterium to oxygen atoms in the oxide film during increasing exposures to D_2O. It is clear that hydrogen is present in the film only in small relative amounts.

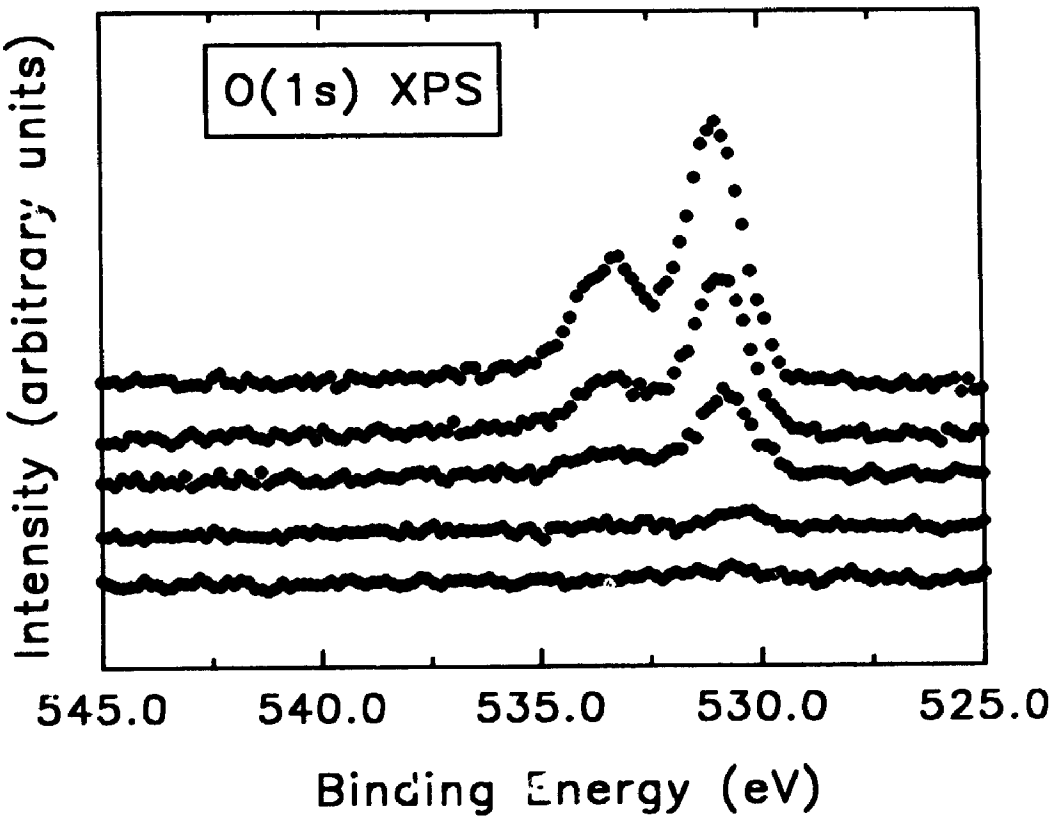

Figure 3.11: High-resolution O(1s) core-level XPS spectra of a magnesium surface allowed to oxidise under a low partial pressure of residual water vapour. The LBE XPS component develops prior to the HBE component.

expected, thus giving an almost constant binding energy of the deep O(1s) level. Oxygen incorporation into magnesium single crystal surfaces has been suggested as the initial step in the oxidation of such surfaces with O_2 [3.4].

It was not possible to determine exactly the exposure values for the spectra in Figure 3.11 since the quadrupole mass spectrometer was not connected to the analytical chamber. However, concurrent measurements of the Mg(2p) XPS signal suggested that the HBE O(1s) peak first appeared (with binding energy 533.3 eV) after the oxide film had grown to an average thickness of approximately 0.5 ML MgO. This value corresponds roughly to the onset of the oxide nucleation and growth stage as determined by AES measurements. The ratio I_{HBE}/I_{LBE} then developed quickly to a nearly constant value of about 0.4 to 0.5 until approximately four monolayers average film thickness. Beyond this value, which corresponds to bulk thickening as determined by AES, the ratio I_{HBE}/I_{LBE} began to increase.

These observations, coupled with the NRA experiments, permit an interpretation of the HBE O(1s) XPS component and the oxidation process itself. It is clear that the impinging water molecules dissociate rapidly on the clean magnesium surface, leading to the chemisorption of oxygen atoms. These chemisorbed atoms then penetrate beneath the topmost magnesium layer, leading to the initial appearance of the LBE O(1s) XPS component at 530.5 eV. It is likely that it is these incorporated oxygen atoms that then act as nucleation sites for the oxide islands. Once the islands begin to assemble, hydroxyl species originating from the dissociated water molecules can attach themselves to the growing islands, leading to the appearance of the HBE O(1s) XPS component at

533.3 eV binding energy. After the islands coalesce at an average height of four monolayers, the deuterium (hydrogen) content was observed to continue to increase, but at a much diminished rate, leading to a nearly constant ratio of deuterium to oxygen atoms in the film.

As bulk thickening proceeds, the HBE component increases in intensity relative to the LBE component. It is postulated here that this behaviour is due to the growth of a highly defective oxide and that the HBE component in this case is due to oxygen atoms present in a "defective" environment, probably in sites adjacent to interstitial metal cations. The fact that logarithmic kinetics were observed suggests that the oxide film is not fully crystalline, but rather exhibits little long-range order. The presence of hydrogen in the film can lead to increased structural flexibility by forming metal-hydrogen or metal-hydroxyl bonds in addition to the normal metal-oxygen bonds [3.39]. This then leads to an increased tendency to non-crystallinity and may account for the proposed defective nature of the oxide film formed on magnesium.

This conclusion was supported by annealing experiments. When magnesium already exposed to 1×10^6 L D_2O was heated from 298 K to 473 K in vacuum, the LBE O(1s) XPS component increased in intensity and the HBE O(1s) XPS component decreased in intensity (Figure 3.12). In addition, the oxide film increased in thickness with heating. Figure 3.13 shows the effect of annealing *in vacuo* on the measured HBE/LBE ratio and oxide film thickness. This behaviour supports the hypothesis that the film is highly defective, with many oxygen atoms occupying "defective" positions. As the specimen is heated, the oxygen atoms can diffuse more easily, leading to

Figure 3.12: High-resolution O(1s) and Mg(2p) XPS spectra of a magnesium surface exposed to 1×10^6 L D_2O and then annealed at the indicated temperatures for one hour. The annealing results in a decrease in the HBE O(1s) XPS component and a concurrent thickening of the oxide film.

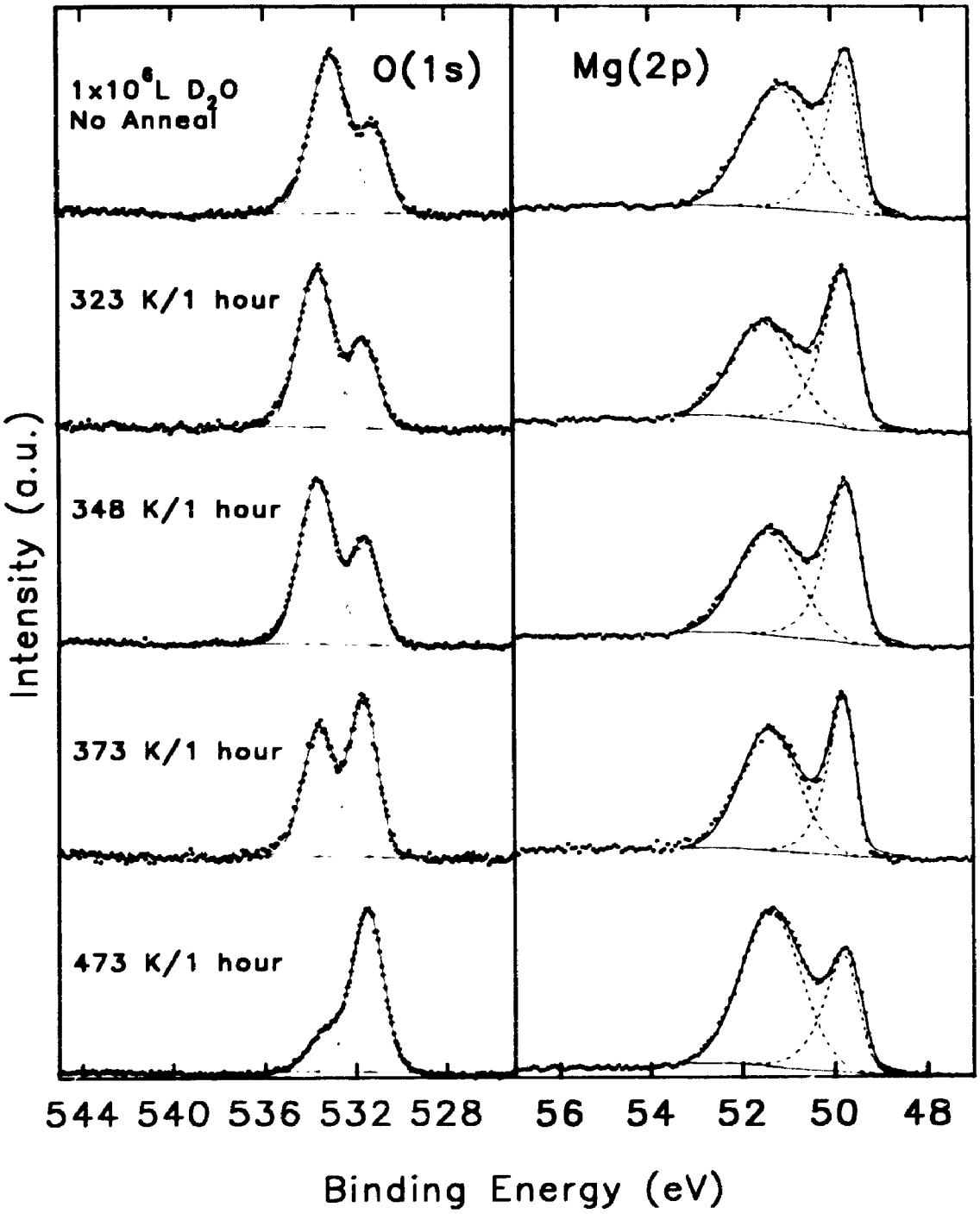
O(1s)
Mg(2p)
1x10⁶L D₂O
No Anneal
323 K/1 hour
348 K/1 hour
373 K/1 hour
473 K/1 hour
Intensity (a.u.)
544 540 536 532 528
56 54 52 50 48
Binding Energy (eV)

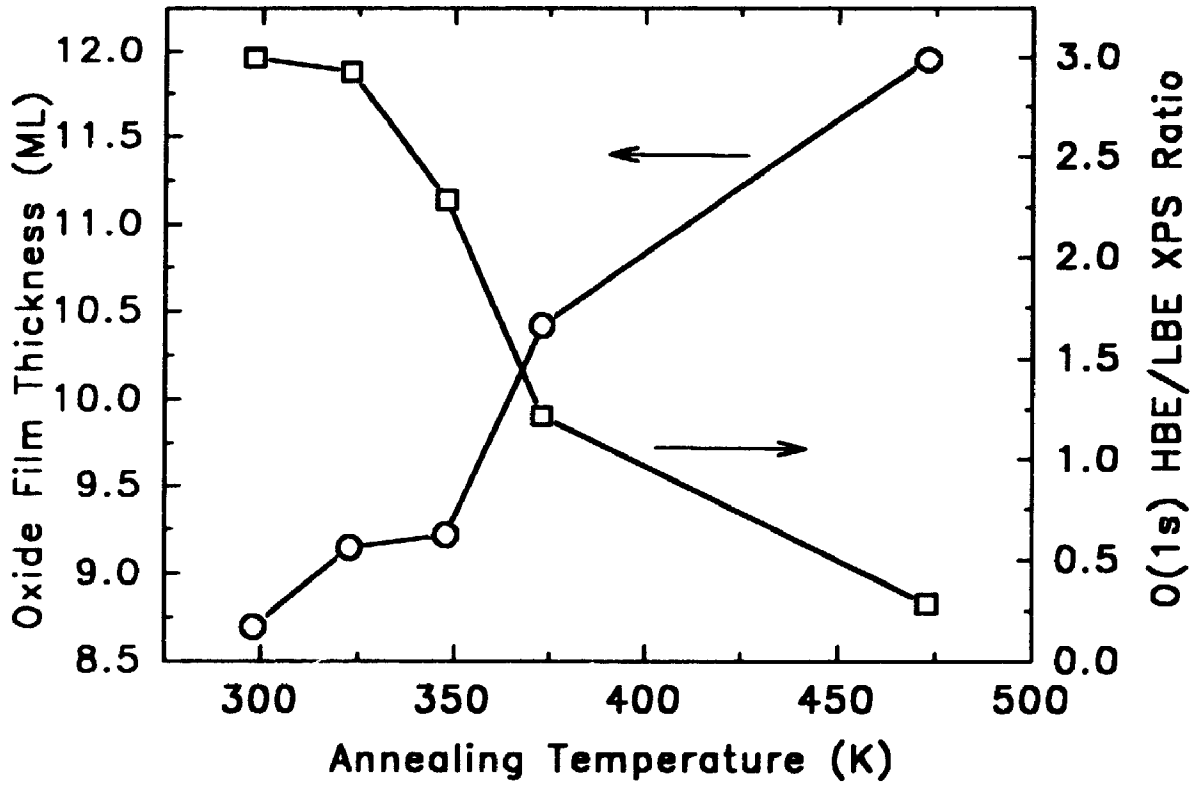

Figure 3.13: The effect of annealing *in vacuo* on the measured O(1s) HBE/LBE ratio and the calculated oxide film thickness.

increased "ordering" of the oxide and thus a decreased HBE O(1s) contribution and an increased oxide film thickness.

3.4 Conclusions

Several conclusions can be drawn from this work:

1. Three stages of early oxide growth by water vapour on pure magnesium have been recognised: a chemisorption stage during D_2O doses up to $\approx$ 0.7 L; a rapid oxide nucleation and growth stage which is complete by 5 L at an average island height of four monolayers and a slow growth stage after coalescence of the islands;

2. Modelling results suggest that the rate of oxygen uptake on pure magnesium surfaces is faster on grain faces that have more open-packed, higher index crystallographic orientations, particularly in the second (island nucleation and growth) stage;

3. The slow growth stage can be adequately described by a logarithmic-type growth law, suggesting a limiting oxide thickness in water vapour of approximately 11 monolayers of MgO. The slow growth process is controlled by the movement of metal cations through the oxide film from the metal/oxide interface to the oxide/gas interface;

4. Hydrogen is present in the oxide film in relatively small amounts. The role of hydrogen in the film is likely to provide structural flexibility leading to the growth of a highly defective oxide;

I would like to thank Dr. Vesna Mitrovic-Scepanovic and the Metals Technology Laboratories (MTL) of the Canada Centre for Mineral and Energy Technology (CANMET), for supplying all of the materials used in this thesis. I also thank Dr. Keith Griffiths and Dr. Willy Lennard of Interface Science Western for their capable help in performing and interpreting the NRA experiments and Dr. Gino Palumbo of the Ontario Hydro Research Laboratories in Toronto for his help in collecting and interpreting the EBSD patterns.

Finally, I wish to thank Surface Science Western for financial support in the form of a Research Assistantship, the Department of Materials Engineering for support in the form of several Teaching Assistantships and the Faculty of Graduate Studies of the University of Western Ontario for support in the form of a Graduate Research Award and a Graduate Research Fellowship.

5. Detailed XPS spectra of the oxide film show two distinct types of oxygen: one of these is assigned to oxygen atoms in normal MgO lattice positions; the other is ascribed to oxygen atoms in a "defective" chemical environment.

References

[3.1] P.A. Thiel and T.E. Madey, Surf. Sci. Rep. 7 (1987) 211.

[3.2] B.E. Hayden, E. Schweizer, R. Kötz and A.M. Bradshaw, Surf. Sci. 111 (1981) 26.

[3.3] R. Kötz, B. Hayden, E. Schweizer and A.M. Bradshaw, Surf. Sci. 112 (1981) 229.

[3.4] H. Namba, J. Darville and J.M. Gilles, Surf. Sci. 108 (1981) 446.

[3.5] J. Ghijsen, H. Namba, P.A. Thiry, J.J. Pireaux and R. Caudano, Appl. Surf. Sci. 8 (1981) 397.

[3.6] P.A. Thiry, J Ghijsen, J.J. Pireaux and R. Caudano, J. Electron Spectrosc. Relat. Phenom. 29 (1983) 193.

[3.7] P.A. Thiry, J. Ghijsen, R. Sporken, J.J. Pireaux, R.L. Johnson and R. Caudano, Phys. Rev. B. 39 (1989) 3620.

[3.8] S.A. Flodström and C.W.B. Martinsson, Surf. Sci. 118 (1982) 513.

[3.9] M.A. Barteau and X.D. Peng, Mat. Chem. Phys. 18 (1988) 425.

[3.10] X.D. Peng and M.A. Barteau, Surf. Sci. 233 (1990) 283.

[3.11] G.C. Allen, P.M. Tucker, B.E. Hayden and D.F. Klemperer, Surf. Sci. 102 (1981) 207.

[3.12] J.C. Fuggle, L.M. Watson, D.J. Fabian and S. Affrossman, Surf. Sci. 49 (1975) 61.

[3.13] J.C. Fuggle, Surf. Sci. 69 (1977) 581.

[3.14] D. Norman and D.P. Woodruff, J. Vac. Sci. Technol. 15 (1978) 1580.

[3.15] A.P. Janssen, R.C. Schoonmaker and A. Chambers, Surf. Sci. 47 (1975) 41.

[3.16] S.A. Flodstrom, C.W.B. Martinsson, G. Kalkoften and C. Kunz, Mater. Sci. Eng. 42 (1980) 31.

[3.17] M.S. Cohen, Acta. Metall. 8 (1960) 356.

[3.18] R.R. Addiss, Jr., Acta. Metall. 11 (1963) 129.

[3.19] J.A. Schultz, M.H. Mintz, T.R. Schuler and J.W. Rabalais, Surf. Sci. 146 (1984) 438.

[3.20] D.R. Baer and M.T. Thomas, Appl. Surf. Sci. 26 (1986) 150.

[3.21] J.H. Scofield, J. Electron Spectrosc. Relat. Phenom. 8 (1976) 129.

[3.22] A.P. Janssen, R.C. Schoonmaker, J.A.D. Mattew and A. Chambers, Solid State Commun. 14 (1974) 1263.

[3.23] P.H. Holloway, J. Vac. Sci. Technol. 18 (1981) 653.

[3.24] P.H. Holloway and J.B. Hudson, Surf. Sci. 45 (1974) 123, 141.

[3.25] D.F. Mitchell, D.P. Sewell and M. Cohen, Surf. Sci. 69 (1977) 310.

[3.26] C. Palacio, H.J. Mathieu and D. Landolt, Surf. Sci. 189/190 (1987) 168.

[3.27] J.M. Sanz, C. Palacio, Y. Casas and J.M. Martinez-Duart, Surf. Interface Anal. 10 (1987) 177.

[3.28] M.P. Seah and W.A. Dench, Surf. Interface Anal. 1 (1979) 2.

[3.29] S. Tanuma, C.J. Powell and D.R. Penn, Surf. Interface Anal. 17 (1991) 911.

[3.30] J.A. Venables, G.D.T. Spiller and M. Hanbuken, Rep. Prog. Phys. 47 (1984) 399.

[3.31] G.E. McGuire, in: Applied Electron Spectroscopy for Chemical Analysis, H. Windawi and F.F.L. Ho (Eds.) (Wiley, New York, 1982) p.1.

[3.32] C.D. Wagner and P. Biloen, Surf. Sci. 35 (1973) 82.

[3.33] S.P. Kowalczyk, F.R. McFeely, L. Ley, V.T. Gritsyna and D.A. Shirley, Solid State Commun. 23 (1977) 161.

[3.34] B.R. Strohmeier, Surf. Interface Anal. 15 (1990) 51.

[3.35] R.C. Weast (ed), Handbook of Chemistry and Physics, 54th Edition, (CRC Press, Cleveland , 1973).

[3.36] B.I. Lundkvist, Phys. Kondens. Mater. 9 (1969) 236.

[3.37] A.T. Fromhold, Jr. and E.L. Cook, J. Appl. Phys. 38 (1967) 1546; Phys Rev. 158 (1967) 600.

[3.38] C. Deacon, M.H. Loretto and R.E. Smallman, Mater. Sci. Technol. 1 (1985) 344.

[3.39] F.P. Fehlner, Low Temperature Oxidation: The Role of Vitreous Oxides (Wiley, New York, 1986).

[3.40] A.F. Carley, S. Rassias and M.W. Roberts, Surf. Sci. 135 (1983) 35.

[3.41] N.S. McIntyre, unpublished results.

CHAPTER 4

INFLUENCE OF Ar^+ ION BOMBARDMENT ON THE INTERACTION OF WATER VAPOUR WITH PURE MAGNESIUM SURFACES

"In classical solid state physics the surface was considered to be an invention of the devil...However, the devil had a son, who in trying to outdo his father, invented the surface defects."
- Klaus Wandelt, Universität Bonn, Germany.

4.1 Introduction

It has long been recognised that the presence of surface defects (steps, kinks, vacancies, impurities) can alter the reactivity of a surface. The properties of surface defects are usually investigated using well-oriented, stepped single crystals which have a reasonably well-defined step geometry and step density [4.1,4.2]. Such studies consistently show that step (edge) sites are more reactive than terrace (flat) sites. However, less attention has been focussed on defects generated by ion bombardment, despite the fact that the different distribution of structural defects introduced on an ion-bombarded surface may significantly change the surface chemistry. The damage introduced by keV Ar^+ bombardment of a metal surface is expected to consist of vacancies, vacancy clusters, vacancy-argon complexes, interstitial agglomerates and dislocation loops [4.3].

The initial adsorption and reaction of water with metal surfaces is of fundamental importance to the understanding of such processes as corrosion-passivation chemistry, electrochemistry and heterogeneous catalysis [4.4]. Typically, surface science

experiments designed to investigate such interactions begin with the preparation of clean surfaces by sputtering with low energy inert gas ions. The damage introduced by particle irradiation is then normally removed by annealing in vacuum. The use of such annealing steps is, however, suspect when examining polycrystalline alloys containing low concentrations of a constituent that could segregate to the surface or to the grain boundaries. The purpose of this study has therefore been to evaluate the influence of ion-induced surface damage on the initial interaction of water vapour with polycrystalline magnesium surfaces in order to facilitate comparison with magnesium samples containing very low-level alloying elements, for which no post-sputtering annealing stage is desirable (Chapter 6). The results are, moreover, of more general interest to the understanding of the role of point defects and defect clusters on oxide growth.

Previous studies of water interaction with disordered metal surfaces have been, not surprisingly, mainly limited to vicinal surfaces. Generally, it is observed that atomically rough (stepped) surfaces are more active for water dissociation than atomically smooth (close-packed) surfaces [4.4]. A limited number of investigations have also been performed on surfaces disordered by ion bombardment. Gonzalez et. al [4.5] studied the effect of Ar^+ bombardment on the oxidation of Fe(110) by O_2 and H_2O and concluded that sputtering damage destroyed the ability of H_2O to form a sub-monolayer protective layer and facilitated the formation of bulk oxide. Baer and Thomas [4.6], in contrast, demonstrated that the passivating effect of H_2O on polycrystalline Fe was not destroyed by prior Ar^+ bombardment. An electron beam (5 keV, 50 nA), however, was found to enhance oxidation and breakdown of the protective film. Finally, Weir [4.7] studied H_2O

adsorption on ion bombarded Fe(001) up to 1×10^{17} L and at elevated temperatures (413 K), and found that nucleation of FeO and bulk oxide formation was enhanced by the sputtering process.

The initial interaction of water vapour with pure polycrystalline magnesium surfaces was examined in detail in Chapter 3. The fitting of AES data to theoretical models suggested that the initial reaction with water vapour resulted in a three stage oxidation behaviour: dissociative chemisorption during doses up to approximately 0.7 langmuir (L); oxide nucleation and island growth until about 5 L and slow, diffusion-controlled oxide growth following coalescence of the oxide islands. In addition, the rate of initial oxygen uptake was found to be faster on grain faces that exhibited more open-packed, higher-index orientations, as compared to the more close-packed, near-basal grains, particularly in the nucleation and island growth stage. Interestingly, the observed differences in oxygen uptake behaviour on various grain faces were found to disappear when the surface had been sputtered with excessive doses of Ar^+ ions ($> \approx 1 \times 10^{17}$ ions/cm^2). The rate of oxygen uptake was lowered for all grain faces after excessive sputtering. It was suggested that the high ion fluences likely caused significant defects to dominate the surface reactivity. The present results confirm this assumption. The presence of relatively large concentrations of implanted argon atoms at elevated ion doses was found to reduce significantly oxygen uptake on magnesium surfaces exposed to water vapour, particularly in the oxide nucleation and island growth regime.

4.2 Experimental

All of the measurements reported in this chapter were made on dark (near basal grains) of high purity magnesium. The *in situ* cleaning procedure described in section 2.3 was, however, modified to include annealing cycles following the initial Ar^+ ion bombardment in an attempt to remove as much of the ion-induced damage as possible. The cleaning procedure therefore consisted of sputtering with 3 keV Ar^+ ions to a maximum dose of 1×10^{16} ions/cm^2 followed by annealing *in vacuo* at temperatures of 450 to 475 K for periods of 30 minutes. This was followed by another brief sputter cycle and a further 30 minute annealing period. A similar procedure was found to produce sharp LEED patterns on Mg(0001) surfaces [4.8].

After cleaning, surface damage was created by bombarding the specimens at room temperature with Ar^+ ions at energies ranging from 1 to 5 keV and fluences ranging from $\theta = 10$ to $\theta = 2000$ ions/surface atom. Here, $\theta = 1$ represents an ion dose of one argon ion, on the average, per surface magnesium atom, where the surface density of Mg(0001), 1.1×10^{15} atoms/cm^2, is assumed. The ion currents were measured using a standard Faraday cage and the ion beam was rastered over a relatively large area in order to minimise the possible diffusion of material from outside the bombarded region. The beam intersected the surface at a normal angle of 45 degrees. The high-purity (research grade) argon was dynamically evacuated by a turbomolecular pump.

The clean, disordered surfaces were then exposed in vacuum to calibrated doses of deuterated water vapour at room temperature for exposures up to 20 L. During

dosing, the D_2O partial pressure was maintained in the range of 1.3×10^{-6} Pa. Auger spectra of the clean and water-dosed surfaces were obtained using a 3 keV electron beam energy and electron currents $\leq$ 30 nA in order to minimise electron beam-induced oxidation, as described in Chapter 3. Electron beam effects were again minimised by disabling all filaments, except the ion pressure gauge, during the water dosing. It was possible to collect the required spectra within about 30 seconds of exposing the samples. The principal features of the derivative Auger spectrum of the water-dosed magnesium are the $O(K_1L_{23}L_{23})$ transition at 510 eV, the metallic $Mg(L_{23}VV)$ transition at 45 eV and the oxidic $Mg(L_{23})O(L_{23})O(L_{23})$ transition at 34 eV (Chapter 3). In order to avoid electron instabilities, the oxygen concentration at the surface was monitored by measuring the ratio of the peak-to-peak amplitudes of the $O(K_1L_{23}L_{23})$ to the metallic $Mg(L_{23}VV)$ Auger signals. Experience has shown that, for a given exposure condition, the ratio O(KLL)/Mg(LVV) was repeatable to within $\pm 10\%$.

A limited number of X-ray Photoelectron Spectroscopy (XPS) measurements were made on the saturated oxide films. XPS spectra were obtained using a Surface Science Laboratories SSX-100 spectrometer using AlK_α radiation, as described previously.

4.3 Results

4.3.1 Effect of Ion Dose

Figure 4.1 shows the evolution of the ratio of the peak-to-peak amplitude of the O(KLL) and Mg(LVV) AES signals as a function of D_2O exposure for different 3 keV Ar^+ irradiation doses. The solid line in Figure 4.1 represents data obtained previously for samples prepared without a post-sputtering annealing stage. The total Ar^+ ion dose for these latter specimens fell within the range of $20 \leq \theta \leq 50$ ions/surface atom (i.e. doses $< \approx 5 \times 10^{16}$ ions/cm^2). It should be noted that it was not possible to obtain a kinetic curve for the annealed surface with no ion dose, because during the cool-down period following the final anneal cycle approximately four monolayers (ML) of MgO formed on the surface by reaction with the residual water vapour present in the vacuum chamber. (The duration of the cool-down period was approximately 12 hours). This thin layer was quickly removed during the subsequent damage-inducing bombardment treatment.

From Figure 4.1 it is evident that the oxygen uptake curves for surfaces receiving various amounts of radiation damage coincide for D_2O exposures up to $\approx$ 0.5 to 0.75 langmuir and separate above this value. This exposure range corresponds approximately to the completion of the dissociative chemisorption stage and to the beginning of the surface oxide nucleation and growth stage, as previously modelled (Chapter 3). It is apparent, therefore, that the initial chemisorption of water vapour on magnesium is little

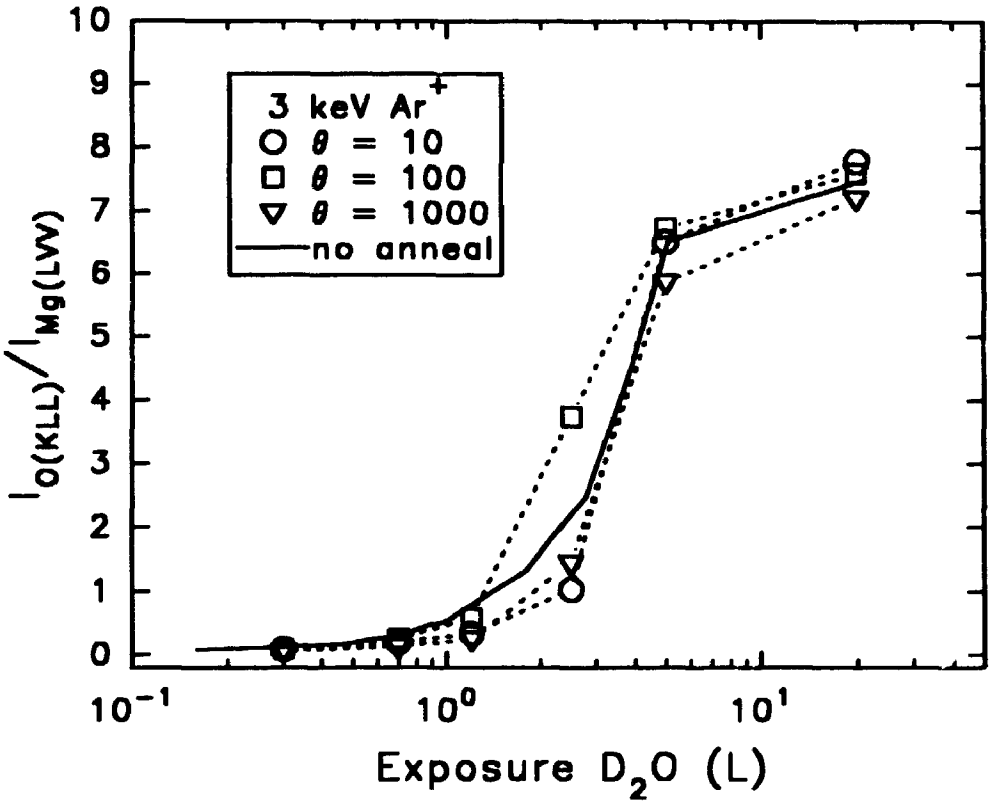

Figure 4.1: The growth of oxide on magnesium surfaces exposed to water vapour for different total Ar^+ ion bombardment doses at 3 keV. The solid line represents data obtained previously for samples prepared without a post-sputtering annealing stage.

affected by Ar^+ bombardment. However, the intermediate stage of nucleation and growth of surface oxide *is* strongly affected by the presence of defects created by ion bombardment. This latter effect also appears to be dependent, in a complex manner, upon the total ion dose that the surface receives. As the ion dose increases from low (θ = 10) to intermediate (θ = 100) values, there is a distinct enhancement in the rate of oxide nucleation and growth. At still higher ion doses (θ = 1000), however, the rate of oxide nucleation and growth is again suppressed, leading to near coincidence of the kinetic uptake curves for total ion doses of θ = 10 and θ = 1000 ions/surface atom (Figure 4.1). Finally, at exposures exceeding approximately 5 L D_2O, corresponding to the beginning of the bulk thickening stage of the oxidation process, the uptake curve for the high dose bombardment treatment (θ = 1000) lies somewhat below those for the low and intermediate dose treatments.

In order to gain more insight into the above phenomena, the O(KLL)/Mg(LVV) AES ratio has been carefully monitored as a function of ion bombardment dose at various D_2O exposures. The results are shown in Figures 4.2. From the figure it is clear that the interaction of water vapour with irradiated magnesium surfaces depends markedly upon the total ion dose that the surface receives and that the character of this dependence changes with the level of D_2O exposure. At very short exposures (0.3 L D_2O), the uptake of oxygen is only weakly affected by increasing 3 keV Ar^+ doses, demonstrating an initial small increase in uptake as the irradiation dose increases to $\theta \approx$ 30 to 50, followed by a very slow, monotonous decrease in uptake with higher ion fluences. As the water exposure is increased to intermediate values, this "increase-then-decrease"

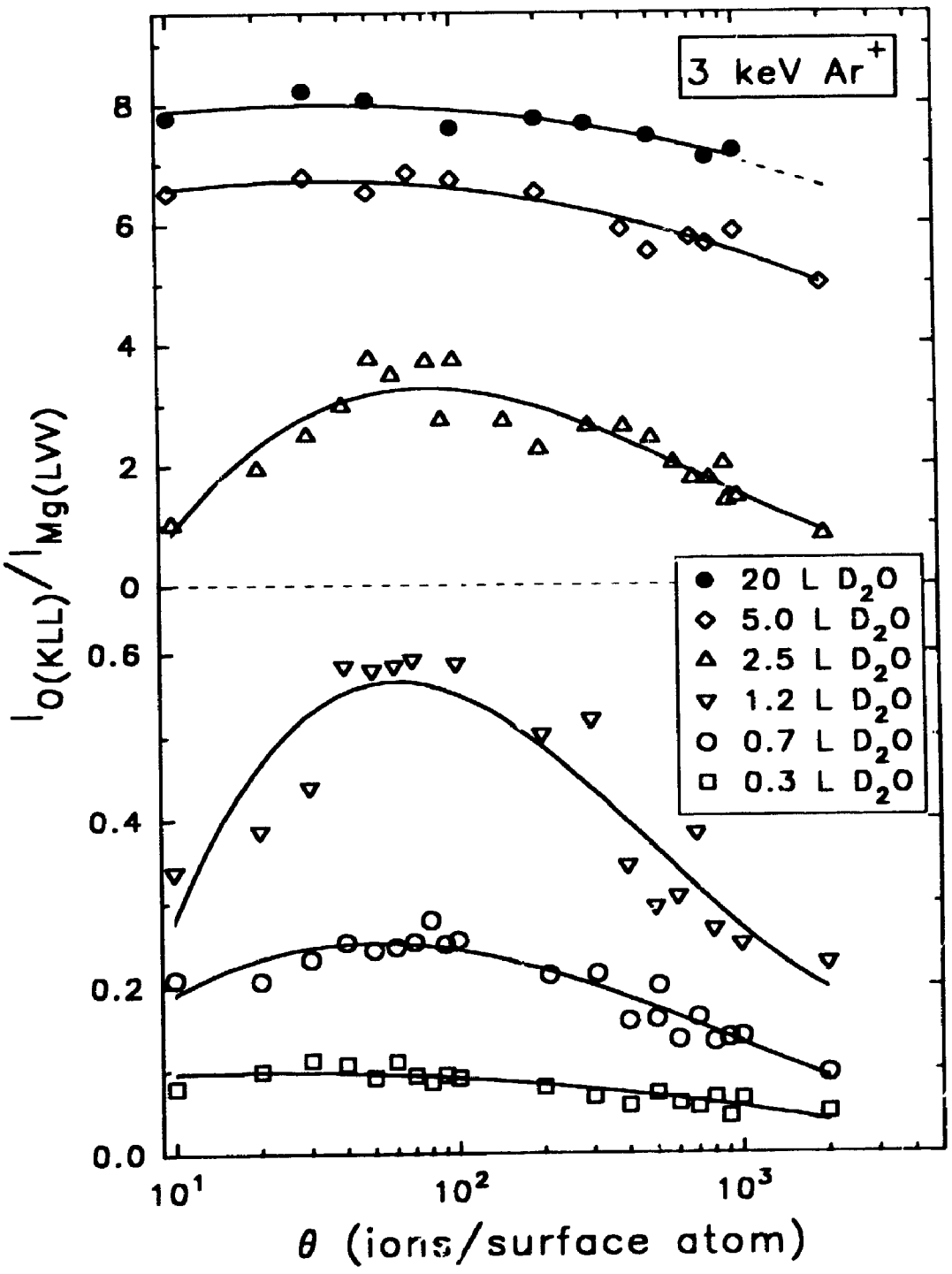

Figure 4.2: The O(KLL)/Mg(LVV) AES ratio as a function of 3 keV Ar^+ ion bombardment dose at various water exposure values. The effect of ion bombardment is greatest for intermediate exposures, corresponding to the oxide nucleation and island growth stage of the oxidation process.

behaviour of oxygen uptake with increasing ion dose becomes systematically more exaggerated. The effect is then largest for exposures of 2.5 L D_2O, where the total amount of detected surface oxygen is substantially increased as the ion bombardment dose is increased from $\theta = 10$ to $\theta \approx 50$ to 100, followed by an equally substantial decrease in total oxygen uptake as the irradiation dose is further increased to $\theta = 200$. Finally, at relatively high water exposures (5 L, 20 L) the total amount of oxygen detected on the surface is again only weakly affected by increasing ion doses. The O(KLL)/Mg(LVV) AES ratio remains constant until the total ion dose exceeds approximately $\theta = 100$ ions/surface atom. Beyond this dose level, the amount of detected oxygen is gradually decreased with increasing irradiation fluences. It is again apparent, therefore, that the effect of ion dose is strongest for the oxide nucleation and island growth stage of the oxidation process.

Some interesting results were obtained when the thin oxide layers formed on various 3 keV Ar^+ irradiated surfaces after 20 L D_2O exposure were sputter depth profiled in the Auger spectrometer. Figure 4.3 shows the dependence of the O(KLL) AES intensity on the time required to sputter the layer formed by a 20 L D_2O exposure on a magnesium surface initially irradiated with doses of $\theta = 10$, 100 and 1000 ions/surface atom. The sputtering was performed with 1 keV Ar^+ ions at a current density of 6 $\mu A/cm^2$. It is evident that after several surface layers have been removed, the oxygen content in the deeper layers remains higher in the specimens initially receiving a larger total Ar^+ irradiation dose ($\theta = 1000$). This occurs despite the fact that the total O(KLL)/Mg(LVV) ratio was observed to decrease with excessive bombardment

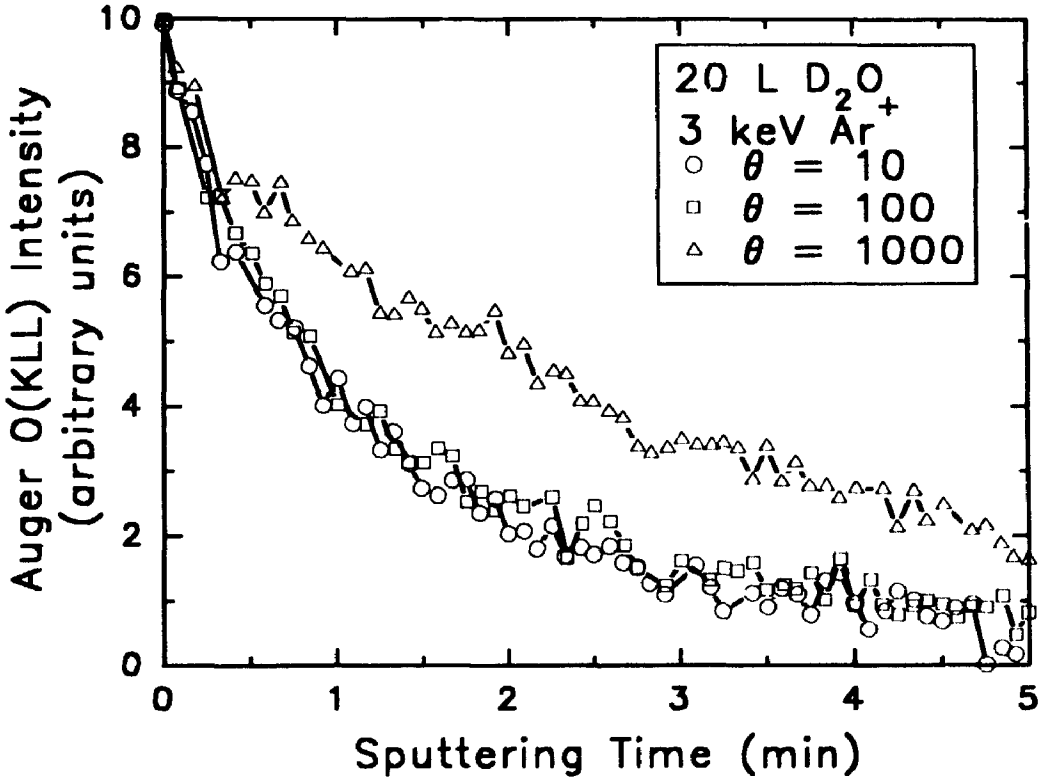

Figure 4.3: The dependence of the O(KLL) AES ratio on the time required to sputter the layer formed by a 20 L D_2O exposure on magnesium surfaces initially irradiated with various 3 keV Ar^+ ion doses. Sputtering was performed with 1 keV Ar^+ ions at a current density of 6 $\mu A/cm^2$.

doses (20 L, Figure 4.2). This suggests, therefore, that the increased damage introduced into the surface layers of magnesium bombarded with high doses of Ar^+ ions may result in easier penetration of oxygen atoms into the lattice, thus leading to a "wider" metal/oxide interface.

Further information regarding the relative number of oxygen atoms in the subsurface layers compared to the surface layers was obtained by monitoring both the Mg(LVV) AES transition at 45 eV and the Mg(KLL) AES transition at 1186 eV for different total Ar^+ doses and D_2O exposures. Since the Mg(LVV) Auger electrons are of much lower kinetic energy than the Mg(KLL) Auger electrons, their inelastic mean free path (IMFP) and thus their escape depth, λ, is significantly shorter. The IMFP's of the various Auger and photoelectrons relevant to this study were calculated using the inelastic scattering model of Tanuma et al [4.9] and are presented in Appendix A.

The O(KLL)/Mg(LVV) AES ratio therefore characterises the number of oxygen atoms at the surface and the O(KLL)/Mg(KLL) AES ratio characterises the number of oxygen atoms in the subsurface layers. Hence, the ratio of Mg(LVV)/Mg(KLL) Auger intensities characterises the relative concentration of oxygen atoms in the subsurface layers compared to the concentration of oxygen atoms at the surface for a thin oxide overlayer on magnesium. Figure 4.4 shows the evolution of this ratio for increasing total 3 keV Ar^+ doses for exposures of 0.3 L and 20 L D_2O. From the figure it is clear that, for an exposure of 20 L D_2O, increasing initial doses of 3 keV Ar^+ ions lead to an increasing penetration of oxygen atoms into the magnesium substrate, consistent with the above depth profiling data. In addition, it is apparent that for low D_2O exposures of 0.3

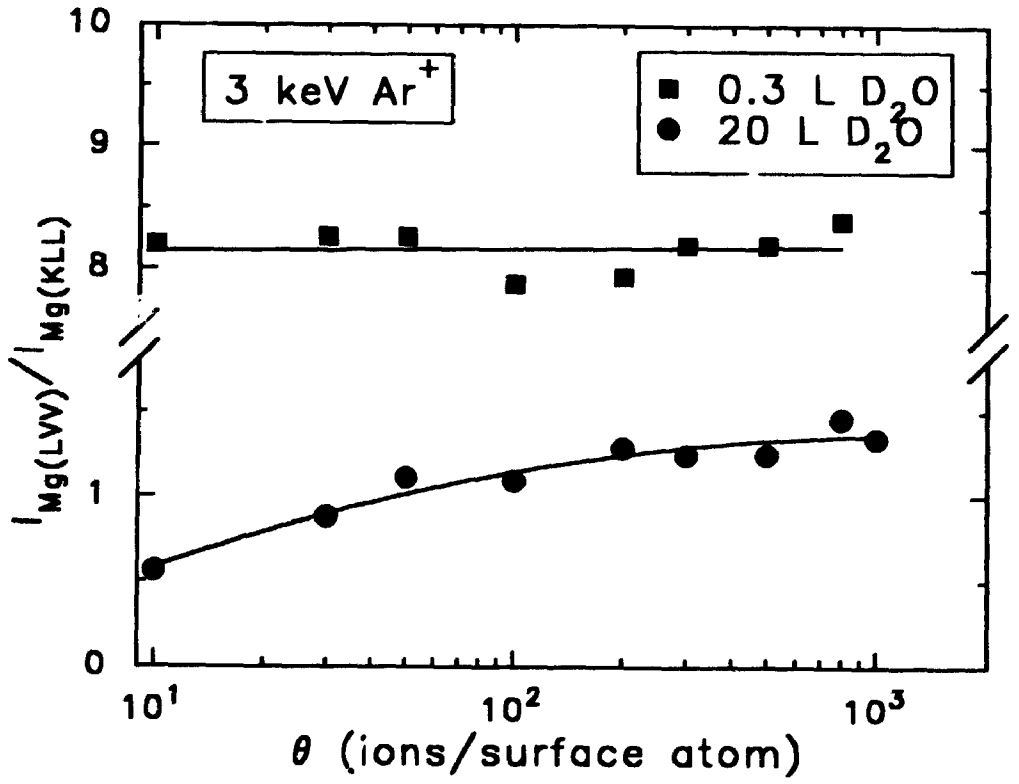

Figure 4.4: The evolution of the Mg(LVV)/Mg(KLL) AES ratio for increasing total 3 keV Ar^+ ion doses for exposures of 0.3 L and 20 L D_2O. The Mg(LVV)/ Mg(KLL) ratio characterises the relative concentration of oxygen atoms in the subsurface layers compared to the near-surface layers.

L (i.e. chemisorption regime), any penetration of oxygen with increasing ion fluences is insignificant. The ratio of Mg(LVV)/Mg(KLL) AES signals remains constant for these latter exposures across the entire ion dose range.

In order to examine the effect of Ar^+ ion bombardment on the long-time oxidation behaviour of magnesium, X-ray Photoelectron Spectroscopy (XPS) was employed. By examining the core-level Mg(2p) and O(1s) XPS lines, it is possible to assess the oxide film thickness and the oxide film chemistry respectively (Chapter 3). Because the photoelectrons of interest are of relatively high kinetic energy (i.e. relatively long IMFP) as compared to the corresponding Auger electrons (Appendix A), information can be obtained for greater total film thicknesses. Figure 4.5 shows the high-resolution O(1s) and Mg(2p) XPS spectra of a magnesium sample initially disordered by 3 keV Ar^+ ions at total fluences of θ = 10, 100 and 1000 ions/surface atom. The spectra were collected from saturated oxide films, obtained by exposing the clean, disordered surfaces to ≈ 1000 L D_2O and then several minutes of air at atmospheric pressure. The thicknesses of the oxide layers were determined by measuring the intensity ratios of the oxidic (Mg^{2+}) to the metallic (Mg^o) XPS peaks, as described previously, and indicated that increasing irradiation doses did not lead to any detectable changes in the thickness of the saturated oxide films. The saturated film thickness for each case in Figure 4.5 was calculated to be approximately 11 monolayers of MgO (≈2.3 nm), in good agreement with that estimated previously (Chapter 3). These results are significant in that they clearly show that, although the degree of initial disorder of the magnesium surface results

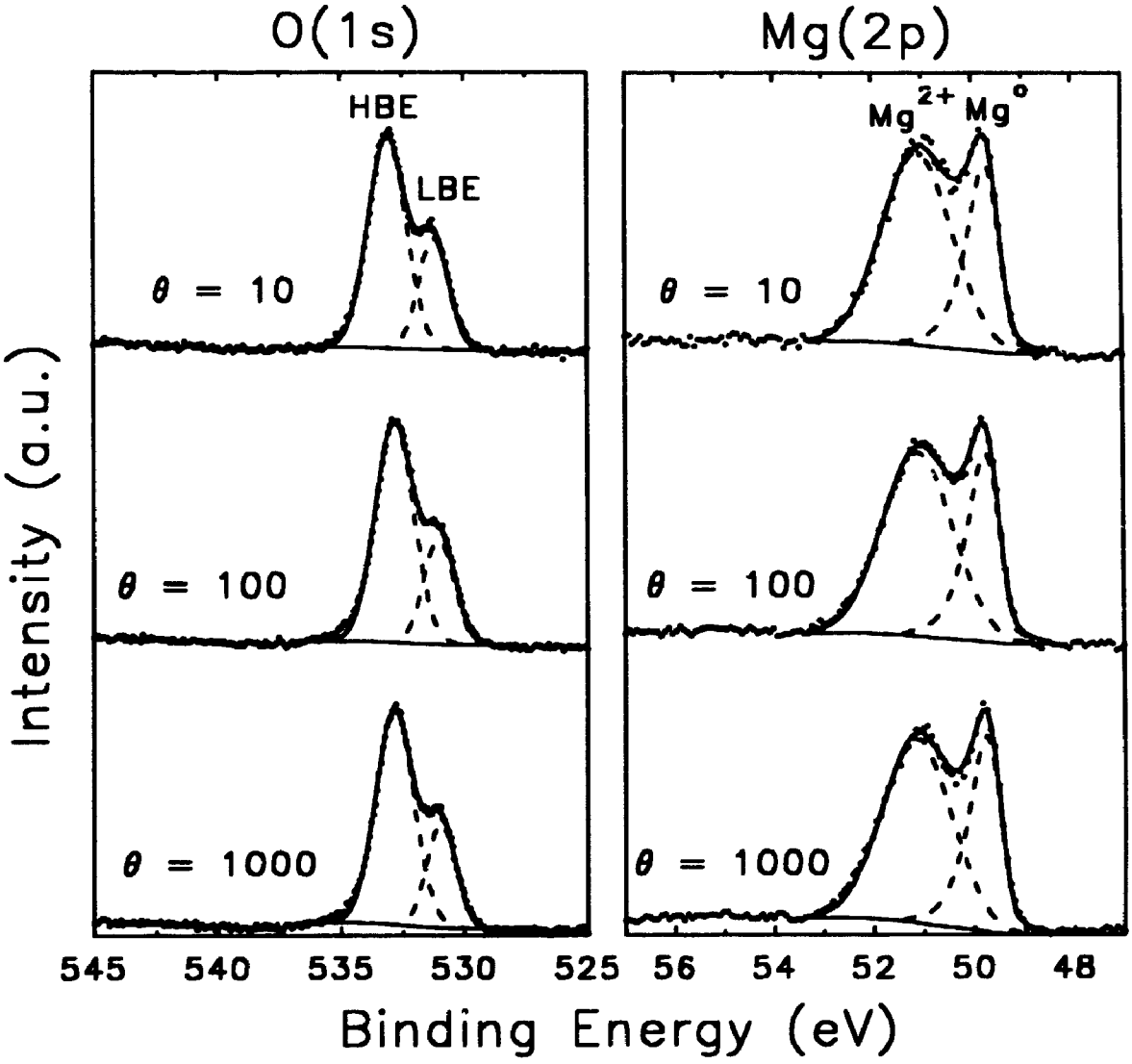

Figure 4.5: High-resolution O(1s) and Mg(2p) XPS spectra of the saturated oxide films formed on magnesium surfaces initially disordered by 3 keV Ar^+ ions at various total ion doses.

in enhanced oxide nucleation and oxygen penetration in the early stages of oxide growth, the limiting oxide thickness is not affected by the irradiation treatment.

4.3.2 Effect of Ion Energy

The effect of varying the ion bombardment energy from 1 to 5 keV at various total ion doses on the amount of surface oxygen detected by AES is shown in Figures 4.6(a), (b) and (c) for magnesium exposed to 0.3, 2.5 and 20 langmuir of D_2O, respectively. These exposure values were chosen for detailed study because they are representative of the three regimes of the oxidation process (dissociative adsorption, oxide nucleation and island growth, bulk thickening), as previously determined. From the figures it is evident that oxygen uptake on water-dosed magnesium surfaces is dependent upon the total ion energy and that the nature of this dependence is in turn dependent upon the total ion dose and the total water exposure that the surface receives. At low D_2O exposures (dissociative chemisorption regime), the concentration of surface oxygen increases with increasing ion bombardment energy for all values of total ion dose from $\theta = 10$ to $\theta = 1000$ ions/surface atom (0.3 L D_2O, Figure 4.6(a)). For the case of intermediate water exposures (oxide nucleation and growth, 2.5 L D_2O, Figure 4.6(b)), on the other hand, the character of the energy dependence changes with ion dose. At low doses ($\theta = 10$), the amount of detected surface oxygen is higher on the samples irradiated with lower energy ions. As the total ion dose increases above $\theta \approx$ 30 to 50, however, the situation is reversed, demonstrating increased surface oxygen

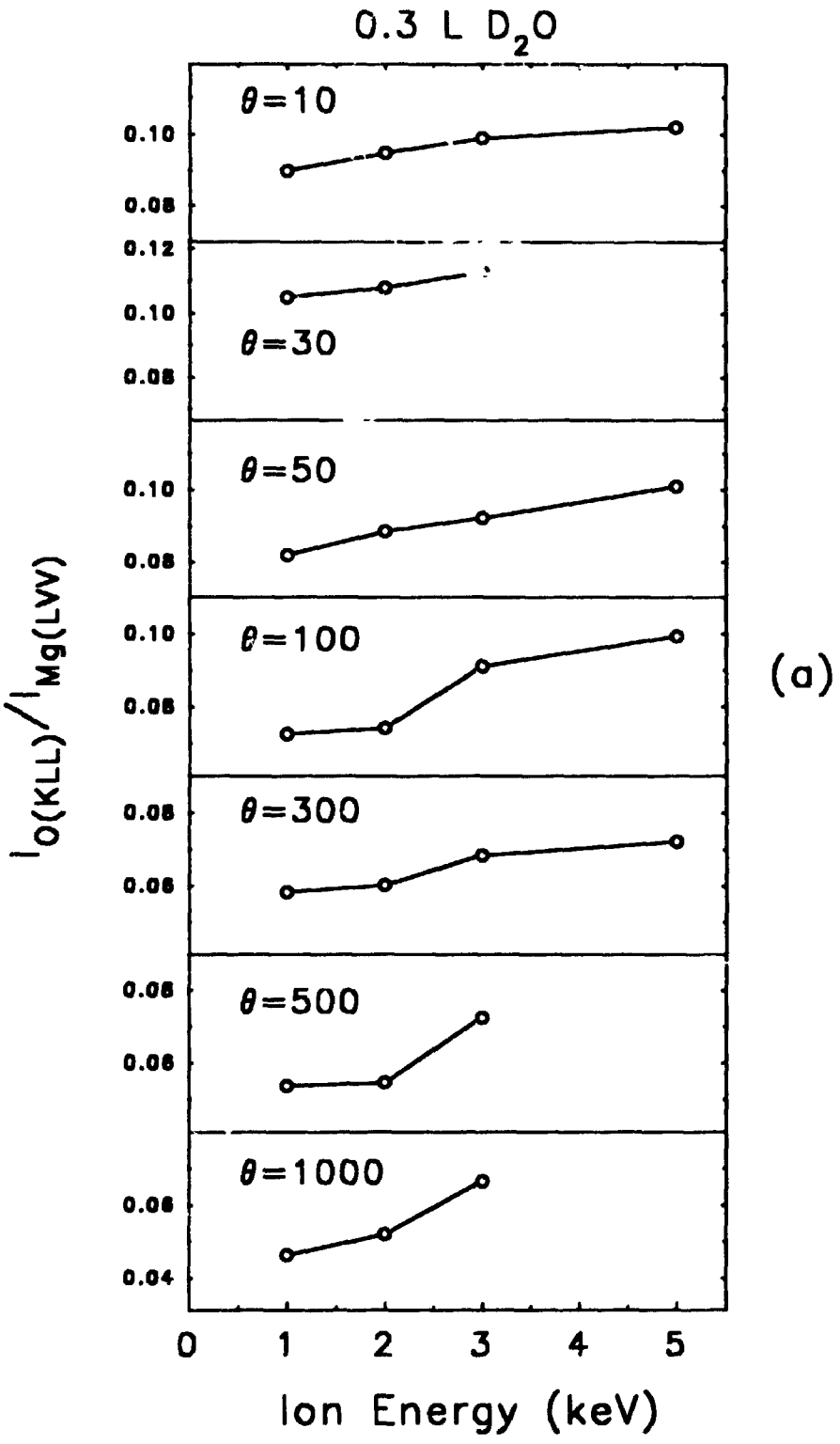

Figure 4.6: The effect of varying the ion bombardment energy from 1 to 5 keV at various total ion doses on the O(KLL)/Mg(LVV) AES ratio for magnesium exposed to (a) 0.3 L D_2O.

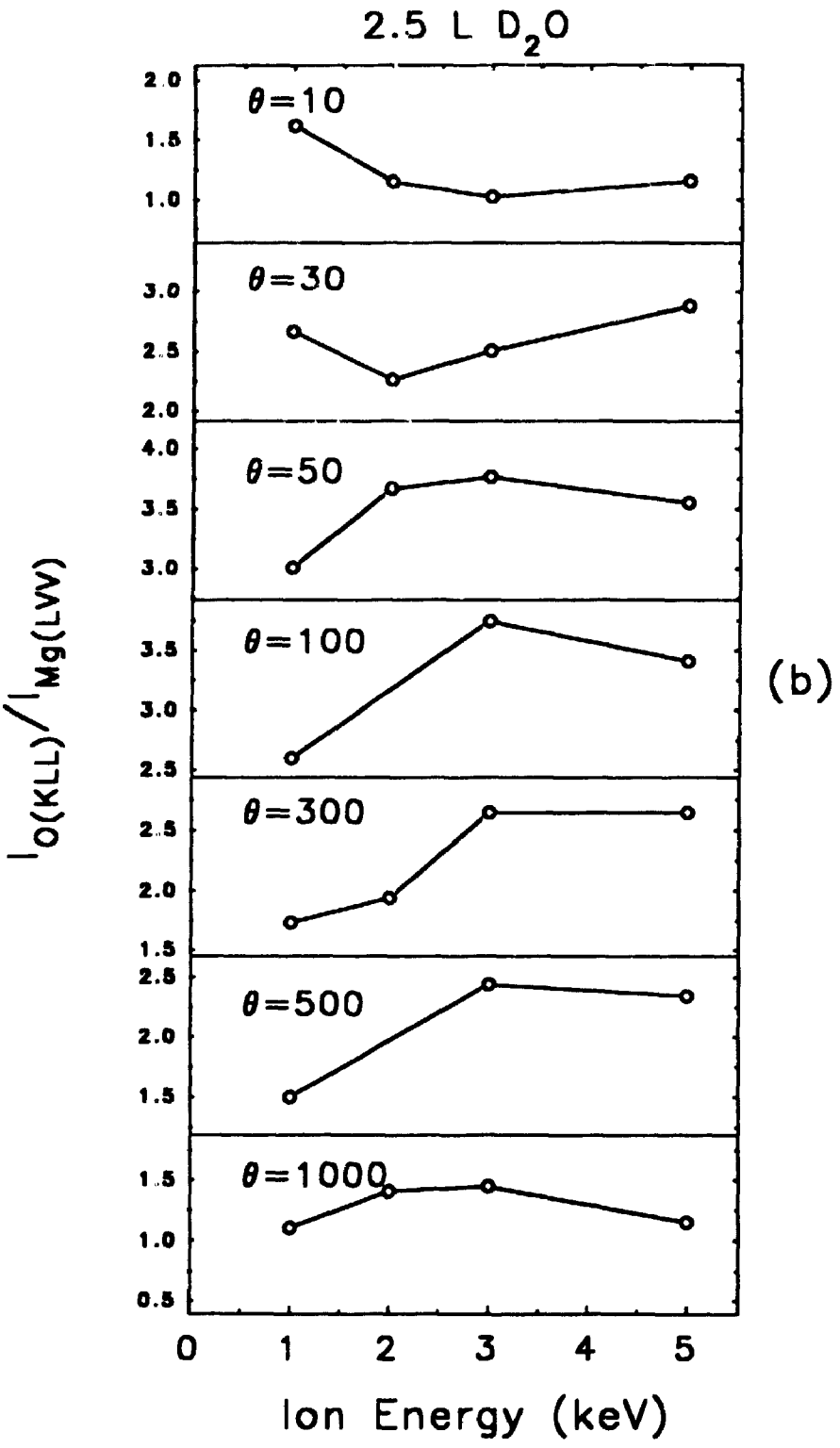

Figure 4.6: The effect of varying the ion bombardment energy from 1 to 5 keV at various total ion doses on the O(KLL)/Mg(LVV) AES ratio for magnesium exposed to (b) 2.5 L D_2O.

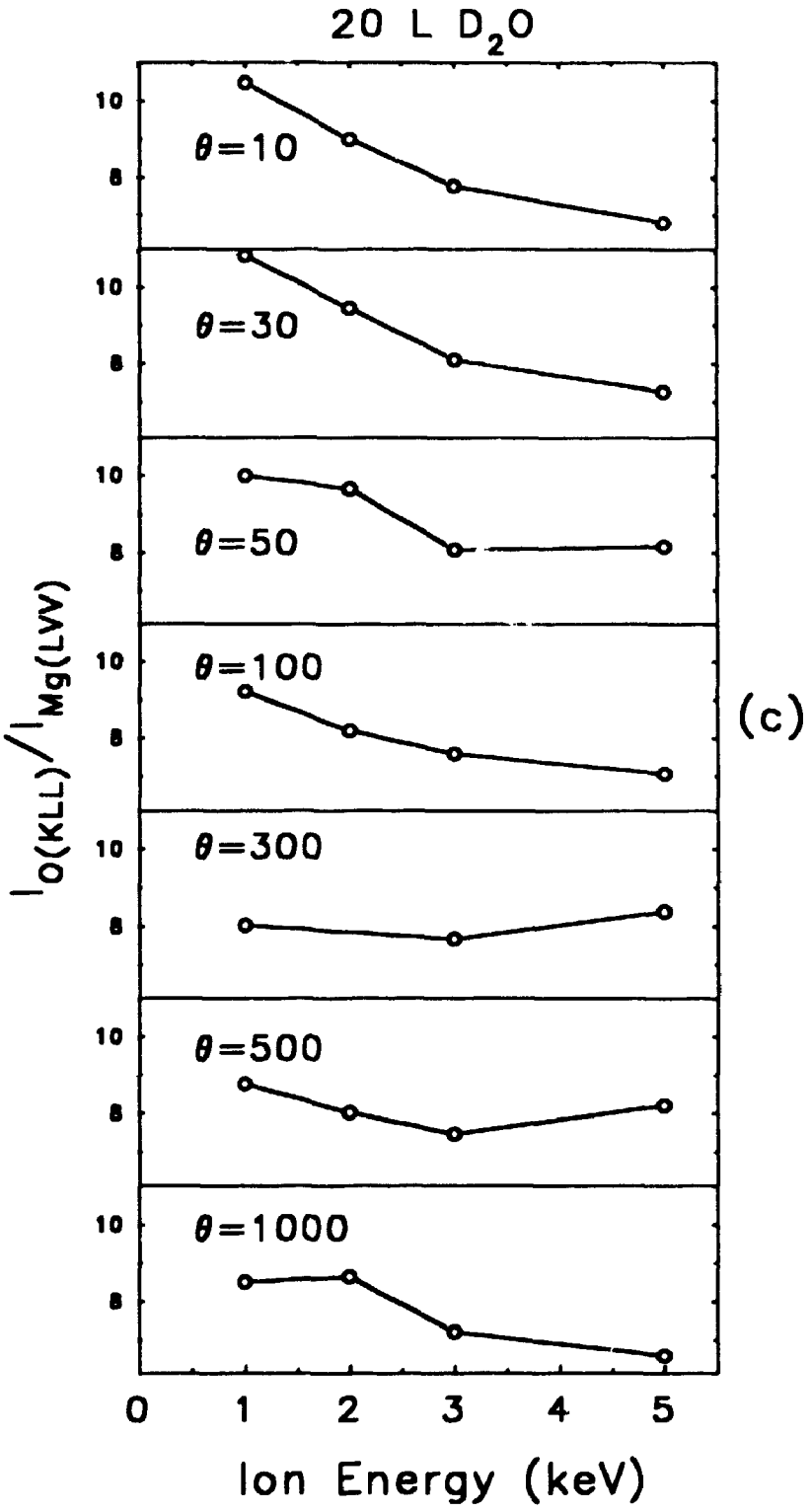

Figure 4.6: The effect of varying the ion bombardment energy from 1 to 5 keV at various total ion doses on the O(KLL)/Mg(LVV) AES ratio for magnesium exposed to (c) 20 L D_2O.

concentrations with increased bombardment energy (once again). Finally, for relatively high water exposures (bulk thickening, 20 L D_2O, Figure 4.6(c)), the O(KLL)/Mg(LVV) ratio decreases with increasing irradiation energy for the entire ion fluence range.

Information concerning the effect of ion energy on the relative number of oxygen atoms in the subsurface layers compared to the surface layers was obtained in a fashion identical to that above. Figure 4.7 shows the measured Mg(LVV)/Mg(KLL) AES intensity ratio for the thin oxide films formed by exposing magnesium surfaces to 20 L D_2O following bombardment with Ar^+ ions at energies ranging from 1 to 5 keV and total doses of θ = 10 , 100 and 1000 ions/surface atom. From Figure 4.7 it is evident that the effect of ion energy on the penetration of oxygen atoms into the magnesium lattice depends markedly on the total ion dose. For low irradiation doses (θ = 10), the number of oxygen atoms detected in the subsurface layers compared to the near-surface layers decreases with increasing bombardment energy. At elevated bombardment doses, on the other hand, increasing the ion bombardment energy form 1 to 5 keV results in an increased penetration of oxygen atoms into the bulk. This effect is clearly most pronounced at the highest fluence level, θ = 1000 ions/surface atom.

4.4 Discussion

In order to account for the data obtained, the structural state of the lattice following ion bombardment must be considered. It is well established that ion bombardment of metals produces replacement collision cascade sequences leading to

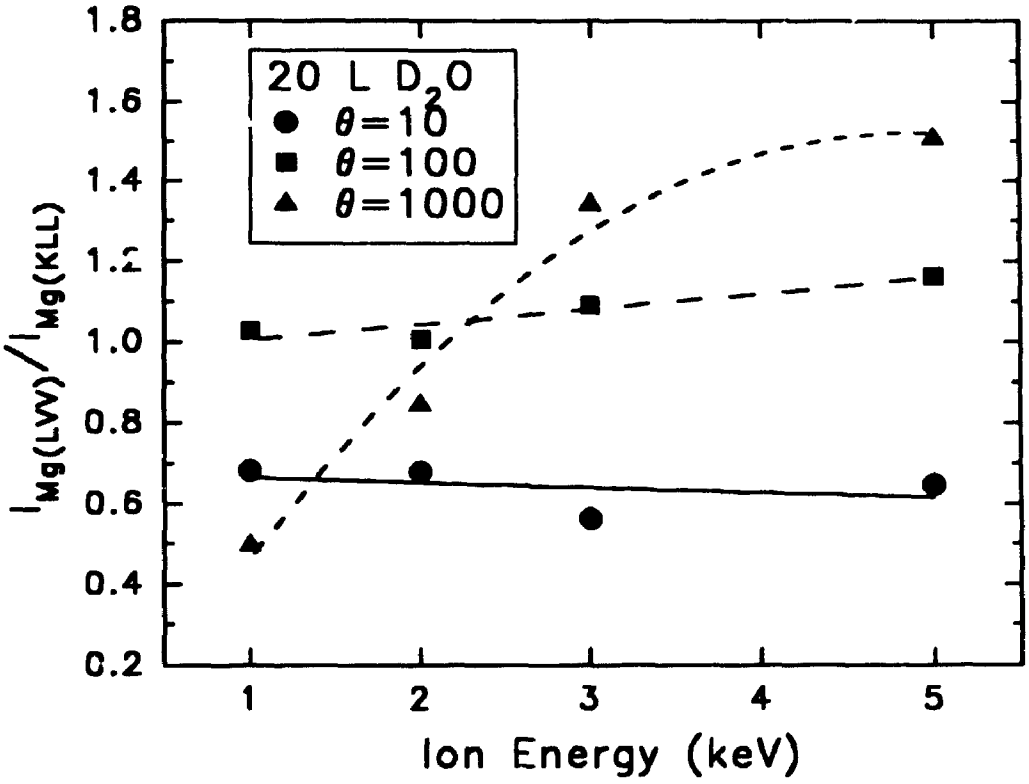

Figure 4.7: The evolution of the Mg(LVV)/Mg(KLL) AES ratio for increasing ion bombardment energy at various total ion doses. The sample was exposed to 20 L D_2O.

damage in the form of vacancies and implanted atoms in the surface layers of the crystal and self-interstitials at larger depths. Figure 4.8 shows the results of calculations of vacancy-type defect profiles and implanted argon atom profiles for magnesium surfaces bombarded with Ar^+ ions at energies ranging from 1 to 5 keV and incident ion beam angles of 45°. The calculations were performed using the Monte Carlo program TRIM (TRansport of Ions in Matter) [4.10]. (Inclusion of a thin ($\approx$1 nm) oxide layer on the surface in the simulations did not significantly alter the calculated profiles.) These simulations provide an estimate of the number of atoms initially displaced for each incoming ion, and consequently give an indication of the depth of damage introduced by the incident ion beam. It should be noted, however, that such calculations do not allow for channelling of ions down rows of atoms in the crystalline lattice and, as a result, the calculated damage depth is considered to be a lower limit. Nevertheless, Figure 4.8 should be useful as a rough guide to interpreting the effects of ion beam dose and energy on the interaction of water with magnesium surfaces. From the figure, it is apparent that the vacancy concentration is very high in the near-surface region and has a significant tail extending to deeper layers. The total number of vacancy-type defects and their mean distribution depth increases with increasing bombardment energy. The argon implantation profiles, on the other hand, are relatively broad, especially at higher incident ion energies. In addition, the number of implanted argon atoms in the near-surface region is smaller for the higher energy bombardment treatment due to the easier penetration of more energetic particles into the lattice.

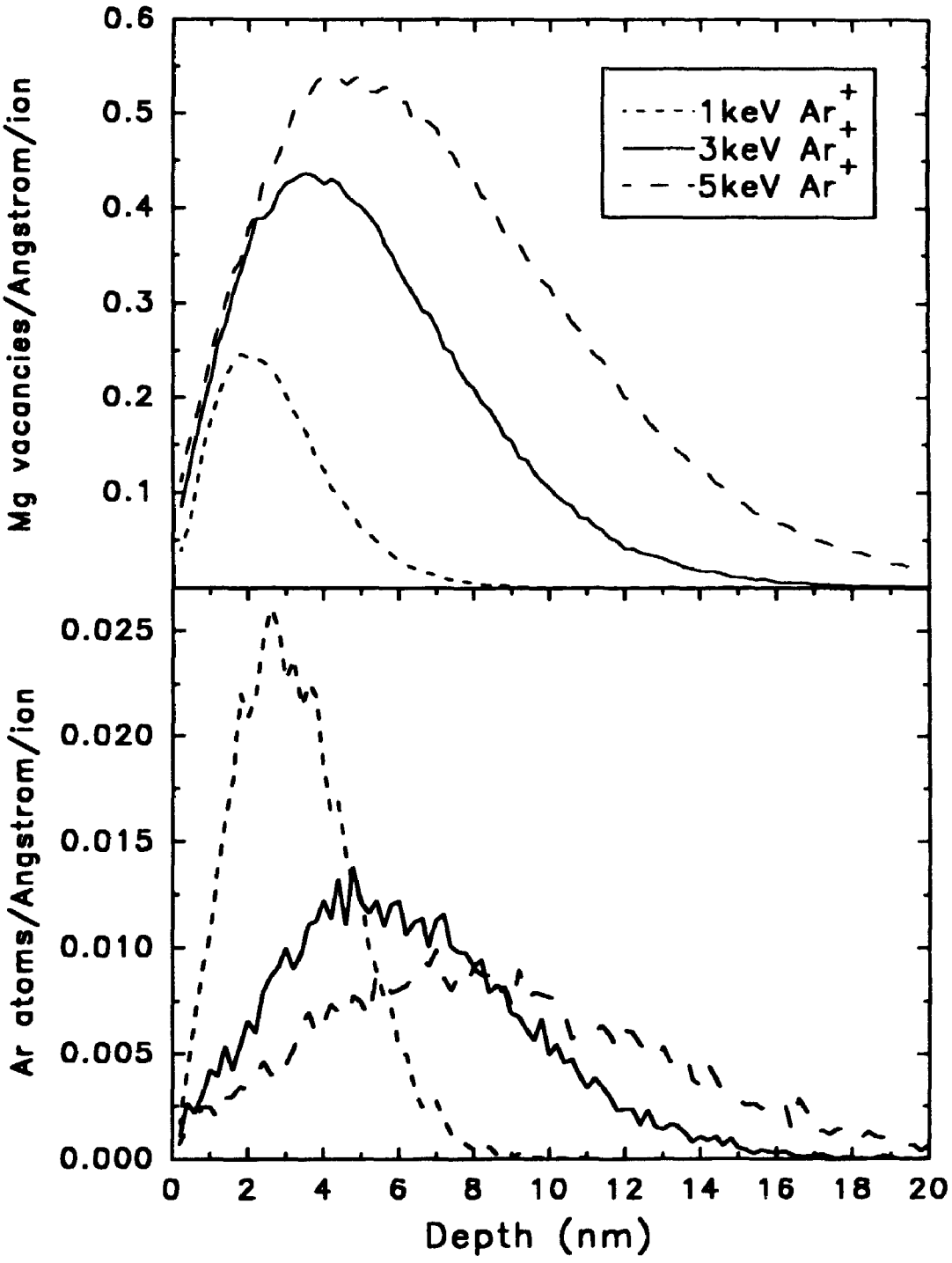

Figure 4.8: Calculations of vacancy-type defect profiles and implanted argon atom profiles for magnesium surfaces bombarded with Ar^+ ions at energies ranging from 1 to 5 keV. The calculations were performed using the Monte Carlo program TRIM [4.10].

It must also be noted, however, that calculations such as these do not allow for defect-defect interactions or defect clustering. These processes can significantly influence the final damage state of the surface, particularly at elevated temperatures and high total ion doses [4.2,4.3,4.11-4.13]. In general, the sequence of defect production as a function of ion dose can be summarised as follows [4.3]. First, at very low doses, only point defects (vacancies, interstitials) are formed both at the surface and in the bulk. Second, at somewhat higher doses, clusters of defects (vacancy clusters, vacancy-argon complexes and interstitial agglomerates) can form, possibly producing random steps and pits on the surface. Finally, at still higher doses, self-interstitials can cluster together, giving rise to dislocation half-loops extending through the entire damage depth (i.e. the range of displaced atoms in the collision cascade) and intersecting the surface. The actual dose ranges for these three generalized regimes will depend upon several variables including incident particle mass and energy and the substrate material. For example, Filiús et al [4.14] observed dislocation segments by TEM on molybdenum irradiated with 100 eV Ar^+ ions only at doses exceeding 1×10^{17} ions/cm^2 ($\theta > \approx 100$). Similarly, Rojo and Bru [4.15] used TEM to examine the damage structure resulting from Ar^+-irradiated Au, Ag and Cu at energies up to 5 keV and doses ranging from 1×10^{15} to 1×10^{17} ions/cm^2 ($\theta \approx 1$ to 100). Clearly resolvable dislocation loops were observed to form at doses greater than 1×10^{16} ions/cm^2.

Although the above TRIM simulations do not allow for detect clustering at elevated ion doses, such information can be obtained, at least qualitatively, by examining the quality of the Electron Back Scattering Diffraction Patterns (EBSDP's). Figure 4.9

shows the EBSP's obtained from magnesium surfaces initially damaged by total Ar^+ ion doses of (A) $\theta = 10$, (B) $\theta = 100$ and (C) $\theta = 1000$ ions/surface atom at 3 keV. From the figure it is evident that increasing doses of Ar^+ ions lead to increased degradation of the quality of the diffraction patterns by slight broadening and blurring of the Kikuchi lines. This increased "diffuseness" of the pattern has been attributed to local bending and dilatation of the lattice planes caused by an increased dislocation density at the surface [4.16,4.17]. This lattice bending results in electrons being scattered away from the Bragg condition and results in reduced sharpness of the diffraction band edges of the EBSDP's. It is very likely, therefore, that at elevated ion doses ($\theta \geq 100$) there is increased lattice strain due to dislocation segments arising from the clustering of point defects introduced by the ion bombardment treatment, as predicted above. The use of pattern degradation of Electron Channelling Patterns (ECP's) to quantify near-surface dislocation density is well established [4.18-4.20]. For EBSDP's, however, it is not trivial to define a simple correlation between pattern diffuseness and lattice strain [4.21]. Nevertheless, recent efforts have been made towards the quantification of EBSD pattern diffuseness using digital image analysis and discrete Fourier methods [4.16] and, although they are not performed here, it is possible that such analyses could be used to quantify the amount of surface damage introduced by fast particle bombardment of a metal surface.

With the above processes in mind, it should now be possible to explain the observed behaviour of oxygen uptake on damaged magnesium surfaces by assuming that competition exists between the effects of radiation damage (vacancies, vacancy clusters,

Figure 4.9: Electron Back Scattering Diffraction Patterns (EBSDP's) obtained from magnesium surfaces initially bombarded with total 3 keV Ar^+ ion doses of (A) $\theta = 10$, (B) $\theta = 100$ and (C) $\theta = 1000$ ions/surface atom. Increasing "diffuseness" of the patterns at elevated ion doses is attributed to increased lattice strain due to an increased near-surface dislocation density.

dislocation emergence points) and implantation of argon atoms on the processes of adsorption, nucleation and growth of oxide. This is discussed below.

The most obvious property of surface point defects such as vacancies and adatoms is that they produce coordinatively unsaturated surface atoms, thus leading to high coordination sites for adsorbates [4.2]. Consequently, at sites above a vacancy, for example, the interaction energy is stronger (i.e. the total energy is lower) because the number of nearest neighbour atoms is increased, or similarly, the distance to nearest neighbours is decreased. The result is that surface point defect sites can increase the sticking coefficient of adsorbates, or reduce the activation energy for dissociative adsorption. Such an effect has been observed, for example, by Miranda, Rojo and Salmeron [4.22] for the chemisorption of O_2 on ion-disordered Pt(111) surfaces. A similar, though less drastic, effect was observed here. As the total ion dose was increased from $\theta = 10$ to $\theta \approx 30$ to 50 there was a small increase in the amount of chemisorbed oxygen detected on the magnesium surfaces (0.3 L D_2O, Figure 4.2). This may be explained by the increased number of adsorption sites of high sticking probability introduced by the radiation-induced defects.

The fact that the amount of chemisorbed oxygen decreased as the ion dose was increased beyond $\theta \approx 30$ to 50 may at first seem unusual. The TRIM simulations (Figure 4.8) indicate that the rate of production of vacancy-type defects is more than an order of magnitude greater than the rate of accumulation of implanted argon. Even if as many as 80% of the vacancies dynamically recombine with self-interstitial atoms, as has been suggested [4.13], the concentration of near-surface vacancies is still expected

to be more than five times that of implanted atoms. In addition, it is expected that the radiation damage will become saturated as a result of the continuous receding of the surface due to sputtering. The ion doses required for saturation will then be of the order of the depth of damaged layers. For example, for magnesium bombarded with 3 keV Ar^+ ions, the depth of damage is approximately 15 nm (Figure 4.8). Assuming that 1 ML Mg $\approx$ 0.26 nm (i.e. one half the lattice parameter, c/2), then 15 nm corresponds to approximately 50 magnesium layers. So, assuming a sputtering yield of unity, the saturation dose of 3 keV Ar^+ ions in Mg is expected to be $\theta \approx 50$. These processes then suggest that the effect of defects should dominate over the effect of implant accumulation, even at elevated ion doses. However, studies of Ar^+ irradiated Mo and Si [4.14] have shown that, at moderate ion fluences, a quasi-saturation of the number of trapped Ar atoms does indeed exist due to sputter-induced saturation fluences. However, at higher ion doses, where self-interstitials were observed to cluster together to form dislocation loops, there was a renewed increase in Ar atom trapping. A similar increase in Ar trapping after excessive ion fluences ($\geq 1 \times 10^{16}$ ions/cm^2) has been observed by Edwards [4.23] for nickel surfaces. It appears, therefore, that the dislocation segments formed at high ion doses may in fact grow and become stabilised by virtue of the mutual interaction between the Ar atoms implanted at a shallow depth and the self-interstitials. It is likely, therefore, that a similar situation exists for Ar^+ irradiated magnesium. At ion doses exceeding saturation ($\theta > \approx 50$, see above), there may be increased Ar trapping associated with the gradual formation of dislocation segments intersecting the surface.

The possibility that the reduced surface oxygen concentration at elevated ion doses may in fact be an artifact caused by diffusion of adsorbed oxygen into the lattice beyond the detection depth of the Auger probe is unlikely. Figure 4.4 clearly shows that, for a 0.3 L D_2O exposure, the relative number of oxygen atoms in deeper layers compared to at the surface remains unchanged with increasing ion fluence. The small decrease in the observed amount of chemisorbed oxygen at elevated ion doses (0.3 L, Figure 4.2) can best be explained by an increased blocking action of the implanted argon atoms at these fluences. Such an effect has been observed previously by Chenakin [4.24] for O_2 chemisorption on polycrystalline copper at relatively high ion doses. The author considered this blocking action as being equivalent to a reduction in chemisorption energy on atoms *nearest* to a defect. Finally, it must be emphasized that the effect of ion dose on the chemisorption stage of the interaction of water vapour with magnesium was very minor (0.3L, Figure 4.2). This is likely due to the fact that the dissociative chemisorption of water on magnesium is very rapid and likely non-activated [Chapter 3]. As such, the effect of radiation-induced defects on the chemisorption regime for magnesium is not expected to be extreme.

Similar arguments can be invoked to explain the effect of ion energy on oxygen uptake in the chemisorption regime (Figure 4.6(a)). It was shown in Figure 4.6(a) that the concentration of surface oxygen detected following a 0.3 L D_2O exposure increased with increasing initial ion bombardment energy, for all values of total ion dose. Similar observations have been made for O_2 chemisorption on copper surfaces bombarded with Ar^+ ions from 1 to 8 keV [4.25]. At low doses ($\theta < 50$) then, the increasing surface

oxygen concentration with ion energy can be attributed to the greater number of near-surface vacancy-type defects created by the more energetic bombardment (Figure 4.8). At intermediate to high ion fluences, where the effect of implanted argon is expected to dominate, the same effect of energy was observed. At low energies there is a larger concentration of Ar atoms in the near-surface region created by the irradiation treatment (Figure 4.8). As the bombardment energy increases, the argon distribution profile moves deeper into the specimen. Consequently, the passivation or blocking effect of the argon atoms is reduced, leading to increased amounts of chemisorbed oxygen at higher energies.

The present results suggest that the effect of ion bombardment on the initial interaction of water with magnesium surfaces is most pronounced in the oxide nucleation and growth stage of the oxidation process. Similar results have been obtained for the case of O_2 interactions with nickel surfaces, where both experiments [4.22,4.26] and theory [4.27] have suggested that defects play a major role in the nucleation process. In addition, early studies by Cohen [4.28] and Orr [4.29] on clean magnesium films concluded that nucleation of surface oxide occurred at preferred (defect) sites.

In order to understand the effects of surface defects and implanted atoms on the processes of nucleation and growth of oxide, the actual mechanisms of these processes must be considered. It has been postulated [4.30] that the nucleation and growth of oxide islands on a metal surface proceeds via a "place exchange" mechanism, whereby oxide grows by a series of activated interchanges between cations and anions at the surface. The driving force for place exchange is an "image force" that arises from the transfer of

charge via electron tunnelling to the oxygen atoms adsorbed on the surface. It is likely that the presence of atomic-scale defects on the surface, which are sites of high chemical potential, will reduce the activation energy for exchange and consequently act as preferred sites for oxide nucleation. In terms of the present results, it appears that as the Ar^+ ion bombardment dose is increased in the low dose regime (θ = 10 to $\theta \approx$ 50 to 100) oxide nucleation is facilitated by the increased number of near-surface defect sites acting to reduce the activation energy for place exchange. This then results in accelerated oxygen uptake in the oxide nucleation and growth stage on disordered surfaces (1.2 L, 2.5 L, Figure 4.2).

It is noteworthy that a similar behaviour was observed in Chapter 3 for the uptake of oxygen on different grain faces of pure magnesium exposed to water vapour. Modelling results suggested that the rate of oxygen uptake was faster on grain faces having higher-index orientations, as compared to the near-basal grains, particularly in the oxide nucleation and island growth stage. It is possible, therefore, that the local environment of atoms on a heavily disordered Mg(0001) surface may be similar to that of an undamaged, higher-index surface.

As the total 3 keV Ar^+ ion dose was increased beyond $\theta \approx$ 50 to 100 (i.e. beyond saturation), the total amount of oxygen detected on the surface for exposures corresponding to the nucleation and growth stage of the oxidation process was found to decrease markedly (Figure 4.2). This can be attributed to the increased argon trapping associated with the formation of dislocation structures at these elevated ion fluences. If the oxide island growth process is again envisaged as an advancing wave of place-

exchanging ions, then the rate of island growth is determined by the rate of place exchange. Since all available oxygen atoms are expected to readily acquire electrons (i.e. electron tunnelling is assumed to be very fast), the rate will depend on the number of cation sites available on the surface for place exchange. According to Fehlner and Mott [4.30], the rate of island growth is given by:

$$\frac{dx}{dt} = \Omega K N_s \nu P \qquad (4.1)$$

where x is the oxide thickness at time t; Ω is the oxide volume per oxygen ion; K is a constant related to the equilibrium between adsorbed and gas-phase molecules at pressure P; N_s is the number of available cation sites; and υ is the critical vibrational frequency for the exchange event. At constant pressure and temperature, υ is expected to remain unchanged for surfaces of varying degrees of disorder. In addition, since it was shown earlier that the effect of ion bombardment on the chemisorption regime on Mg was small, K can be regarded as essentially constant. Therefore, it is likely that the presence of excess Ar atoms in the surface layers serves to limit N_s, the number of cation sites available for place exchange. The implanted atoms thus appear to block nucleation sites or interfere with the kinetics of oxide island ordering and hence the rate of oxide nucleation and growth is diminished at excessive Ar^+ ion doses.

The effect of ion energy on the kinetics of oxygen uptake in the oxide nucleation and island growth regime was shown in Figure 4.6(b). The total amount of oxygen

detected on the surface was found to actually decrease with increasing ion energy at low total ion dose (θ = 10). This behaviour was unexpected because, at this fluence level, vacancy-type defects are expected to dominate the damage state of the lattice and increasing bombardment energy should lead to increased near-surface vacancy concentrations (Figure 4.9). It is possible, however, that at these low total ion doses, the lower energy bombardment treatment results in a higher density of dislocations intersecting the surface. Evidence supporting this contention is contained in Figure 4.7, where an enhanced penetration of oxygen into the magnesium lattice was observed at lower energies for a total ion dose of θ = 10 ions/surface atom. The depth of damage is significantly shorter for the lower energy bombardment treatment (Figure 4.8) and, as a result, saturation of damage should occur more readily at lower energies for a given low total ion dose level. This would presumably facilitate the formation of dislocation structures at lower energies. The dislocation emergence points would then provide numerous low activation energy sites for place exchange, resulting in faster oxide island growth. As the total ion dose increases, however, the build-up of retained Ar is expected to become significant. For these higher dose irradiation treatments, therefore, the increased numbers of near-surface Ar atoms for the less energetic bombardment would serve to limit oxide nucleation and growth, as discussed above.

The effect of Ar^+ ion bombardment on the bulk oxide thickening stage of the oxidation process of magnesium also warrants discussion. It was shown in Chapter 3 that the bulk thickening process is controlled by the transport of metal cations from the metal/oxide interface to the oxide/gas interface. Such a mechanism is then expected to

produce a counterflow of vacancies into the metal, as cations are incorporated into the growing oxide film. It is therefore expected that the presence of dislocation emergence points on the surface, which could act as sinks for the vacancies created by cation incorporation, would cause an increase in the rate of bulk oxide growth. With this in mind, it seems surprising that increased 3 keV Ar^+ ion doses resulted in a slow *decrease* in the amount of surface oxygen detected for water exposures in the bulk thickening regime (5L, 20L, Figure 4.2). The possibility that the shallowly implanted argon atoms may in some way act to limit vacancy injection or cation incorporation seems unlikely, particularly in view of the ion energy effect data of Figure 4.6(c). If this were indeed the case, then the lower energy bombardment, which results in a higher near-surface argon distribution (Figure 4.8), should have resulted in lower total detected oxygen concentrations as compared to the higher energy bombardment, which results in a much lower near-surface argon concentration. A more plausible explanation for the decreasing AES intensities observed for elevated ion doses, therefore, is that some of the oxygen atoms may in fact penetrate beyond the detection depth of the technique. Figures 4.3, 4.4 and 4.7 clearly show that more oxygen signal originates from within deeper layers for the heavily damaged surfaces. This results in a "wider" metal/oxide interface and suggests that the penetration of oxygen atoms into the magnesium lattice is facilitated by the high dose irradiation treatment.

The actual depth of oxygen penetration at elevated ion doses can be estimated by considering the escape depths of the various Auger electrons (Appendix A). It is expected that 95% of the Mg(LVV) AES signal will originate from within

$3(\lambda_{Mg(LVV)}) \approx 1.0$ nm from the surface and that, similarly, 95% of the O(KLL) signal will originate from within $3(\lambda_{O(KLL)}) \approx 2.5$ nm from the surface. The fact that a measurable Mg(LVV) signal remains after 20 L exposure implies that the oxide film must necessarily be less than 1.0 nm thick. In order for the O(KLL)/Mg(LVV) AES ratio to decrease at elevated ion doses (Figure 4.2) while more oxygen is detected in deeper layers (Figure 4.3,4.4), it is apparent that some oxygen atoms must penetrate at least 2.5 nm into the surface. In addition, these penetrating oxygen atoms will cause some of the substrate Mg atoms to become oxidised, thereby reducing the intensity of the metallic Mg(LVV) and Mg(KLL) signals. The fact that the ratio Mg(LVV)/Mg(KLL) increases with increasing ion dose (Figure 4.4) suggests that the metallic Mg(KLL) signal is attenuated to a larger extent than is the metallic Mg(LVV) signal. This, combined with the fact that a measurable Mg(LVV) signal is still present even at the highest ion doses, suggests that the penetration of oxygen atoms into the Mg lattice is very likely a localized phenomenon. Diffusion likely occurs along dislocation paths originating from the high fluence bombardment, since the activation energy for ion movement would be less along such paths.

It is interesting to note that the penetration of oxygen into the substrate at elevated ion doses was not observed by XPS at higher coverages (Figure 4.5). The Mg(KLL) Auger electrons and the Mg(2p) photoelectrons have comparable escape depths (Appendix A) and consequently should both be equally capable of detecting penetrating oxygen atoms. The apparent discrepancy can, however, be explained by the different total oxide thicknesses present on the surface for the two experiments. The AES results (Figures

4.3,4.4 and 4.7) are for a 20 L exposure - relatively early in the bulk thickening regime. The film thickness in this case is less than 1.0 nm (see above). The XPS results (Figure 4.5), on the other hand, refer to the saturated oxide films formed by a long exposure. The thickness of these films is approximately 2.3 nm. Any oxygen atoms penetrating below the oxide film in the XPS experiments would then be proportionately more difficult to detect because of the relatively large oxidised Mg signal already present due to the much thicker film. Nevertheless, the fact that no *significant* change in the relative oxidised/metallic Mg XPS contributions was observed suggests that the oxygen atoms do not penetrate much deeper than approximately 2.5 to 3.0 nm into the surface.

The fact that the degree of initial disorder of the magnesium surface did not affect the limiting oxide thickness (Figure 4.5) may also seem surprising in view of the bulk oxide thickening mechanism of magnesium. A possible consequence of the increased number of nucleation sites for damaged surfaces is a reduced oxide grain size [4.31]. This would then be expected to provide a greater number of fast diffusion pathways (i.e. grain boundaries) for the outward-moving cations, thus again leading to an increased rate of oxide growth. These apparent difficulties can, however, be accounted for by considering the structural state of the oxide film itself. It was suggested in Chapter 3 that the oxide film formed on magnesium by reaction with water vapour is very likely non-crystalline, exhibiting little long-range order. It was further suggested that it is the presence of a small amount of hydrogen in the film that leads to this increased tendency towards non-crystallinity by providing structural flexibility in the form of metal-hydrogen and metal-hydroxyl bonds in addition to the normal metal-oxide bonds. These

conclusions were reached in part by carefully examining the shape of the core-level O(1s) XPS line. Detailed XPS spectra showed the presence of two distinct types of oxygen and it was concluded that the high binding energy (HBE) O(1s) component is due, at least in part, to oxygen atoms in a "defective" environment within the disordered oxide. (The LBE component is due to oxygen atoms in a normal MgO chemical environment). These conclusions are further supported by the present results. Figure 4.5 also shows the O(1s) XPS line of the saturated oxide films for different total 3 keV Ar^+ ion doses. From the figure, it is clear that the ratio of the HBE/LBE O(1s) XPS components remains constant for increasing total ion doses. This suggests that an increasing degree of surface disorder in the magnesium substrate does not lead to an increasing degree of disorder in the oxide film. The influence of the ion-induced defects thus appears to be confined to the first layers of the growing oxide.

4.5 Conclusions

The interaction of water vapour with ion-damaged magnesium surfaces has been systematically studied by AES. It has been established that the kinetics of water interaction with irradiated surfaces depends markedly on the total ion dose (θ = 10 to 2000 ions/surface atom) and ion energy (1 to 5 keV) that the surface receives and that the character of this interaction changes with the level of water exposure. The effect of ion bombardment was clearly most pronounced in the oxide nucleation and island growth stage of the oxidation process. The dissociative chemisorption and final bulk thickening regimes were only weakly affected by prior radiation treatment. The results have been interpreted based on the assumption of competition between the effects of radiation-induced defects (vacancies, vacancy-clusters, dislocation loops) and implanted argon atoms on the oxidation process.

Increasing numbers of near-surface vacancy-type defects caused a small increase in the amount of detected surface oxygen during the chemisorption regime. This has been explained by the increased number of adsorption sites of high sticking probability introduced by the radiation-induced defects. Vacancy-type defects also caused a significant increase in the amount of detected surface oxygen during the oxide nucleation and growth stage, by providing sites with reduced activation energy for place exchange. At elevated total ion fluences (above saturation), lattice strain due to the presence of an increased near-surface dislocation density was evident. A renewed increase in Ar atom retention associated with the dislocation formation was assumed to occur in order to

account for the observed decrease in oxygen adsorption and oxide nucleation and growth at high ion doses. The effect of implanted Ar atoms was to block adsorption and nucleation sites and to interfere with oxide island ordering. At relatively high water exposures (bulk thickening), there was enhanced penetration of oxygen atoms into the magnesium lattice at high total ion doses. This penetration was assumed to occur preferentially along dislocation emergence points originating from the high dose bombardment. No such enhanced penetration of oxygen was observed for shorter water exposures. The limiting thickness of the oxide layer (11 ML, 2.3 nm) was not found to be affected by prior ion bombardment. The influence of the ion-induced defects thus appeared to be confined to the first layers of growing oxide.

References

[4.1] G.A. Somorjai, Chemistry in Two Dimensions - Surfaces, (Cornell University Press, Ithaca, 1981).

[4.2] K. Wandelt, Surf. Sci. 251/252 (1991) 387.

[4.3] R. Miranda and J.M. Rojo, Vacuum 34 (1984) 1069.

[4.4] P.A. Thiel and T.E. Madey, Surf. Sci. Rep. 7 (1987) 211.

[4.5] L. Gonzalez, R. Miranda and S. Ferrer, Solid State Commun. 44 (1982) 1461.

[4.6] D.R. Baer and M.T. Thomas, Appl. Surf. Sci. 26 (1986) 150.

[4.7] T.W. Weir, Reaction of Water and Hydrogen Sulphide with Single Crystal Iron (001), Ph.D. Thesis, Lehigh University (1984).

[4.8] H. Namba, J. Darville and J.M Gilles, Surf. Sci. 108 (1981) 446.

[4.9] S. Tanuma, C.J. Powell and D.R. Penn, Surf. Interface Anal. 17 (1991) 911.

[4.10] Z.F. Ziegler, J.P. Biersack and U. Littmark, The Stopping and Range of Ions in Solids (Permagon Press, New York, 1985).

[4.11] D.G. Armour and A.H. Al-Bayati, Nucl. Inst. Meth. Phys. Res. B67 (1992) 279.

[4.12] R.S. Nelson and D.J. Mazey, Rad. Eff. 18 (1973) 127.

[4.13] J. Mäkinen, A. Vehanen, P. Hautojärvi, H. Huomo, J. Lahtinen, R.M. Nieminen and S. Valkealahti, Surf. Sci. 175 (1986) 385.

[4.14] H.A. Filius, A. Van Veen, K.R. Bijkerk and J.H. Evans, Rad. Eff. Def. Sol. 108 (1989) 1.

[4.15] J.M. Rojo and L. Bru, Phil. Mag. 25 (1972) 1409.

[4.16] A.J. Wilkinson, Mater. Sci. Eng. A135 (1991) 189.

[4.17] P.N. Quested, P.J. Henderson and M. McLean, Acta Metall. 36 (1988) 2743.

[4.18] D.L. Davidson, Int. Met. Rev. 29 (1984) 75.

[4.19] R. Stickler and G.R. Booker, Electron Microscopy and Structure of Materials (University of California, Berkeley, 1972) 301.

[4.20] G. Palumbo and K.T. Aust, Microstructural Sci. 17 (1989) 275.

[4.21] V. Randle, Microtexture Determination and its Applications (Institute of Materials, London, 1992).

[4.22] R. Miranda, J.M. Rojo and M. Salmeron, J. Vac. Sci. Technol. 18 (1981) 596.

[4.23] D. Edwards Jr., J. Appl. Phys. 46 (1975) 1437.

[4.24] S.P. Chenakin, Vacuum 36 (1986) 635.

[4.25] S.P. Chenakin, V.T. Cherepin and A.B. Goncharenko, Phys. Met. 3 (1981) 495.

[4.26] D.F. Mitchell, P.B. Sewell and M. Cohen, Surf. Sci. 61 (1976) 355.

[4.27] J.M. Gallagher and R. Haydock, Surf. Sci. 83 (1979) 117.

[4.28] M.S. Cohen, Acta Metall. 8 (1960) 356.

[4.29] W.H. Orr, Thesis, Cornell University No. 62-5965 (Ann Arbour, 1962).

[4.30] F.P. Fehlner and N.F. Mott, Oxid. Met. 2 (1970) 59.

[4.31] G. Dearnley, in J.K. Hirvonen (ed.), Treatise on Materials Science, Vol. 18 - Ion Implantation (Academic Press, New York, 1980).

CHAPTER 5

THE INITIAL INTERACTION OF WATER VAPOUR WITH Mg-Al ALLOY SURFACES

5.1. Introduction

The initial adsorption and reaction of water vapour with metal surfaces is of fundamental interest from both a theoretical and practical point of view [5.1]. In particular, an understanding of the initial stages of oxide formation on alloy surfaces, up to and including the formation of a steady-state film, is critical to designing for oxidation/corrosion resistance [5.2,5.3]. In this chapter, the initial oxide formation occurring on Mg-Al alloy surfaces exposed to low partial pressures of water vapour at room temperature has been studied in detail using Auger electron spectroscopy (AES) and X-ray photoelectron spectroscopy (XPS).

The low density and high specific stiffness of magnesium-based alloys make them extremely attractive candidates for engineering applications where light weight is important (eg. aerospace industries, automotive industries). However, despite their competitive mechanical properties, the use of magnesium alloys is not fully realised, largely due to a perceived lack of corrosion resistance. The addition of aluminum is a long-known and well-documented means of improving the corrosion resistance of Mg alloys [5.4,5.5], however, the mechanisms and limits of this improvement are poorly understood. The present study was undertaken, therefore, with the intention of

understanding more clearly the mechanisms of protective oxide formation on Mg-Al alloy surfaces. The results are, moreover, of more general theoretical interest since both Mg and Al are simple metals and their behaviour can be approached by simple models.

The interaction of oxygen with Mg-Al alloy surfaces has been examined by several other groups [5.6-5.11]. For example, Leontis and Rhines [5.6] observed linear growth of oxide on polycrystalline Mg and Mg-Al alloys (1.8wt% Al to 9.1wt% Al) in the temperature range of 773 K to 848 K. The activation energy for the oxidation process was found to increase with aluminum content. Similarly, Schwoebel [5.7] studied oxide growth on Mg single crystals in pure O_2 at 673 K using a quartz microbalance and found that the addition of 0.96 at% Al resulted in a small decrease in the parabolic growth rate. Under these experimental conditions, however, the very early stages of oxide formation up to a few monolayers of oxide could not be characterised. Hayden et al. [5.8,5.9], on the other hand, used AES, XPS, volumetric absorption and diode surface potential measurements to study the room temperature oxidation of Mg containing from 1 to 6 wt% Al. These authors observed an increase in the rate of the early stages of oxidation with increased Al contents and noted that both Mg and Al atoms were oxidised. It was also found that oxide nucleation was facilitated on Mg-Al surfaces compared to pure magnesium surfaces. The later stages of oxide film growth (bulk thickening) were not examined.

To the best of our knowledge, there have been no fundamental investigations of the interaction of water vapour with Mg-Al alloy surfaces. The interaction of water vapour with pure magnesium surfaces was examined in detail in Chapter 3. In the

present work, a similar three-stage oxidation behaviour was found to be operative on Mg-Al alloy surfaces. Modelling of AES data suggested that the rate of oxide nucleation was enhanced on Mg-Al surfaces relative to pure Mg surfaces. In addition, the growth of oxide islands appeared to occur preferentially above magnesium-rich regions on the surface. At longer exposures, XPS indicated that Al^{3+} cations were incorporated into the growing oxide film, resulting in an increased activation energy for ion movement and a pronounced decrease in the rate of bulk oxide thickening.

5.2. Experimental

Two polycrystalline magnesium alloys were used throughout the study: Mg-3.0wt%Al and Mg-8.5wt%Al. Table 5.1 shows the major impurities present in the specimens determined by spark source mass spectrometry. The alloys were solution heat-treated to a T4 condition (24 h, 693K) and quenched in water in order to homogenise their microstructures to the greatest possible extent. The specimens were then mechanically polished to a 0.05μm Al_2O_3 finish and degreased ultrasonically before being mounted in a Perkin-Elmer PHI-600 scanning Auger microprobe (base pressure $\approx$ $1x10^{-7}$ Pa). The surfaces were cleaned *in situ* by sputtering with 3 keV Ar^+ ions at a current density of 16 $\mu A/cm^2$ and incident angle off the surface normal, θ_i, of 45°. The sputtering process resulted in an enrichment of Al at the surface due to preferential sputtering of Mg atoms (see below). No post-sputtering annealing stage was performed in order to avoid any further segregation of Al and impurity elements to the surface or

to the grain boundaries. It was shown in Chapter 4 that the rate of initial oxygen uptake on pure magnesium was affected by the level of prior ion bombardment. The total ion dose was therefore purposefully kept low ($< \approx 5 \times 10^{16}$ ions/cm^2) and the uptake of oxygen was continuously checked against that on pure magnesium surfaces under exactly identical conditions. In this way, it was believed that reliable comparisons could be made between the rate of oxygen uptake on Mg-Al surfaces and that on pure magnesium surfaces.

Table 5.1: Major impurities present in Mg-Al specimens determined by spark source mass spectroscopy (ppma).

	Zn	Mn	Fe	O	N	Si	P	S	Cl
Mg-8.5Al	74	7	4	6	2	5	0.2	0.3	0.8
Mg-3.0Al	74	9	7	6	2	5	0.2	0.3	0.8

The sputtering process was sufficient to remove the polishing damage layer thus revealing the grain contrast of the specimens. Grains which exhibited very dark secondary electron contrast were chosen for detailed AES analysis. Grains of similar contrast levels on pure Mg were previously found to have surface normals very near the basal Mg(0001) pole in electron back scattering diffraction patterns (EBSDP's) (section 2.4).

Auger and XPS spectra of the clean and water-dosed surfaces were obtained using the same experimental conditions as outlined in Chapter 3. The principal AES features of the water-dosed specimens are the $O(K_1L_{23}L_{23})$ transition at 510 eV, the metallic $Mg(L_{23}VV)$ transition at 45 eV, the oxidic $Mg(L_{23})O(L_{23})O(L_{23})$ transition at 34 eV, the metallic $Al(L_{23}VV)$ transition at 68 eV and the oxidic $Al(L_{23})O(L_{23})O(L_{23})$ transition at 55 eV [Chapter 3, 5.12].

5.3. Results and Discussion

Figure 5.1 shows the effect of the sputtering process on the enrichment of Al at the surface of the two alloys under investigation. The atomic fraction of Al at the surface was calculated from the ratio of the peak-to-peak amplitude of the Al(LVV) AES signal to the sum of the peak-to-peak amplitudes of the Al(LVV) and Mg(LVV) AES signals at 68 eV and 45 eV kinetic energy respectively. These signals were normalized to the intensities for pure Mg and Al standards and the intensity loss originating from subsurface contributions was accounted for by using appropriate attenuation factors [5.13]. The surface concentration of Al was also verified using XPS (squares in Figure 5.1) following ion bombardment to several different ion dose levels. Quantification of XPS data was achieved by correction of the integrated Al(2p) (binding energy = 72.8 eV) and Mg(2p) (binding energy = 49.9 eV) intensities with appropriate photoelectron cross-sections [5.14] using software developed by Surface Science Laboratories, Inc.

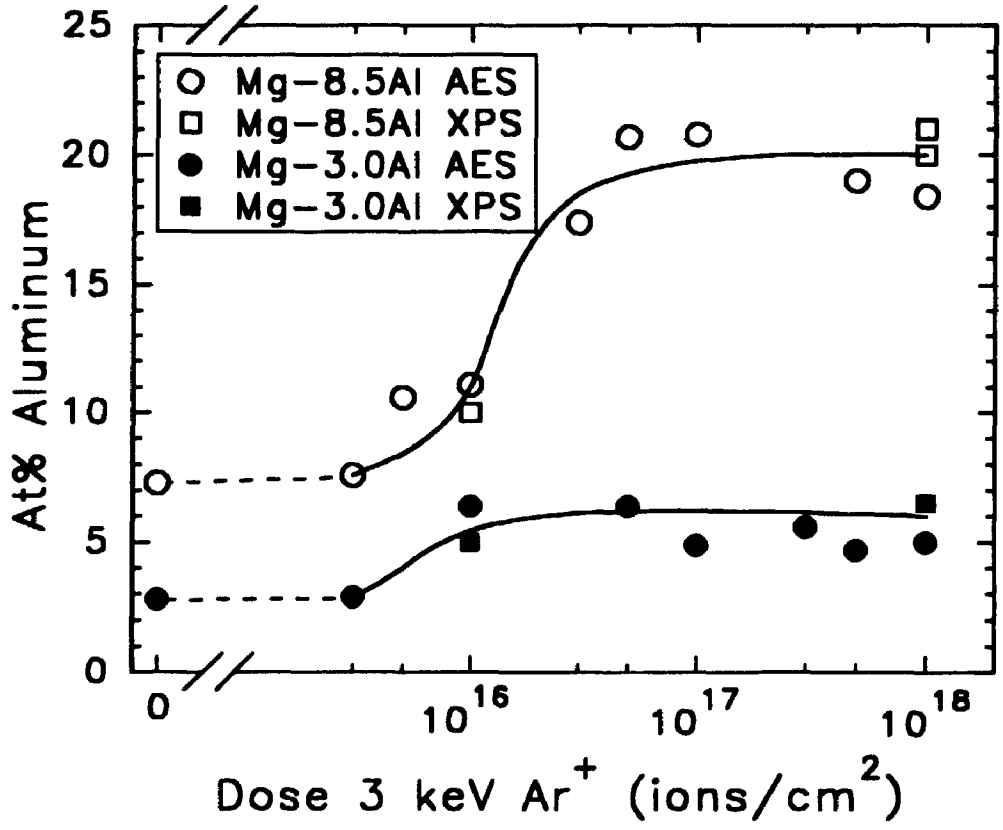

Figure 5.1: The effect of the initial sputter-cleaning process on the enrichment of Al at the surface of the Mg-Al alloys.

These cross-sections were corrected to account for the different inelastic mean free paths (IMFP's) for photoelectrons of differing kinetic energies. The good agreement between the AES and XPS results is apparent in the figure.

From Figure 5.1, it is evident that the degree of sputter-induced Al enrichment at the surface is most pronounced for the Mg-8.5Al alloy. The surface of this specimen was enriched with ≈20 at% Al (22 wt% Al) at total ion doses exceeding about 5×10^{16} ions/cm^2. The enrichment of Al on the Mg-3.0Al alloy surface, on the other hand, was less drastic. The surface concentration of Al in this specimen was quickly saturated at ≈6 at% (7 wt%) at ion doses greater than 1×10^{16} ions/cm^2. Even though the composition of this latter specimen moves into a two-phase region of the phase diagram during sputtering [5.15], no segregation of phases is expected to occur. Braun et al. [5.16] used electron energy loss spectroscopy (EELS) to show that the values of the plasmon energies for sputtered Mg-3.0Al specimens matched the values of scribed samples when the sputter-induced alteration of surface composition was taken into account. These authors then concluded that no segregation of phases occurs during sputtering of these alloys. The segregation of Al to the surface may in fact allow for a better comparison with industrial alloys, since surface segregation of Al is expected to occur during heat treatment [5.8].

Figure 5.2 shows the changes in the low-energy derivative Auger spectra of the Mg-8.5Al alloy surface (surface concentration 20 at% Al) for increasing exposures to D_2O up to 10 L. Similar changes were observed for the Mg-3.0Al specimen. The spectrum labelled "clean" in Figure 5.2 is characterized by the metallic Al($L_{2,3}$VV) AES

Figure 5.2: Representative Auger spectra of the clean Mg-8.5Al surface and the same surface exposed to the indicated exposures of D_2O.

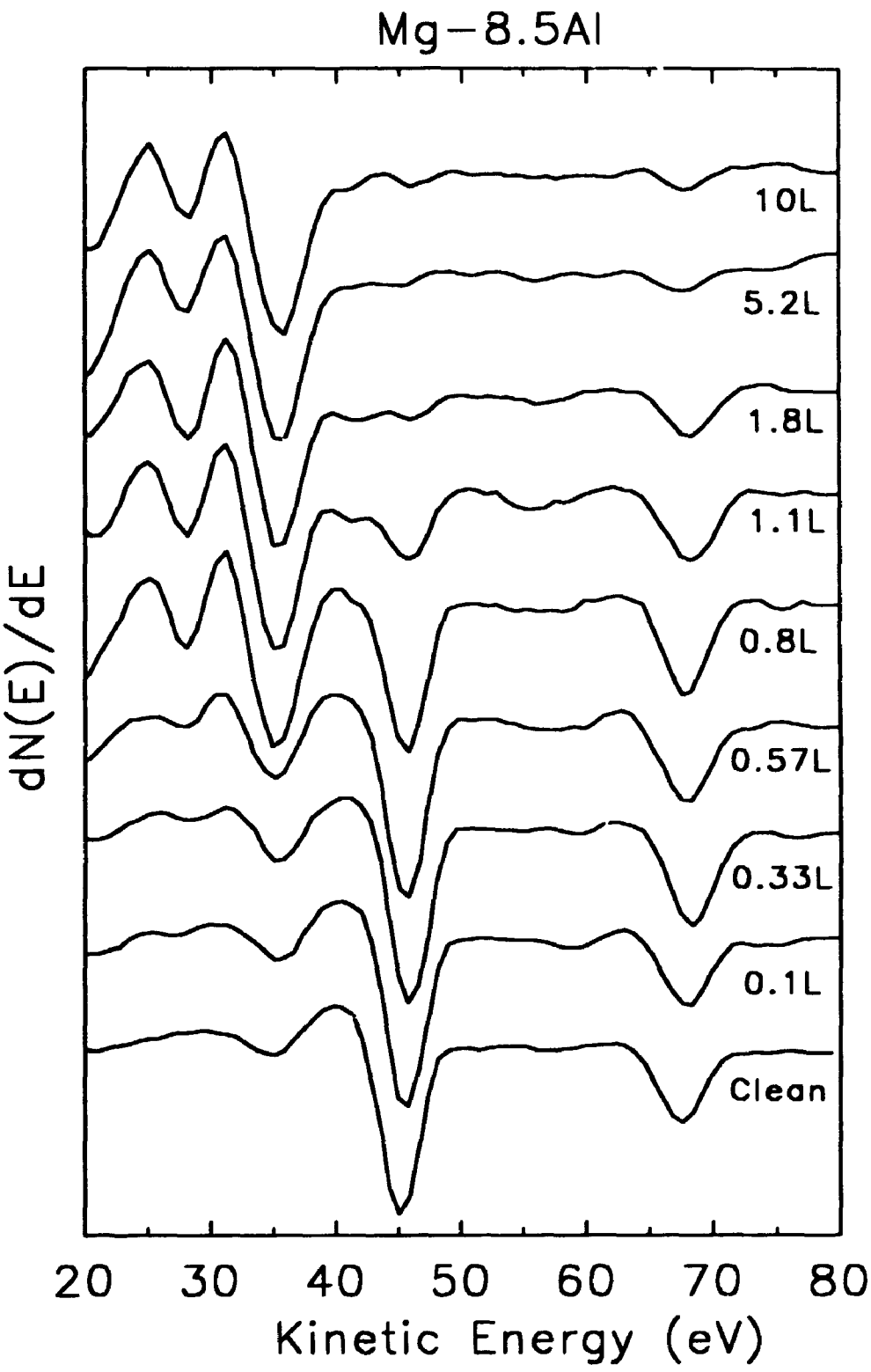
Mg−8.5Al
10L
5.2L
1.8L
1.1L
0.8L
0.57L
0.33L
0.1L
Clean
dN(E)/dE
20
30
40
50
60
70
80
Kinetic Energy (eV)

transition at 68 eV, the metallic Mg(L_{23}VV) transition at 45 eV and the overlapping surface and bulk plasmon loss satellites from the Mg signal at 34 eV. Exposing the clean surface to increased doses of D_2O results in an attenuation of the metallic Al and Mg signals and a growth of the 34 eV signal. The latter also represents the main oxidized Mg(L_{23})O(L_{23})O(L_{23}) Auger transition. Increasing exposures to D_2O also results in the appearance of a new peak at 27 eV, representative of an interfacial Mg(L_{23})O(L_1)Mg(V) transition, or a cross-transition occurring at the metal-oxygen interface [5.17]. The presence of this peak at exposures as low as 0.1 L indicates that true chemical bonding exists between oxygen atoms present on the surface and magnesium atoms present in the substrate. Finally, a weak signal at 56 eV appears at low D_2O exposures. This peak, which represents the oxidized Al(L_{23})O(L_{23})O(L_{23}) transition, is fully extinguished following a 10 L exposure. These changes were accompanied by the simultaneous appearance and subsequent growth of an O($K_1L_{23}L_{23}$) transition at 510 eV (not shown).

Figure 5.3 shows the evolution of the peak-to-peak intensities of the Mg(LVV) (45 eV), the Al(LVV) (68 eV) and the O(KLL) (510 eV) AES signals as a function of D_2O exposure for (a) Mg-8.5Al and (b) Mg-3.0Al surfaces. The measurements were made on several grain faces of each specimen that exhibited similar secondary electron contrast levels. The intensity of each component in Figure 5.3 has been normalised to the clean Mg(LVV) signal. From the figure, it is evident that the initial interaction of water vapour with Mg-Al surfaces results in a three-stage oxidation behaviour similar to that observed for pure magnesium (Chapter 3), viz. a slow oxygen uptake during low exposures ($< \approx 0.5$ L), a rapid increase in uptake rate at intermediate exposures (≈ 0.5

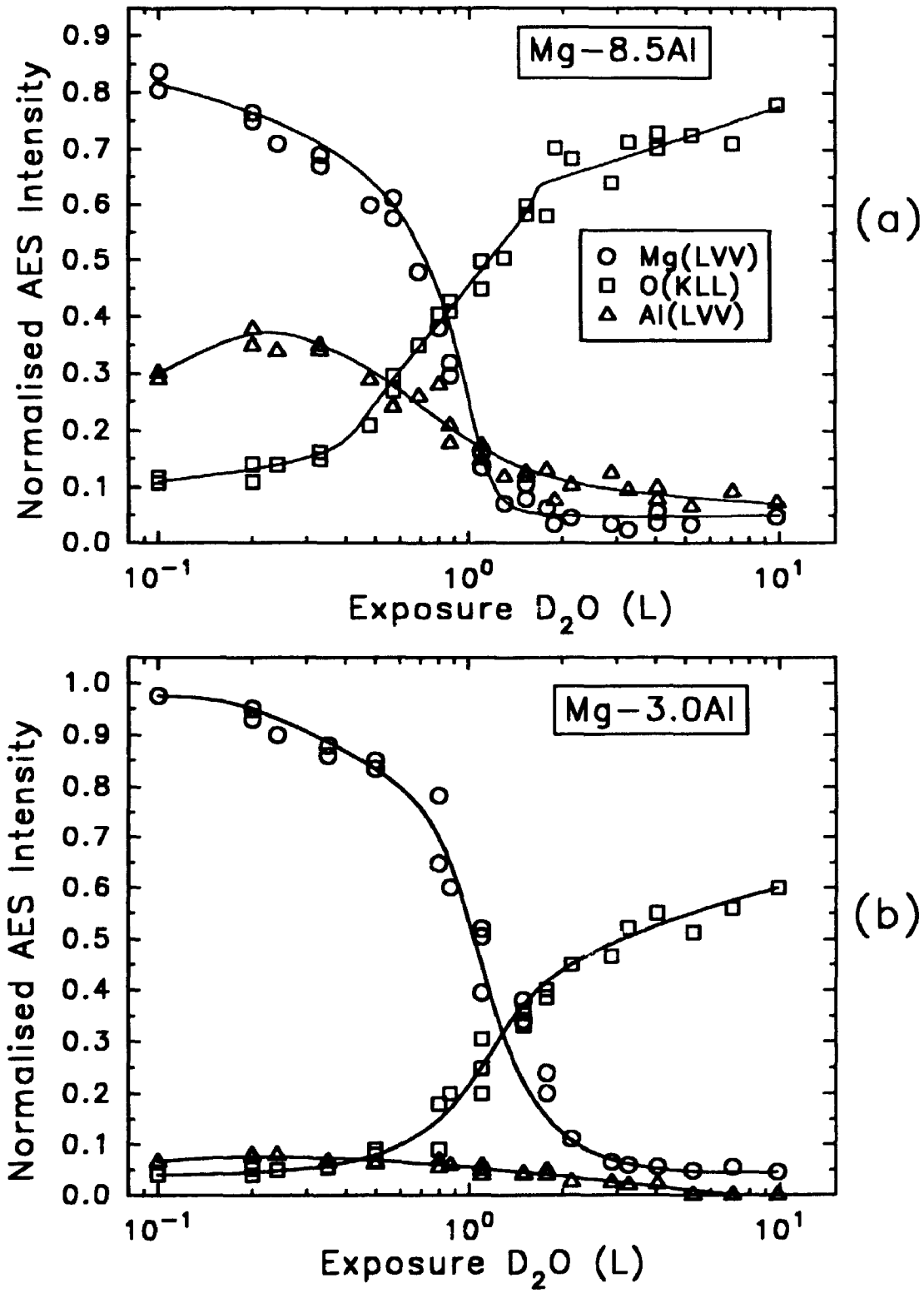

Figure 5.3: The evolution of the peak-to-peak intensities of the Mg(LVV) (45 eV), the Al(LVV) (68 eV) and O(KLL) (510 eV) AES signals as a function of D_2O exposure for (a) Mg-8.5Al and (b) Mg-3.0Al surfaces. The intensities were normalised to the clean Mg(LVV) signal intensity.

L to ≈ 3 L), and a slow, more gradual increase in uptake to higher exposures (> ≈3 L). This three-stage oxidation behaviour will be discussed more thoroughly below.

The changes occurring in the AES spectra presented in Figures 5.2 and 5.3 allow for a qualitative description of the initial stages of the interaction of water vapour with Mg-Al surfaces. At very low exposures (0.1 L to ≈ 0.8 L), the metallic Mg(LVV) and Al(LVV) AES signals are attenuated by a small amount relative to the clean surface and weak signals appear at ≈ 27 eV and ≈ 55 eV kinetic energy. The simultaneous appearance of an O(KLL) signal at 510 eV indicates that, at room temperature, water vapour dissociates on the Mg-Al alloy surfaces leading to the concurrent chemisorption of oxygen on *both* Mg and Al atoms present on the surface. Esposto et al. [5.18] recently observed a similar simultaneous reaction of O_2 with both Mg and Al atoms on the surface of a Mg-segregated Al-Mg alloy using AES and static secondary ion mass spectrometry (SSIMS). The simultaneous reaction of water vapour with both Mg and Al atoms is consistent with the small electronegativity difference between Mg (1.2 eV) and Al (1.5 eV).

It is also noteworthy that the intensity of the metallic Al(LVV) AES signal was observed to *increase* slightly during very short exposures on both Mg-8.5Al and Mg-3.0Al surfaces (Figure 5.3). This small increase could be indicative of a chemisorption-induced segregation of Al atoms from within deeper layers. Such a mechanism has previously been observed for alloying elements which possess the greatest affinity for oxygen [5.19]. The fact that aluminum atoms diffuse to the surface following the

adsorpton of oxygen atoms can again be attributed to the small difference in electronegativity between Mg and Al.

At increasing exposures (above ≈ 0.5 L), both the Mg and Al metallic signals are rapidly attenuated (Figure 5.3). These changes are accompanied by an equally rapid growth in the oxidized Mg (34 eV) AES peak (Figure 5.2). The oxidized Al (55 eV) signal, on the other hand, does not grow proportionately and is in fact extinguished by ≈ 10 L exposure. These observations suggest that, following adsorption, magnesium oxide islands are preferentially nucleated on the alloy surface and subsequently grow to cover the mixed Mg-Al-O chemisorbed precursor layer.

Further evidence for this description of the early stages of oxide growth on Mg-Al surfaces, viz. preferential nucleation and growth of MgO islands, can be obtained by examining the ratio $(Al/Al^{clean})/(Mg/Mg^{clean})$ during increasing exposures to water vapour. Such a ratio effectively describes the relative attenuation of the metallic Al AES signal compared to the corresponding attenuation of the metallic Mg AES signal as the oxide overlayer is formed on the Mg-Al substrate. Figure 5.4 shows the evolution of this ratio for increasing exposures to D_2O on Mg-8.5Al and Mg-3.0Al surfaces. Three regions are again clearly resolved. At low exposures, the ratio $(Al/Al^{clean})/(Mg/Mg^{clean})$ is constant at unity, thus indicating that both the Al and Mg AES signals are attenuated by the same amount during this exposure range. As the exposure is increased beyond ≈ 0.5 L (Mg-8.5Al) or ≈ 0.8 L (Mg-3.0Al), the ratio $(Al/Al^{clean})/(Mg/Mg^{clean})$ increases rapidly, indicating that the AES signal originating from metallic Mg atoms is attenuated much more rapidly than is that originating from metallic Al atoms in the substrate. Finally,

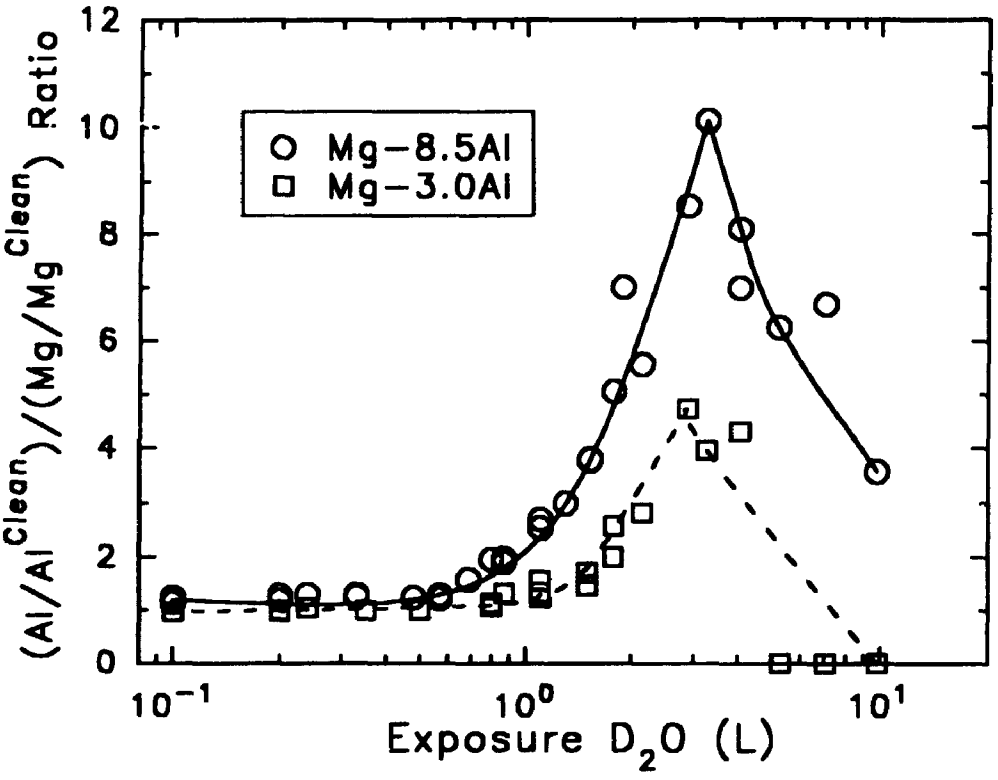

Figure 5.4: The evolution of the ratio $(Al/Al^{clean})/(Mg/Mg^{clean})$ for increasing exposures to D_2O on Mg-Al surfaces. This ratio describes the relative attenuation of the metallic Al AES signal compared to the metallic Mg AES signal as the oxide overlayer is formed.

at an exposure of ≈ ? L D_2O the ratio drops abruptly for both surfaces, suggesting a sudden attenuation of the Al(LVV) intensity at this exposure value.

These observations can easily be explained by assuming that the build-up of oxide on Mg-Al surfaces proceeds in three stages: dissociative chemisorption during low exposures to D_2O; oxide nucleation and growth by islands during intermediate exposures; and slow, diffusion-controlled bulk oxide thickening following coalescence of the oxide islands. At low exposures, therefore, water vapour dissociates on the alloy surface leading to chemisorption of oxygen on both Mg and Al atoms. The equal attenuation of both the metallic Mg and Al AES signals in Figure 5.4 during this regime suggests that the chemisorption process is homogeneous across the surface. Bulk oxide is then nucleated at exposures of ≈ 0.5 to 0.8 L D_2O. The fact that the Mg(LVV) AES intensity is attenuated much more rapidly than is the Al(LVV) intensity during this regime (Figure 5.4) suggests that the island growth process proceeds preferentially above alloy regions that are Mg-rich. Finally, once these islands of MgO coalesce, the Al-rich regions which previously did not support oxide growth are abruptly covered with several layers of magnesium oxide, resulting in the observed sudden drop in the $(Al/Al^{clean})/(Mg/Mg^{clean})$ ratio (Figure 5.4).

It should be noted that a *homogeneous* island growth model would also be expected to produce the general shape of the curve in Figure 5.4 due to the different escape depths of the Mg(LVV) and Al(LVV) Auger electrons. Since the kinetic energy of the Mg(LVV) Auger electrons is lower than that of the Al(LVV) Auger electrons, their inelastic mean free path (IMFP) and thus their escape depth, λ, is shorter (Appendix

A). Now, if it is assumed that an oxide island growth mode is operative, then the relative intensity of the substrate metal Auger electrons can be calculated from the well-known exponential attenuation of emitted electron intensity from a solid (equation 2.5, Chapter 2) and is found to be:

$$\frac{I}{I^{clean}} = \theta_{isl} \cdot \exp(-\frac{N}{\lambda}) + (1-\theta_{isl}) \qquad (5.1)$$

where I/I^{clean} is the relative intensity of the substrate metal Auger electrons normalised to that from a clean surface, θ_{isl} is the coverage of oxide islands on the surface ($0 \leq \theta_{isl} \leq 1$), N is the average number of layers in the islands and λ is the escape depth of the appropriate Auger electrons in monolayers (ML). Figure 5.5(a) shows the results of a simulation using equation (5.1) to estimate the ratio $(Al/Al^{clean})/(Mg/Mg^{clean})$ for the homogeneous growth of oxide islands on an Mg-Al alloy surface. The escape depths of the Mg(LVV) and Al(LVV) Auger electrons used in the simulation were calculated using the inelastic scattering model of Tanuma et al. [5.20] and were found to be $\approx$0.33 nm (1.56 ML MgO) and 0.34 nm (1.61 ML MgO) respectively for the instrument geometry (Appendix A). The resulting curves presented in Figure 5.5(a) show that the general shape of Figure 5.4 can be realised for high relative island coverages. However, in order for the *magnitude* of the observed changes in $(Al/Al^{clean})/(Mg/Mg^{clean})$ (Figure 5.4) to be reproduced, the escape depth, λ, of the Al(LVV) Auger electrons would have to be more than 10 times that of the Mg(LVV) Auger electrons. Since this cannot

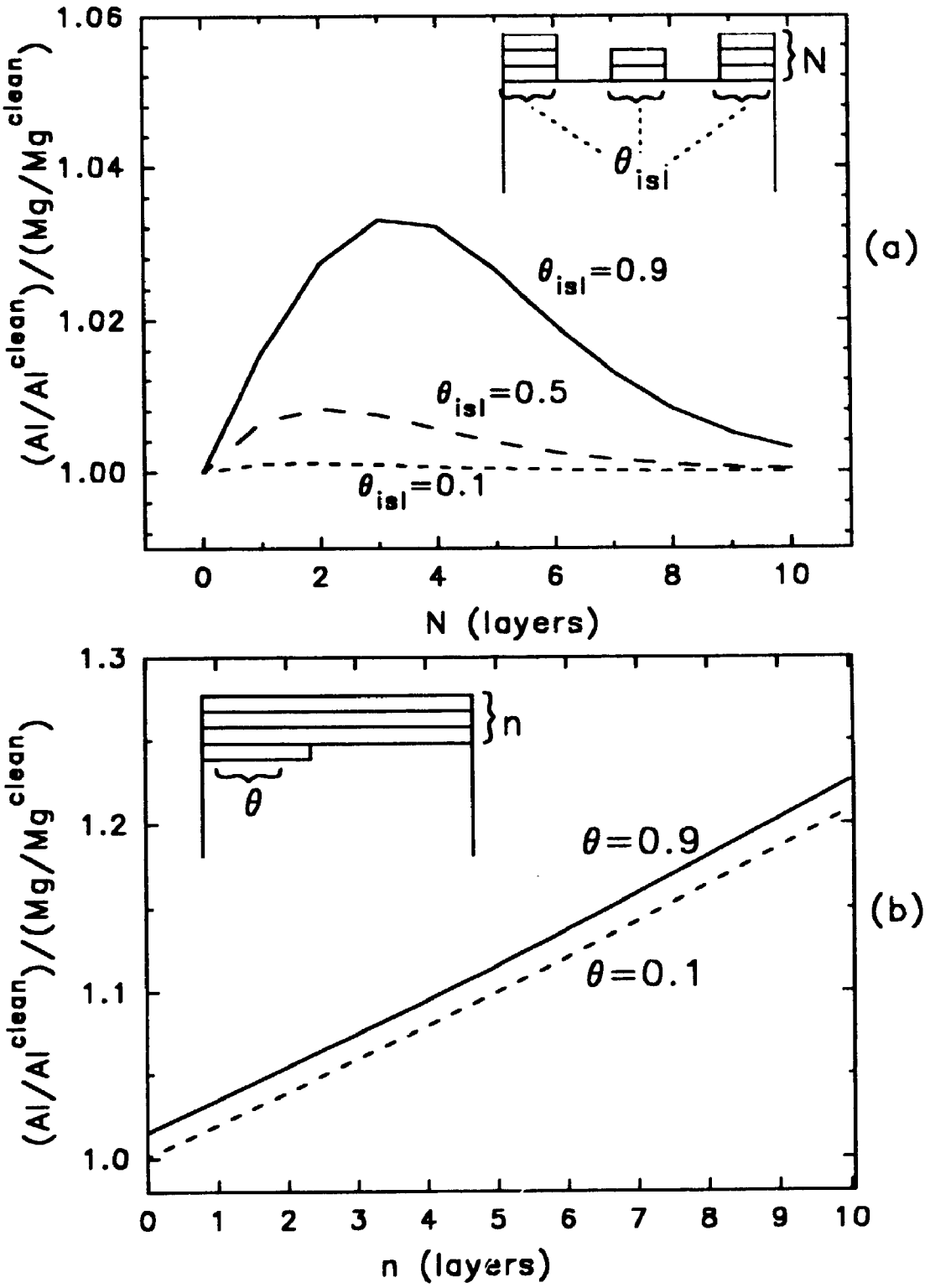

Figure 5.5: Results of simulations using (a) equation (5.1) for the homogeneous growth of oxide islands and (b) equation (5.2) for the layer-by-layer growth of oxide to estimate the ratio $(Al/Al^{clean})/(Mg/Mg^{clean})$ during the formation of an oxide overlayer on Mg-Al surfaces.

obviously be the case, it is concluded that the island growth process occurs preferentially above Mg-rich areas on the surface. It should also be noted that the general shape of Figure 5.4 cannot be reproduced using a layer-by-layer oxide growth model. Figure 5.5(b) shows the results of a such a simulation using the following expression for layer-by-layer growth:

$$\frac{I}{I^{clean}} = \theta \cdot \exp\{\frac{-(n+1)}{\lambda}\} + (1-\theta) \cdot \exp(-\frac{n}{\lambda}) \qquad (5.2)$$

where θ is the coverage of interface oxide ($0 \leq \theta \leq 1$); and n is the number of completed oxide layers not including the interface oxide. From Figure 5.5(b) it is evident that the ratio $(Al/Al^{clean})/(Mg/Mg^{clean})$ increases continuously during the layer-by-layer build-up of oxide on an Mg-Al alloy surface. This provides further evidence that the oxidation process involves the nucleation and growth of oxide islands.

It was shown in Chapter 3 that useful information regarding the first two stages of the oxidation process (i.e. chemisorption and island nucleation and growth) could be obtained by fitting the experimental I/I^{clean} (i.e. Mg/Mg^{clean}) data to theoretical models. The kinetics of the first two stages of the oxidation process were described by equations (3.3) and (3.6), respectively. Equations (3.3) and (3.6) were therefore fitted to the Mg/Mg^{clean} data (open circles in Figure 5.3) using non-linear regression. The data have been re-plotted in Figure 5.6 along with the lines of best fit obtained for the parameter

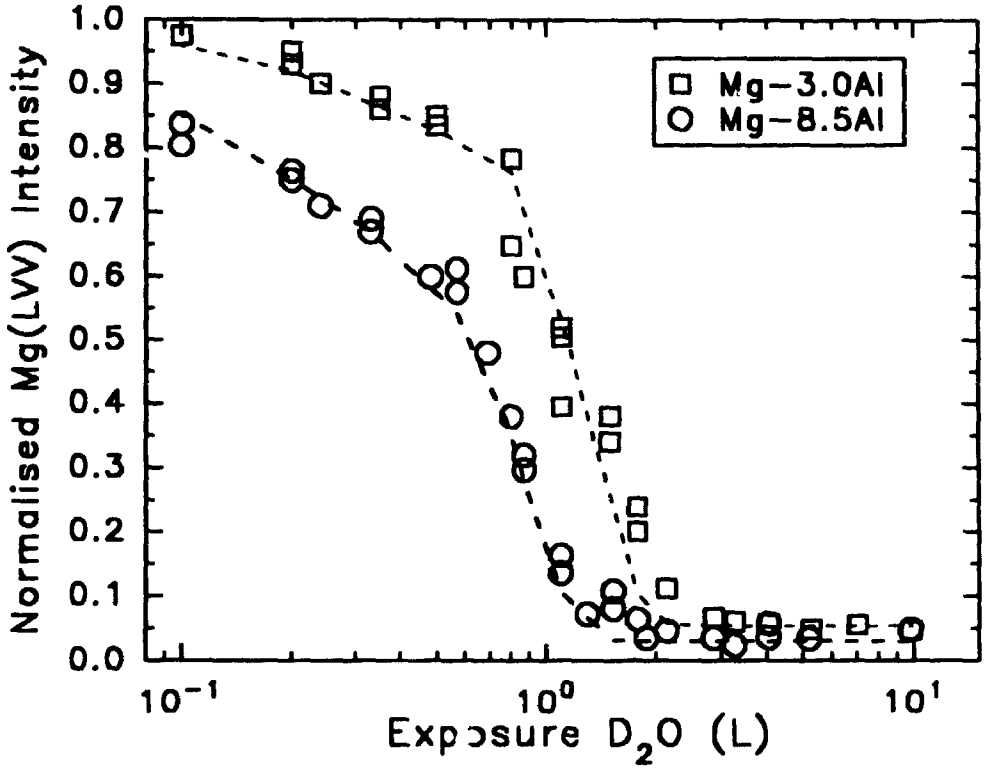

Figure 5.6: The attenuation of the metallic Mg(LVV) AES signal for Mg-Al surfaces. The dashed lines represent the lines of best fit for equations (3.3) and (3.6) with the parameter estimates of Table 5.2.

estimates given in Table 5.2. Table 5.2 also contains the parameter estimates obtained in Chapter 3 for pure Mg substrates. It should be noted that the best-fit values for the escape depth of the Mg(LVV) Auger electrons, λ, fell within the range of 1.5 to 1.8 ML MgO, again in good agreement with the value estimated using the empirical expressions of Tanuma et al. [5.20] ($\approx$ 1.5 ML). In addition, the fitted values for L_o, the exposure value at which oxide nuclei first appear, closely match the exposure values at which the ratio $(Al/Al^{clean})/(Mg/Mg^{clean})$ deviates from unity for the respective Mg-Al alloy surfaces (Figure 5.4). These observations suggest that the parameter estimates presented in Table 5.2 are reasonably accurate.

Table 5.2: Best-fit parameter estimates for calculation of curves in Figure 5.6 after equations (3.3) and (3.6).

	λ (ML)	L_o (L)	n (ML)	K (L^{-1})	C (L^{-2})
Mg-8.5Al	1.7	0.50	6.0	5.3	5.4
Mg-3.0Al	1.8	0.80	4.9	1.1	3.1
Pure Mg	1.5	0.70	4.2	1.6	0.41

These parameter estimates then allow for a semi-quantitative description of the first two stages of oxide growth on Mg-Al alloy surfaces. For example, the best-fit parameters suggest that MgO islands nucleate on the Mg-8.5Al surface at an exposure

of ≈ 0.5 L D_2O and that these islands subsequently grow to an average height of ≈ 6 ML MgO prior to coalescence. The coverage at nucleation, θ^{nucl}, can then be estimated by recognising that the parameter K in equation (3.3) is a constant relating the gas impingement rate to the number of adsorption sites and is given by equation (3.8):

$$K = \frac{1}{(2\pi mkT)^{1/2} N_o^{nucl}} \tag{3.8}$$

where m is the mass of the oxygen atom; kT is the thermal energy of the gas; and N_o^{nucl} is the number of occupied sites at the end of the chemisorption stage. For K = 5.3 (Table 5.2), therefore, we obtain $N_o^{nucl} = 8.6 \times 10^{13}$ cm^{-2}. Now, if the number of available adsorption sites, N_o, is taken to be the surface atom density of Mg(0001) (1.1×10^{15} cm^{-2}) then the coverage at nucleation is $\theta^{nucl} = N_o^{nucl}/N_o = 9.4 \times 10^{13}/1.1 \times 10^{15} \approx 0.09$. For Mg-3.0Al, on the other hand, nucleation of MgO is slower, occurring at a higher total exposure value (≈ 0.8 L) and a higher coverage at nucleation ($\theta^{nucl} = 4.5 \times 10^{14}/1.1 \times 10^{15} \approx 0.41$). In addition, the oxide islands on Mg-3.0Al surfaces grow to a smaller average height (≈ 5 ML) prior to coalescence as compared to those on Mg-8.5Al surfaces. Finally, for pure Mg surfaces exposed to D_2O under identical conditions, it was found that oxide island nucleation occurred at an exposure of ≈ 0.70 L D_2O and continued until an average island height of ≈ 4 ML MgO had been reached (Chapter 3). The coverage at nucleation for these specimens was approximately $\theta^{nucl} = 3.2 \times 10^{14}/1.1 \times 10^{15} \approx 0.29$.

From the above description, it is evident that the presence of Al as a bulk alloying addition affects the kinetics of initial oxygen uptake on magnesium surfaces. The results also indicate that it is likely the two-phase nature of the alloy that may play a significant role in the early stages of oxide formation. The solid solubility of Al in Mg is known to be low ($\approx$ 2 wt%) [5.15]. However, for Mg-Al specimens that have been solution heat-treated and quenched, a supersaturated solid solution can remain stable at room temperature, depending on the aluminum content. Generally, for compositions less than about 8 wt% Al, only few second-phase precipitates form (precipitation hardening is weak) [5.15]. This may help explain the very similar initial oxidation behaviour observed on Mg-3.0Al surfaces and pure Mg surfaces. Both of these specimens exhibited oxide nucleation at similar total D_2O exposures and surface oxygen coverages (see above). The fact that some evidence for preferential oxide growth above Mg-rich areas was observed (Figure 5.4) suggests that the Mg-3.0Al alloy is not fully homogeneous. For aluminum compositions exceeding about 8 wt%, on the other hand, appreciable second-phase precipitation is possible (precipitation hardening is strong) [5.15]. This then helps explain the significant difference in initial oxidation behaviour observed on Mg-8.5Al surfaces compared to pure Mg surfaces. The nucleation of oxide was observed to be greatly facilitated on the Mg-8.5Al surface, occurring at a lower total exposure and much lower total coverage. In addition, the preferential growth of MgO above Mg-rich regions was appreciable (Figure 5.4), implying that oxide nucleation is impaired over the second-phase precipitate regions. It appears, therefore, that the overall increase in reaction rate may be simply due to a reduced total reaction area exposed to

an equivalent total reactant flux. The incident water molecules can thus presumably migrate freely over the precipitate regions (i.e. surface diffusion is easy) and attach themselves to the growing oxide islands in the Mg-rich areas.

At exposures exceeding ≈ 2 to 3 L D_2O, the normalised O(KLL) AES intensities in Figure 5.3 show what appears to be the beginning of a logarithmic-type bulk oxide thickening regime on the Mg-Al alloy surfaces. At these exposures, however, the low-energy Mg(LVV) and Al(LVV) AES signals are almost completely extinguished. In order to follow the oxide growth process to much higher total exposures, therefore, XPS was employed. Because the photoelectrons of interest are of relatively high kinetic energy (i.e. relatively long IMFP) as compared to the corresponding Auger electrons, information can be obtained for greater total film thicknesses. Figure 5.7 shows the changes in the Mg(2p) and Al(2p) XPS spectra of the Mg-8.5Al surface for increasing exposures to D_2O up to 1×10^6 L. Similar changes were observed on the Mg-3.0Al specimen. The spectrum labelled "clean" in Figure 5.7 shows the presence of two narrow peaks at 49.9±0.05 eV binding energy (b.e.) and 72.8±0.05 eV b.e., representative of the metallic Mg(2p) (Mg^o) and metallic Al(2p) (Al^o) XPS peaks respectively. The broad feature at ≈ 61 eV b.e. is due to a plasmon loss satellite from the Mg(2p) band. Increasing exposures to water vapour leads to the development of shoulders to the high binding energy side of both metallic lines. The shoulder on the Mg(2p) peak develops shifted approximately 1.6 eV to higher binding energies and is identical to that observed for heavily oxidised Mg and for bulk MgO [5.21]. Similarly, the shoulder on the Al(2p) peak appears shifted approximately 2.5 eV to

Figure 5.7: Representative XPS spectra of the clean Mg-8.5Al surface and the same surface exposed to the indicated exposures of D_2O.

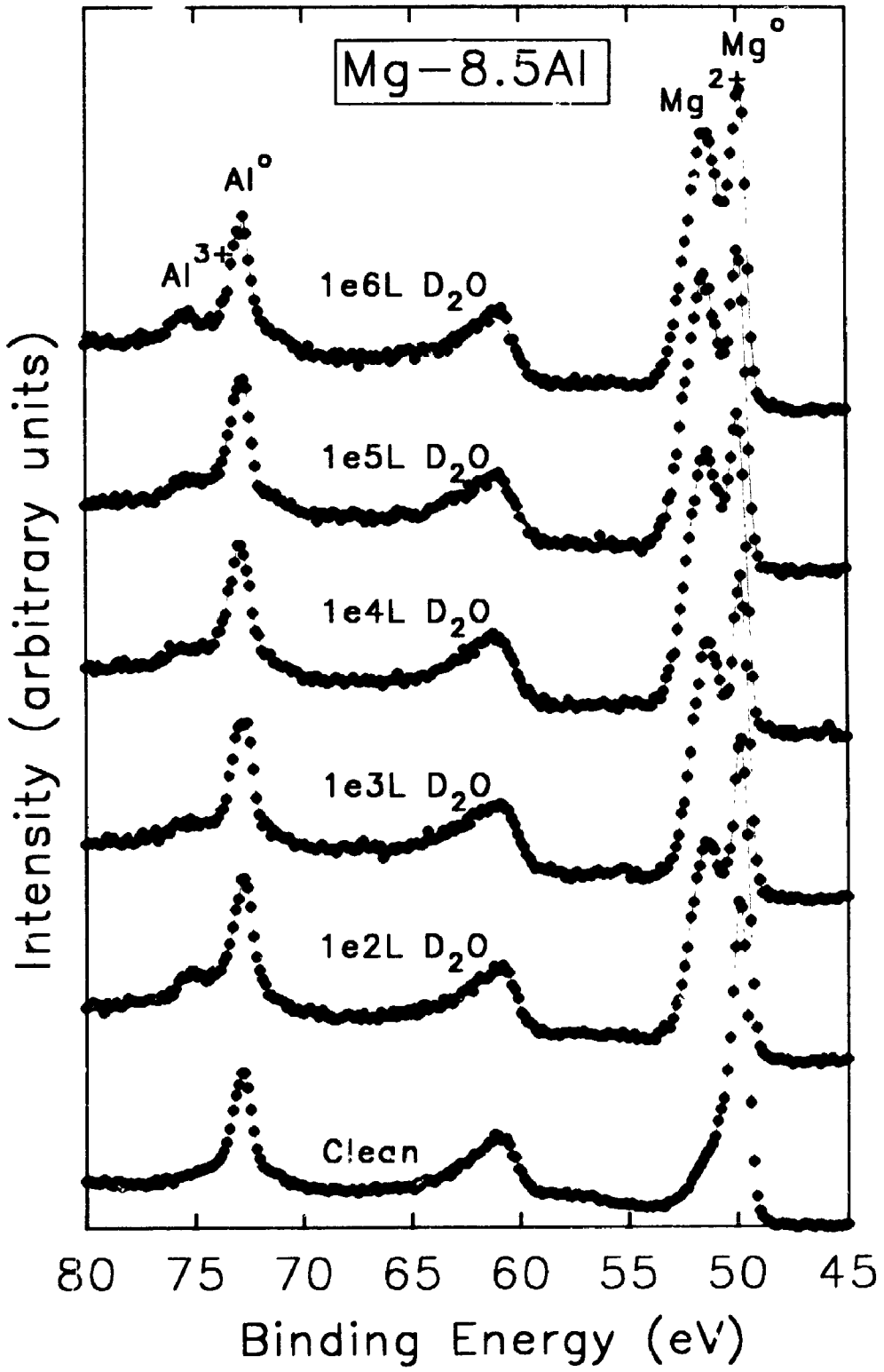
Mg−8.5Al
Mg°
Mg2+
Al°
Al3+
1e6L D2O
1e5L D2O
1e4L D2O
1e3L D2O
1e2L D2O
Clean
Intensity (arbitrary units)
80 75 70 65 60 55 50 45
Binding Energy (eV)

higher binding energies and is similar to that observed on heavily oxidised Al and on Al_2O_3 [5.21-5.23]. These lines are consequently labelled Mg^{2+} and Al^{3+} in Figure 5.7. From the figure, it is evident that exposure to water vapour results in the growth of a mixed Mg-Al oxide on the alloy surface. In addition, the Al^{3+} signal remains relatively weak even at very high exposures, suggesting that the overlayer consists mainly of MgO with relatively small numbers of Al^{3+} cations being built into the oxide structure.

In order to examine the kinetics of the bulk thickening regime in a quantitative fashion, the thickness of the oxide layers formed at various total exposures was determined by measuring the intensity ratio of the oxidic (Mg^{2+}) to metallic (Mg^{o}) XPS peaks, as described in Chapter 3. Figure 5.8 shows the oxide thickness versus exposure on Mg-8.5Al and Mg-3.0Al surfaces calculated using the measured I_o/I_m ratios and equation (3.9) for exposures ranging from 100 to 1×10^6 L. The equivalent oxide film thicknesses for the short exposure range (0.1 to 10 L) were estimated using the previous Mg/Mg^{clean} AES data and equation (3.10). The dashed line in Figure 5.8 represents the best fit to data obtained previously for pure Mg surfaces (Chapter 3). From the figure, it is evident that the bulk thickening regime following coalescence of the oxide islands on Mg-Al surfaces follows a logarithmic-type course, similar to that observed on pure Mg. In addition, the rate of film thickening is slower on the Mg-Al alloy surfaces compared to that on pure Mg, despite the fact that the oxide islands grow more quickly and to a greater average height in the previous stage.

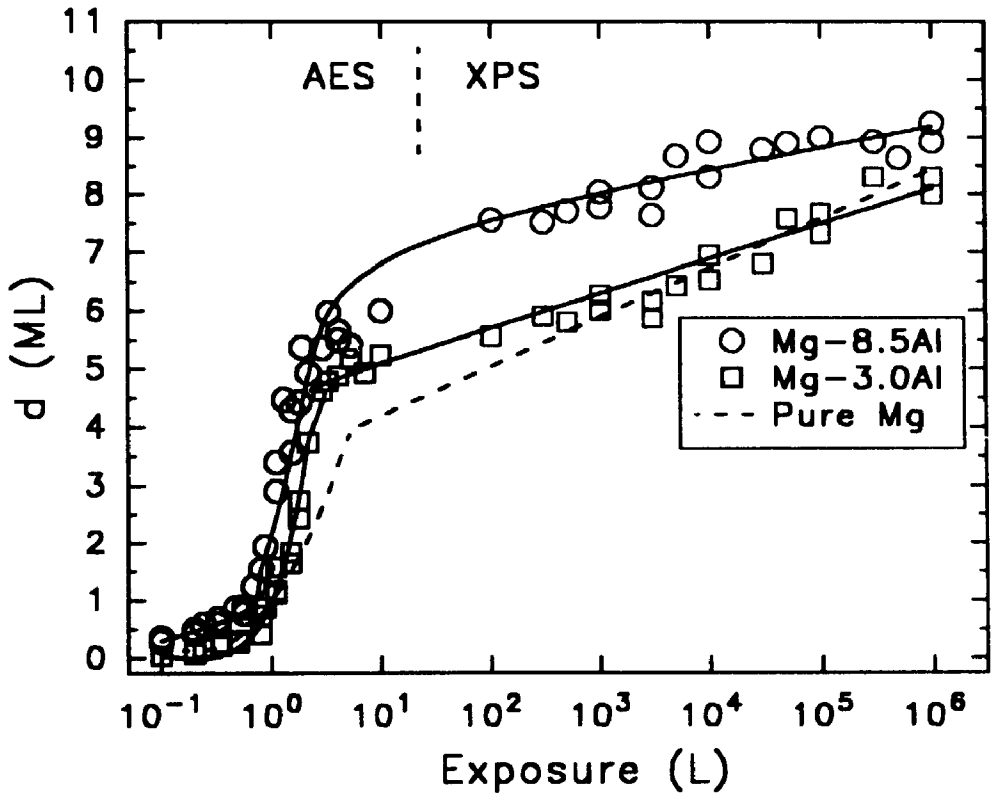

Figure 5.8: The growth of oxide on Mg-Al surfaces monitored by AES (0 to 10 L) and XPS (100 to 1 × 10^6 L). The dashed line represents the best fit line to data obtained previously for pure Mg surfaces (Chapter 3).

Logarithmic growth of thin oxide films at low temperatures is usually described in terms of the Cabrera-Mott theory of metal oxidation [5.24]. The basic hypothesis of this theory is that adsorbed oxygen produces electronic trap sites at the oxide/gas interface and that electrons then freely pass through the oxide to populate these sites, thus equalizing the Fermi level in the metal and the adsorbed layer. The electrons can traverse the oxide film by any number of mechanisms, including quantum tunneling, impurity conduction or Schottky emission into the oxide conduction band. A contact potential, V, is thus set up between the substrate and the adsorbed oxygen, creating an electric field, E, such that $E=V/x$, where x is the film thickness. Since the film is usually very thin, the field is strong enough to significantly alter the activation barrier for the diffusion of ions or other charged defects. Field-dependent transport of ionic defects therefore constitutes the rate-limiting step in the oxidation process.

The fundamental equation describing oxide growth according to Cabrera and Mott is:

$$\frac{dx}{dt} = a\nu\exp[-\frac{W}{kT}]\ \sinh[\frac{qaE}{kT}] \qquad (5.3)$$

where a is one half the distance separating equilibrium ion sites; ν is the ion jump attempt frequency ($\approx 10^{12}$ sec^{-1}); W is the activation barrier for defect motion; q is the magnitude of charge on the defect; E is the electric field strength; and kT is the thermal energy. Cabrera and Mott [5.24] provide an approximate integration of equation (5.3):

$$\frac{X_1}{x} = A - B\ln t \tag{5.4}$$

where $X_1 = qaV/kT$ and A and B are constants. Equation (5.4) represents the well-known inverse logarithmic law for oxide growth at low temperatures. Much debate has centred around the validity of equation (5.4). It has been practically impossible to graphically distinguish between inverse logarithmic and direct logarithmic kinetics [5.25] and, in fact, Ghez [5.26] showed rigorously that equation (5.4) is *not* an asymptotic solution to equation (5.3). Instead, he carried out a more exact integration of equation (5.3) and found:

$$\frac{X_1}{x} = -\ln\left(\frac{t+\tau}{x^2}\right) - \ln(X_1 u) \tag{5.5}$$

where τ is a constant, and

$$u = N\Omega\nu\exp\left(-\frac{W}{kT}\right) \tag{5.6}$$

$$X_1 = \left|\frac{qaV}{kT}\right| \tag{5.7}$$

where N is the density of mobile defects at the interface and Ω is the volume of oxide per defect. Equation (5.5) allows for a better test of the Cabrera-Mott theory. Experimental data can be fitted to predicted parametric relationships by plotting $1/x$ versus $ln(t/x^2)$. The resulting plot should yield a straight line with slope $-1/X_l$ and intercept $-1/X_l \cdot [ln(X_l u)]$.

. Figure 5.9 shows the oxide film thickness data replotted in the form $1/d$ (i.e. $1/x$) versus $ln(L/d^2)$ (i.e. $ln(t/x^2)$). From the figure, it is evident that the data fall on a straight line as predicted by theory. The solid lines in Figure 5.9 represent the best-fit lines obtained by linear least squares regression. These regressions yielded reasonably good correlation coefficients (≥ 0.86) thus indicating that no obvious tendency toward curvature exists. This then implies that the constant τ in equation (5.5) is very small and can be neglected [5.26]. The parameters of the theory, u and X_l , were calculated from the best-fit slopes and intercepts and are presented in Table 5.3. Table 5.3 also contains the parameters for the oxidation of pure Mg surfaces obtained in an identical fashion.

Table 5.3: Values of u and X_l obtained by linear least-squares regression of oxidation data.

	u (ML/L)	X_l (ML)	Correlation Coefficient
Mg-8.5Al	5.2e-25	89	.86
Mg-3.0Al	3.9e-14	140	.95
Pure Mg	5.6e-11	370	.96

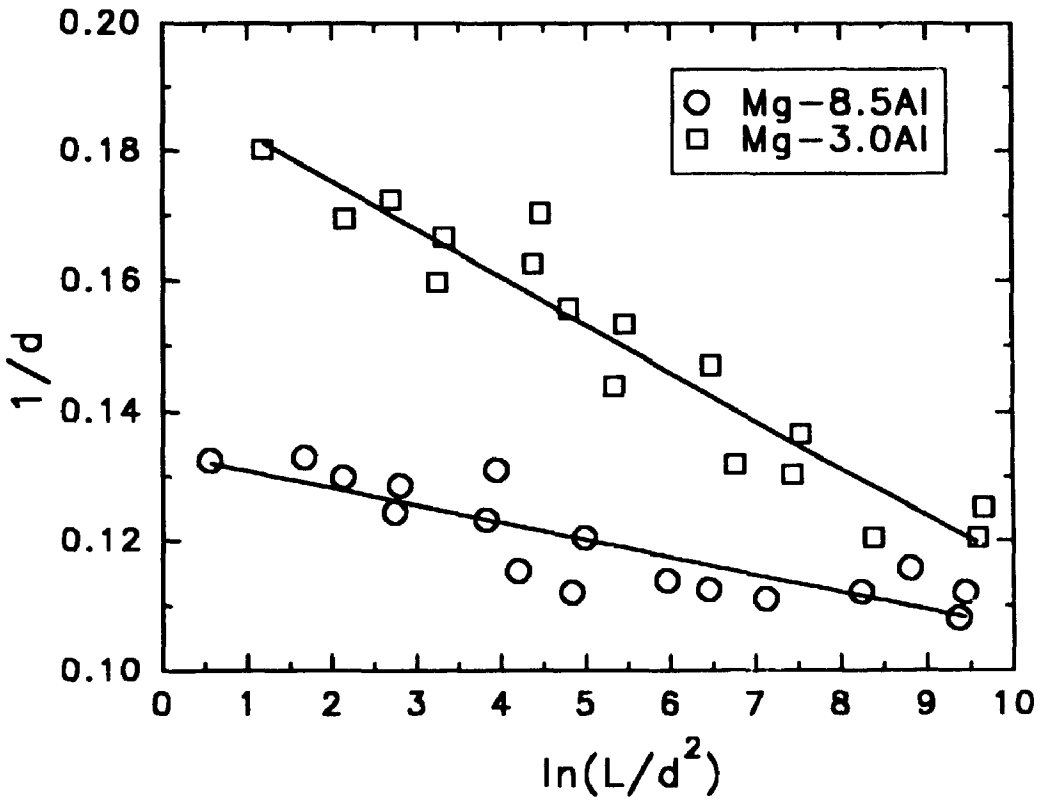

Figure 5.9: Oxide film thickness data re-plotted in the form of equation (5.5) [5.26]. The parameters of the theory, u and X_I, are calculated from the best-fit slopes and intercepts and are included in Table 5.3.

These parameters can now be used to estimate actual physical quantities. For example, using equation (5.6) we can write:

$$\frac{u_{Mg}}{u_{MgAl}} = \frac{N_{Mg}\Omega_{Mg}\nu_{Mg}\exp(-W_{Mg}/kT)}{N_{MgAl}\Omega_{MgAl}\nu_{MgAl}\exp(-W_{MgAl}/kT)} \tag{5.8}$$

Now, if it is assumed that $N_{Mg} \approx N_{MgAl}$, $\Omega_{Mg} \approx \Omega_{MgAl}$, and $\nu_{Mg} = \nu_{MgAl}$ then

$$\frac{u_{Mg}}{u_{MgAl}} = \exp[\frac{(W_{MgAl}-W_{Mg})}{kT}] \tag{5.9}$$

Equation (5.9) can be used with the estimates of u contained in Table 5.3 to estimate the change in activation energy for defect motion (i.e. oxidation) due to the presence of Al in Mg. At room temperature, we find:

$$W_{Mg\text{-}3.0Al} \approx W_{Mg} + 0.3\ eV \tag{5.10}$$

$$W_{Mg\text{-}8.5Al} \approx W_{Mg} + 1.3\ eV \tag{5.11}$$

It should be noted that the presence of Al may also be expected to decrease N, the number of potentially mobile defects at the interface, by a small amount. The estimated differences in the activation energies presented in equations (5.10) and (5.11) should

therefore be considered upper limits. These results nevertheless suggest that the presence of Al as a bulk alloying addition to Mg leads to an increase in the activation energy required for defect motion through the oxide films. In order to define absolute values of W, the above analyses would have to be repeated at several temperatures and the corresponding Arrhenius relationships determined. Although this was not performed here, W_{Mg} can be *estimated* by making use of the data of Schwoebel [5.7] for the oxidation of Mg(0001) at 673 K. In this work, relatively thick oxide films were formed by reaction with low partial pressures of pure O_2. For thick films ($x \gg X_1$), equation (5.3) reduces to:

$$\frac{dx}{dt} = 2u \frac{X_1}{x} \tag{5.12}$$

which yields the well-known parabolic rate law:

$$(\frac{ut}{X_1}) + C = \frac{1}{4}(\frac{x}{X_1})^2 \tag{5.13}$$

Schwoebel's original data were re-fitted to equation (5.13) using non-linear regression (not shown) and yielded an estimate for u_{Mg} at 673 K of $\approx$ 0.44 nm/sec $\approx$ 2.1 ML/L at 1.3×10^{-4} Pa. This was then compared to the value of u_{Mg} at 298 K determined above (5.6×10^{-11} ML/L) and provided an estimate of the activation energy for the

oxidation of pure Mg of $W_{Mg} \approx 1.8$ eV. This value closely matches that reported by Schwoebel (viz. 39 kcal/mol $\approx$ 1.7 eV) and is therefore deemed to be reasonable. It is apparent, therefore, that the presence of Al causes a sizeable *relative* increase in the activation energy for oxide growth on Mg surfaces. Using equations (5.10) and (5.11), we estimate the appropriate activation energies to be $W_{Mg\text{-}3.0Al} \approx 2.1$ eV and $W_{Mg\text{-}8.5Al} \approx$ 3.1 eV. These estimates are in good agreement with those reported by Leontis and Rhines [5.6] for the linear oxidation of several binary Mg-Al alloys (Table 5.4).

Table 5.4: Activation energies for the linear oxidation of several binary Mg-Al alloys (in wt%) [5.6].

	Mg-1.8Al	Mg-3.8Al	Mg-7.2Al	Mg-9.1Al
W_{MgAl} (eV)	1.86	1.68	2.38	3.24

The fact that Al additions resulted in increased activation energies and thus reduced logarithmic oxide growth rates is not surprising in view of the bulk oxide thickening mechanism of magnesium. It was proposed in Chapter 3 that the bulk thickening process is controlled by the transport of metal cations from the metal/oxide interface to the oxide/gas interface. Since MgO is classified as an n-type oxide semiconductor (metal excess) [5.27], the addition of small amounts of a trivalent impurity such as Al would, as a consequence of the law of mass action, decrease the equilibrium concentration of defects (i.e. Mg interstitials) and therefore decrease the rate of oxide film growth.

Although the theory of defect equilibria in oxides undoubtedly requires some modification when applied to thin films, the basic conclusions regarding the effects of small impurity additions of differing valencies, which would affect the overall defect concentration, should still be valid. It should also be noted that the above results are supported by the TEM results of Hales et al. [5.28]. These authors studied dislocation loop growth in Mg foils as a function of small alloying additions and air pressure. The growth of loops, which was due to metal cation movement through the oxide resulting in a counterflow of vacancies into the substrate, was found to be much slower on Mg-0.5at% Al than on pure Mg. It was therefore concluded that the presence of Al reduced the equilibrium concentration of metal cations in the oxide film and thus decreased the rate of vacancy injection into the metal.

Finally, it is interesting to note that the relative concentration of Al^{3+} in the oxide films was observed to *decrease* as the oxidation proceeded. Figure 5.10 shows the evolution of the Al^{3+}/Mg^{2+} XPS intensity ratio for increasing exposures to D_2O on the Mg-8.5Al surface. A similar observation was made by Hayden et al [5.8] for the oxidation of Mg-1.0Al and Mg-6.0Al surfaces by oxygen at room temperature. This phenomenon can again be understood with reference to the Cabrera-Mott theory outlined above. As stated, it is the field-dependent transport of ions that governs the oxidation process. The role of the electric field is therefore to lower the activation energy for ion movement, W, by an amount equal to qaE. The ion flux through the oxide film, n, can then be represented by:

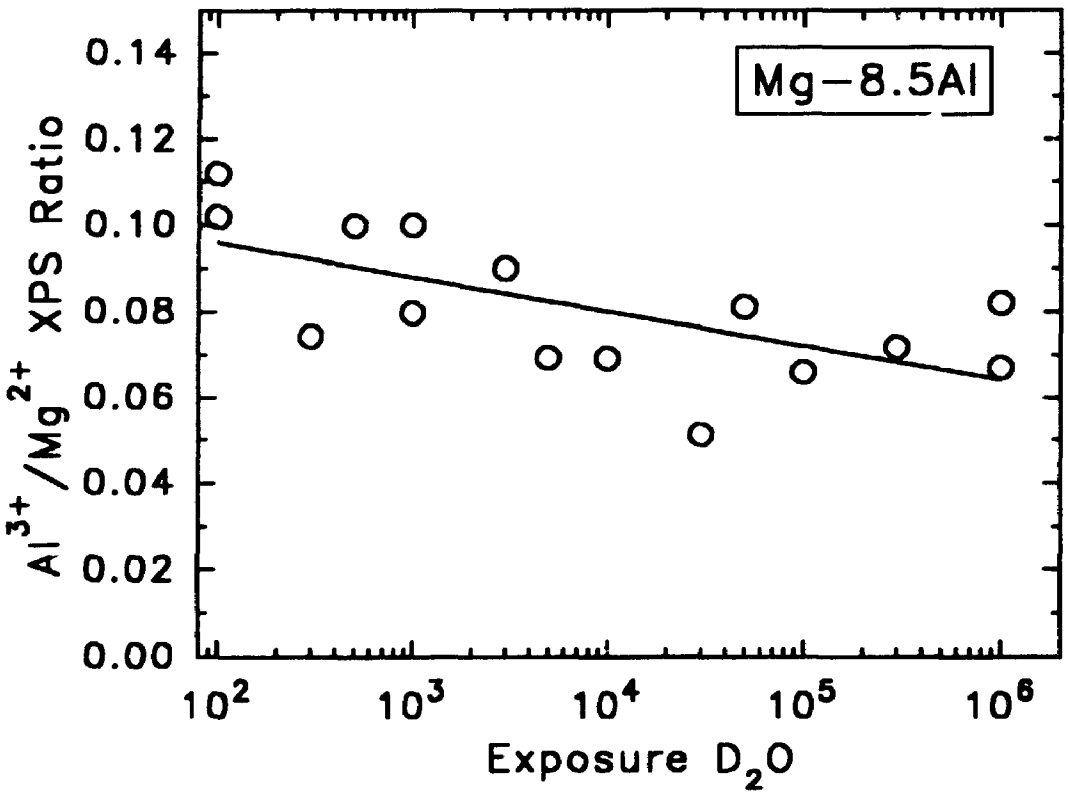

Figure 5.10: The evolution of the Al^{3+}/Mg^{2+} XPS intensity ratio for increasing exposures to D_2O on the Mg-8.5Al surface.

$$n = n^{o} \exp[-\frac{(W-qaE)}{kT}] \qquad (5.14)$$

where n^{o} is the concentration of ions available to move from the interface. For the case of ion movement through the oxide films formed on Mg-Al alloys, two identical equations of the form of equation (5.14) can be written for the movement of Mg^{2+} and Al^{3+} ions, n_{Mg} and n_{Al}. If it is now recognised that the activation energy for the diffusion of Mg^{2+} is lower than for Al^{3+} in the oxide film [5.29] *and* that the concentration of available Mg^{2+} ions at the interface, n^{o}_{Mg}, is greater than that for Al^{3+} ions, n^{o}_{Al}, then it is clear from the form of equation (5.14) that a crossover in n_{Mg} and n_{Al} can occur as a function of field strength. Figure 5.11 shows the results of a simulation of equation (5.14) for n_{Mg} and n_{Al} when $W_{Mg} < W_{Al}$ and $n^{o}_{Mg} > n^{o}_{Al}$. From the figure, it is clear that as the oxide film thickens (i.e. as the electric field strength decreases), the relative flux of Al^{3+} ions through the film decreases. This then provides further evidence that the Cabrera-Mott oxidation mechanism is operative on Mg-Al alloy surfaces.

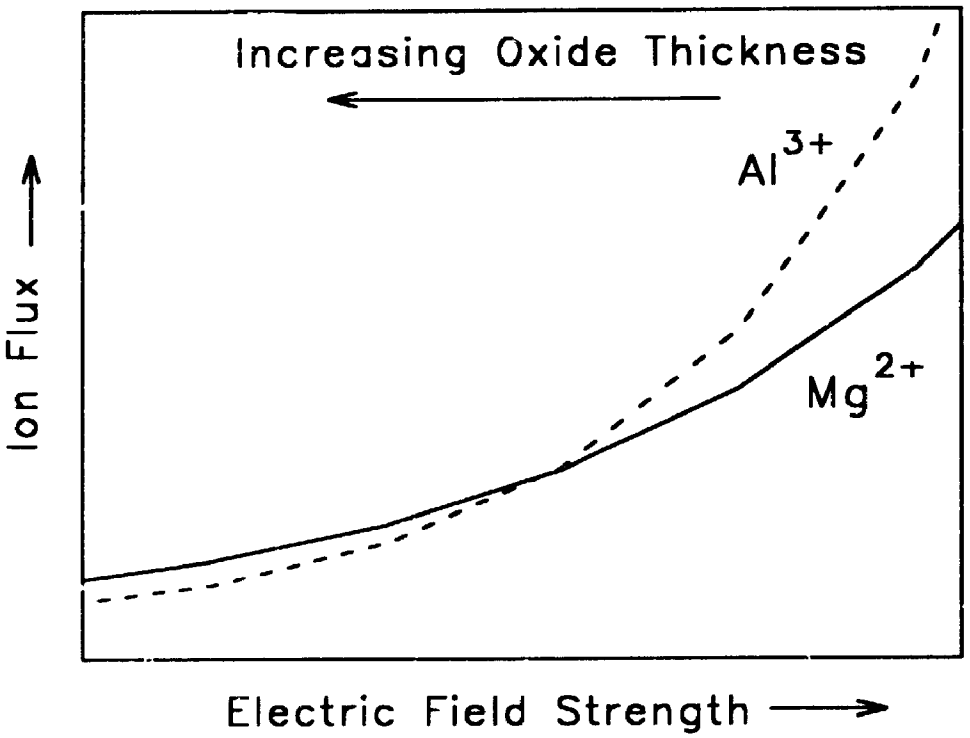

Figure 5.11: Results of a simulation using equation (5.14) to estimate the relative flux of Mg^{2+} and Al^{3+} ions through an oxide film of varying electric field strength.

5.4. Conclusions

Several conclusions can be drawn from this work:

(1) The room temperature interaction of water vapour with Mg-Al alloy surfaces results in a three-stage oxidation behaviour, similar to that observed on pure magnesium: dissociative chemisorption during low exposures (up to $\approx$ 0.5 L); oxide nucleation and island growth during intermediate exposures ($\approx$ 0.5L to 3.0L); and slow, diffusion-controlled bulk oxide thickening following coalescence of the oxide islands;

(2) The adsorption of oxygen occurs simultaneously on both magnesium and aluminum atoms present on the surface. Modelling results suggest that the rate of oxide nucleation and growth is enhanced on Mg-Al surfaces compared to on pure Mg surfaces, especially at higher Al contents. The nucleation and growth of MgO islands appears to occur preferentially above Mg-rich regions on the surface, suggesting that the two-phase nature of the alloys may play a significant role in the early stages of oxide formation.

(3) At l arger exposures, Al^{3+} cations are incorporated into the growing oxide film, resulting in an increased activation energy for ion movement and a pronounced decrease in the rate of bulk thickening. The surface concentration of aluminum is observed to decrease slowly as the film thickens. The bulk thickening regime can be adequately described in terms of the Cabrera-Mott theory of low-temperature oxidation.

References

[5.1] P.A. Thiel and T.E. Madey, Surf. Sci. Rep. 7 (1987) 211.

[5.2] D.P. Whittle, in: R.A. Rapp (Ed.), High Temperature Corrosion, NACE-6, (San Diego, 1983) p.171.

[5.3] G.C. Wood and F.H. Stott, Mater. Sci. Technol. 3 (1987) 519.

[5.4] J.D. Hanawalt, C.E. Nelson and J.A. Peloubet, Trans. AIME 147 (1942) 273.

[5.5] G.L. Makar, J. Kruger and A. Joshi, in: H. Paris and W. Hunt (Eds.), Proc. Advances in Magnesium Alloys and Composites, (TMS, Phoenix, 1988) p.105.

[5.6] T.E. Leontis and F.N. Rhines, Trans. AIME 166 (1946) 265.

[5.7] R. Schwoebel, J. Appl. Phys. 34 (1963) 2776.

[5.8] B.E. Hayden, D.F. Klemperer, G.C. Allen and P.M. Tucker, Le Vide, les couches minces, 201 (1980) 453.

[5.9] G.C. Allen, P.M. Tucker, B.E. Hayden and D.F. Klemperer, Surf. Sci. 102 (1981) 207.

[5.10] J. Kruger, G.G. Long, Z. Zhang and D.K. Tanaka, Corros. Sci. 31 (1990) 111.

[5.11] N. Shamir, M.H. Mintz, J.Bloch and U. Atzmony, J. Less Common Met. 92 (1983) 253.

[5.12] A. Hoffman, Ts. Maniv and M. Folman, Surf. Sci. 182 (1987) 56.

[5.13] D. Briggs and M.P. Seah, Practical Surface Analysis, Volume 1, 2nd Edition (J. Wiley and Sons, Chichester, 1990).

[5.14] J.H. Scofield, J. Electron. Spectrosc. Relat. Phenom. 8 (1976) 129.

[5.15] G.V. Raynor, The Physical Metallurgy of Magnesium and Its Alloys (Permagon Press, New York, 1959).

[5.16] P. Braun, M. Arias, H. Störi and F.P. Viehböck, Surf. Sci. 126 (1983) 714.

[5.17] A.P. Janssen, R.C. Schoonmaker, J.A.D. Mattew and A. Chambers, Solid State Commun. 14 (1974) 1263.

[5.18] F.J. Esposto, C.-S. Zhang and P.R. Norton, Surf. Sci., in press.

[5.19] C. Leygraf, C. Hultquist, S. Ekelund and J.C. Eriksson, Surf. Sci. 46 (1974) 157.

[5.20] S. Tanuma, C.J. Powell and D.R. Penn, Surf. Interface Anal. 17 (1991) 911.

[5.21] S.P. Kowalczyk, F.R. McFeely, L. Ley, V.T. Gritsyna and D.A. Shirley, Solid State Commun. 23 (1977) 161.

[5.22] A. Barrie, Chem. Phys. Lett. 19 (1973) 109.

[5.23] S.A. Flodström, C.W.B. Martinson, G. Kalkoffen and C. Kunz, Mater. Sci. Eng. 42 (1980) 31.

[5.24] N. Cabrera and N.F. Mott, Rep. Prog. Phys. 12 (1948) 163.

[5.25] F.P. Fehlner, Low Temperature Oxidation: The Role of Vitreous Oxides (Wiley, New York, 1986).

[5.26] R. Ghez, J. Chem. Phys. 58 (1973) 1838.

[5.27] O. Kubachewski and B.E. Hopkins, Oxidation of Metals and Alloys, 2nd Ed. (Butterworths, London, 1962).

[5.28] R. Hales, P.S. Dobson and R.E. Smallman, Met. Sci. J. 2 (1968) 224.

[5.29] C. Lea and C. Molinari, J. Mater. Sci. 19 (1984) 2336.

CHAPTER 6

THE INITIAL INTERACTION OF WATER VAPOUR WITH DILUTE Mg-Fe ALLOY SURFACES

6.1 Introduction

The enhanced corrosion of magnesium-base alloys caused by trace amounts of noble metal impurities is well-known [6.1-6.4]. Of these, iron is often the most troublesome since it is introduced to the melt from steel pots and casting moulds and is present as an impurity in the alloying additions. When the iron concentration in magnesium exceeds the "tolerance limit" of approximately 170 parts per million by weight (wt ppm), the rate of corrosive attack in chloride-containing aqueous solutions increases dramatically [6.1]. The precise role that iron plays in the corrosion process is, however, unclear. In this chapter, the initial oxide formation occurring on the surfaces of magnesium specimens deliberately contaminated with very low (ppm) levels of iron has been studied by AES, XPS and SIMS. An understanding of the effect of iron on the nature of the oxide films formed on magnesium should be helpful in gaining a better understanding of the effect of iron on the corrosion properties of magnesium.

There are no specific theories which suggest why iron causes enhanced corrosion in magnesium. Iron is, however, of unfavourable size factor with magnesium [6.5] and consequently no appreciable solid solution formation is observed. The solubility limit of iron in magnesium has in fact recently been re-evaluated by Mitrovic-Scepanovic et

al. [6.6] using electronprobe microanalysis (EPMA) and was found to be approximately 55 ppm by weight at 673 K. Thus, if the iron content of magnesium or magnesium alloys exceeds this value, the microstructure is expected to consist of a dispersion of iron-rich precipitates throughout the magnesium matrix. Since iron and magnesium are widely separated on the galvanic series [6.7], magnesium will dissolve at the expense of iron if the two metals are coupled in an electrolyte. The deleterious effect of iron on magnesium corrosion may therefore be due to the microgalvanic effects induced by the inhomogeneous distribution of iron-rich particles in the magnesium matrix. The effect of the level and distribution of iron on the aqueous corrosion properties of magnesium is currently being investigated at the Metals Technology Laboratories (MTL) of the Canada Centre for Mineral and Energy Technology (CANMET), Ottawa, Ontario.

The influence of iron additions on the growth and nature of the oxide films formed on magnesium in gaseous environments has received very little attention. To the best of our knowledge, the only existing report is from the 1960's. Schwoebel [6.8] studied oxide growth on Mg(0001) single crystals in pure O_2 at 673 K using a quartz microbalance and found that the addition of 0.017 at% Fe ($\approx$ 400 wt ppm Fe) resulted in a small decrease in the parabolic growth rate. Under these experimental conditions, however, the very early stages of oxide formation, up to a few monolayers of oxide, could not be characterised.

In the present work, the adsorption of water vapour and subsequent oxide film growth on pure magnesium containing very low concentrations of iron (120 wt ppm to 700 wt ppm) has been shown to be retarded during the very early stages. The growth

rate at longer exposures, during the bulk thickening regime, was found to be unaffected by the iron content of the substrate. Segregation of iron atoms into the oxide film has, however, been detected by static secondary ion mass spectrometry (SSIMS). Finally, the saturated oxide films formed on iron-containing magnesium specimens have been shown by XPS to be more "defective" than those formed on pure magnesium surfaces.

6.2 Experimental

Three binary Mg-Fe alloys containing nominally 120 wt ppm Fe (50 ppma), 350 wt ppm Fe (150 ppma) and 700 wt ppm Fe (300 ppma) were used throughout the study. The specimens were produced at the [illegible]dry facilities of MTL-CANMET. Iron was introduced in the form of powdered Fe_2O_3 mixed with a chloride flux into a high-purity magnesium melting stock ($\approx$ 9 wt ppm Fe, section 2.3) which had been heated to 1033 K in an induction furnace [6.6]. The ingots were subsequently rolled at 673 K, cut into strips and annealed at 673 K in N_2 for one hour. This heat treatment was sufficient to produce a fully recrystallised structure. Table 6.1 shows the major impurities (in parts per million by weight), determined by EPMA [6.6].

Table 6.1: Major impurities in Mg-Fe specimens (wt ppm) .

	Al	Zn	Mn	Fe	O	Ni	Cu	Si
Mg-120Fe	52	37	32	120	4	5	7	30
Mg-350Fe	53	37	35	345	4	6	7	30
Mg-700Fe	60	39	30	710	4	7	6	10

Surfaces were prepared for oxygen uptake studies as described in section 2.3. Once again, no post-sputtering annealing stage was performed in order to avoid the possible segregation of the low-level iron impurities to the surface or to the grain boundaries. It was shown in Chapter 4 that the rate of oxygen uptake on magnesium surfaces is sensitive to the level of prior Ar^+ ion bombardment. The total ion dose was therefore purposefully kept low ($< \approx 5 \times 10^{16}$ ions/cm^2) and the uptake of oxygen was continuously checked against that on pure magnesium surfaces under exactly identical conditions. In this way, it was believed that reliable comparisons could be made between the rate of oxygen uptake on Mg-Fe surfaces and that on pure Mg surfaces.

The clean surfaces were exposed in vacuum to calibrated doses of deuterated water vapour at room temperature for exposures up to 1×10^6 L. Auger and XPS spectra of the clean and water-dosed surfaces were then obtained using the same experimental conditions as outlined in Chapters 3 to 5. Once again, grains which exhibited very dark secondary electron contrast were chosen for detailed analysis. Grains of similar contrast levels on pure Mg were found to have surface normals very near the basal Mg(0001) pole in electron back scattering diffraction patterns (EBSDP's) (section 2.4).

A Cameca IMS-3f ion microscope was used to examine the distribution of iron-rich precipitates in the specimens, as described in section 2.6.4. The usefulness of SIMS imaging results from lateral resolution limits of approximately 0.5 μm in the direct ion imaging mode [6.9]. Static secondary ion mass spectrometry (SSIMS) was used to search for the presence of iron atoms in the thin oxide films formed on the surfaces of

the specimens. A modified Vacuum Generators (VG) ZAB-2F spectrometer was used for this purpose (section 2.6.4).

6.3 Results and Discussion

Figure 6.1 shows the evolution of the ratio of the peak-to-peak amplitude of the O(KLL) and Mg(LVV) AES signals as a function of D_2O exposure for pure magnesium and iron-containing magnesium surfaces. The various specimens were loaded simultaneously into the Auger spectrometer and were given identical low-dose ion-bombardment cleaning treatments in order to minimise ion-induced effects (see above). The vertical error bars in Figure 6.1 represent the standard error calculated from at least three, and in most cases five, separate exposures on different grains showing similar contrast levels for each alloy. In most cases, the error bars are buried within the symbols. The inset shows the data obtained for the low exposure range re-plotted on an expanded linear scale. From the figure it is clear that the presence of very low levels of iron in pure magnesium results in a measurable decrease in the rate of oxygen uptake during short exposures to water vapour. The oxygen uptake curve for the iron-containing specimens lies below that for pure magnesium for exposures ranging from $\approx$ 0.15 to 20 L. In addition, it is noteworthy that the passivating effect of iron does not appear to be a function of the iron level itself. The data points for the various iron-containing specimens very nearly overlap each other. This may be due to the fact that the solubility limit for iron in magnesium was exceeded for each alloy (see below).

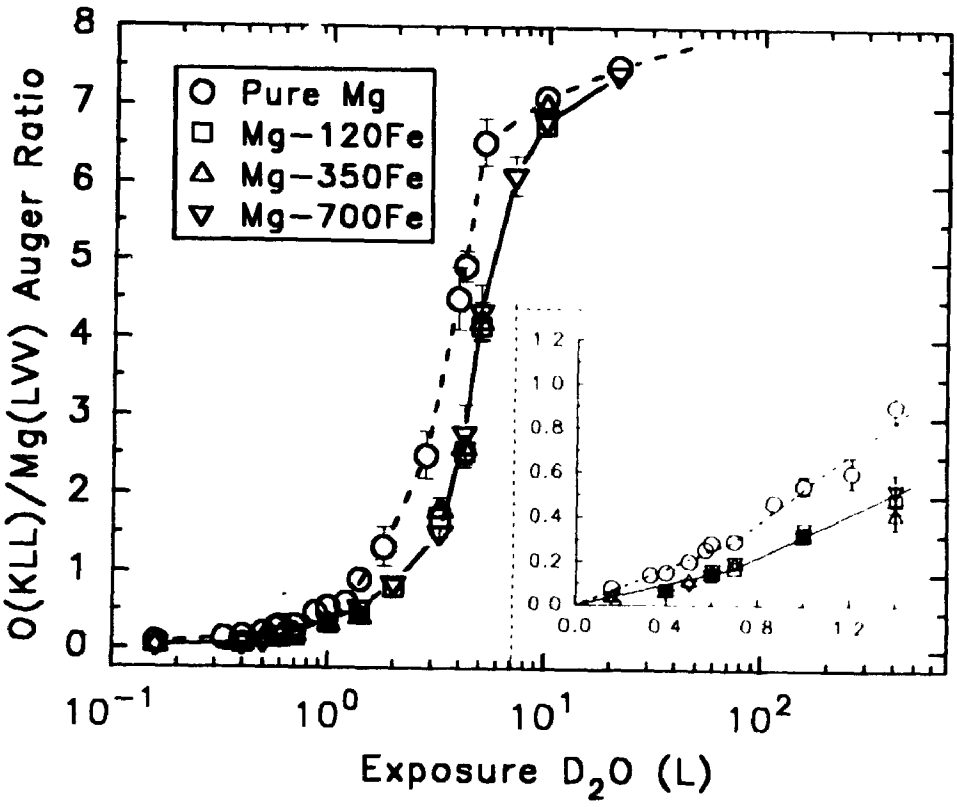

Figure 6.1: The evolution of the ratio of the peak-to-peak amplitude of the O(KLL) and Mg(LVV) AES signals as a function of D_2O exposure for pure magnesium and Mg-Fe surfaces. The error bars represent the standard error calculated for at least three separate exposures on each specimen. If the error bars do not appear, then they are buried within the symbols.

It was established in Chapter 3 that the initial interaction of water vapour with magnesium surfaces results in a three-stage oxidation behaviour: chemisorption; oxide nucleation and growth; and bulk oxide thickening. The breaks in the curves in Figure 6.1 at ≈ 0.7 L (inset) and ≈ 5 L exposure are thus consistent with the modelling results presented in Chapter 3, viz. chemisorption until approximately 0.7 L followed by oxide nucleation and growth by islands until coalescence at approximately 5 L exposure. It is apparent from Figure 6.1 that the rate of oxygen uptake is slower on the iron-containing surfaces during both the chemisorption and the oxide nucleation and growth regimes. The mechanism for this effect is not unambiguous, but it may result from small changes in the binding of the water molecule to the surface of the iron-containing specimens. This possibility is discussed below. Finally, at exposures exceeding approximately 10 L D_2O, corresponding to the beginning of the bulk thickening regime of the oxidation process, the oxygen uptake curves for pure magnesium and iron-containing magnesium surfaces coincide. The effect of iron impurities on the bulk thickening stage of magnesium oxidation is discussed in more detail later in this chapter.

The adsorption and reactivity of various molecules on metal surfaces is known to be significantly influenced by the presence of low-level impurities [6.10-6.12]. To date, most of the attention has been focussed primarily on the promotion and poisoning effects of coadsorbates observed during catalytic reactions. In general, electronegative and electropositive impurities are found to affect adsorption properties in different ways. For example, Nørskov et al. [6.10] used effective medium theory to show that electronegative coadsorbates (impurities) serve to deplete metal states near the Fermi level, thus

raising the *local* work function of the surface and hindering the dissociative adsorption of simple molecules such as CO and O_2. Electropositive impurities were shown to have the oppositive effect. For polar molecules such as H_2O, the situation is somewhat more complex, but can still be related to electrostatic effects [6.12].

Iron is expected to behave as an electronegative impurity in magnesium. For example, Guenzburger and Ellis [6.13] performed first principles electronic structure calculations for embedded clusters representing an Fe impurity in alkaline earth hosts and found that the Mullikan charge on the Fe impurity in Mg was negative. This is consistent with the fact that the electronegativity of Fe (1.8 eV) exceeds that of Mg (1.2 eV); electron transfer from Mg to Fe is therefore expected. The result of this electrostatic interaction is that the acidity (electron deficiency) of the Mg atoms in close proximity to the impurity Fe atoms is increased (i.e. the *local* work function of the surface increases). Since the water molecule initially binds through the lone-pair electrons of the oxygen atom (i.e. the lone-pairs act as electron donors) [6.12], the increased acidity induced by the iron impurity should thereby increase the ability of the nearest neighbour magnesium atoms to accept electrons from the H_2O molecule (ligand). This increased stability (binding) of the water molecules at the electron-poor Mg sites near the Fe impurities may then act to limit their mobility over the surface, thus preventing them from easily reaching vacant sites suitable for dissociation. Similarly, one would expect that the electronic effects which stabilize adsorbed water would destabilize adsorbed oxygen and hydroxyl [6.12]. The presence of the electronegative Fe impurity should therefore act to decrease the binding energy of adsorbed oxygen and

hydroxyls on magnesium surfaces, thus limiting the dissociative adsorption of water and subsequent oxygen uptake.

The stronger binding of the water molecule to the iron-containing surfaces can also result in a retardation of oxide nucleation. If the nucleation process is once again envisaged as a "place exchange" process (Chapter 4) [6.14], then, in order for oxide nucleation to proceed, there must be "switch-on" of a repulsive interaction between oxygen in the chemisorbed state and an attractive interaction between oxygen in the oxidised state [6.15,6.16]. The increased binding of the water molecules to the electron-poor Mg sites could conceivably delay this transformation.

The fact that the influence of iron on the uptake of oxygen on magnesium surfaces was not found to be a clear function of iron concentration (Figure 6.1) may be due to the fact that the solubility limit of iron was exceeded in each specimen. Figure 6.2 shows representative two-dimensional SIMS images of the secondary $^{54}Fe^{+}$ and $^{56}Fe^{+}$ ions collected from (a) Mg-120Fe, (b) Mg-350Fe and (c) Mg-700Fe specimens. The images can be considered to be representative of the specimen bulk. From the figure, it is evident that all of the iron-containing specimens exhibit an inhomogeneous distribution of iron-rich precipitates in the magnesium matrix, ranging from $\approx$ 1 μm to $\approx$ 10 μm in size. The larger features in Figure 6.2 likely represent clusters of smaller precipitates. Identical specimens were examined by transmission electron microscopy (TEM) at MTL-CANMET and the results are presented elsewhere [6.6, 6.17]. In this work, all iron-containing specimens were found to contain iron-rich inclusions, often in the form of clusters, with diameters ranging from $\approx$ 0.3 μm to $\approx$ 3 μm. In addition, smaller iron-

Figure 6.2: Representative SIMS images of the $^{54}Fe^+$ and $^{56}Fe^+$ secondary ions collected from (a) Mg-120Fe, (b) Mg-350Fe and (c) Mg-700Fe specimens. The secondary ions were generated using a 100 nA, 17 keV O^- primary ion beam rastered over a 250 × 250 μm^2 area. No voltage offset was used in order to maximize the yield of secondary ions. Because of this, both the $^{54}Fe^+$ and $^{56}Fe^+$ signals were collected in order to confirm that no major molecular interference from $^{56}MgO_2^+$ was present. Similar images for both isotopes of iron verified this assertion. The imaged field is approximately 150 μm in diameter and the lateral resolution is approximately 1 μm.

5. Detailed XPS spectra of the oxide film show two distinct types of oxygen: one of these is assigned to oxygen atoms in normal MgO lattice positions; the other is ascribed to oxygen atoms in a "defective" chemical environment.

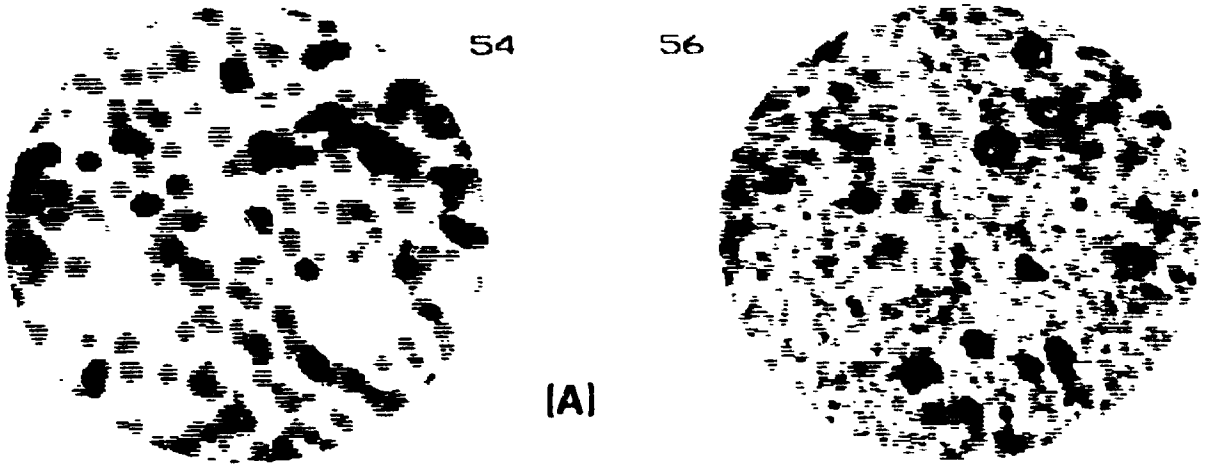
54
56
(A)

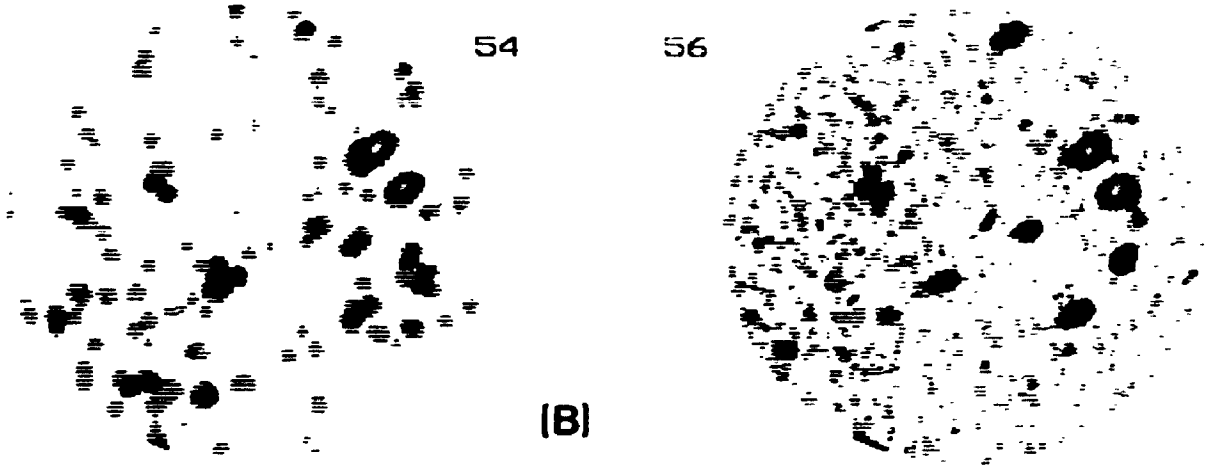
54
56
(B)

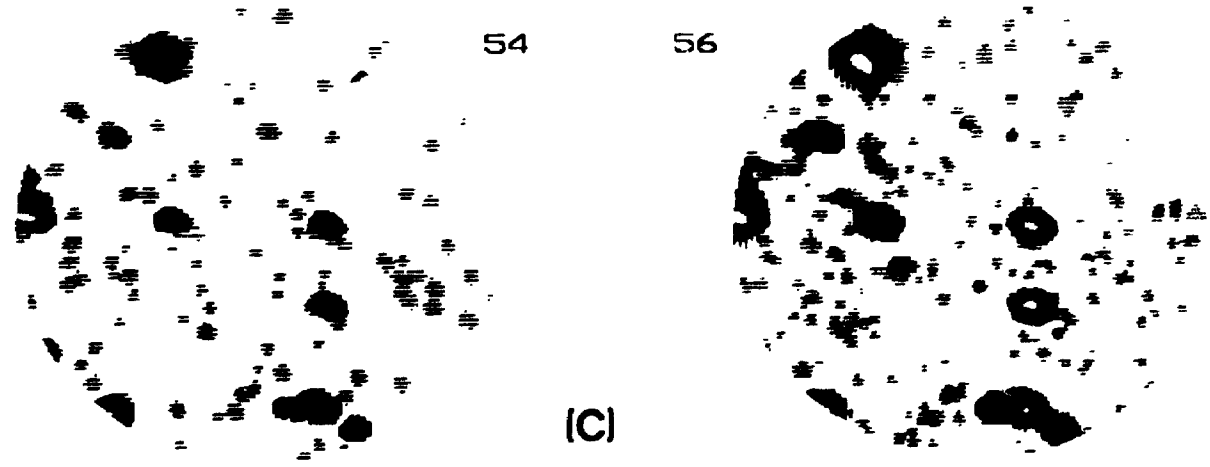
54
56
(C)

containing precipitates (diameters 200 to 300 nm) were observed. Energy dispersive X-ray analysis (EDX) and convergent beam electron diffraction (CBED) analysis suggested that the precipitates were composed mainly of iron containing $\approx$ 6 at% dissolved silicon. Pure iron was not observed as a second phase in any of the alloys studied. Iron-rich precipitates were rare in the high-purity magnesium specimens. The fact that all of the alloys showed a similar inhomogeneous distribution of iron and the oxygen uptake results showed no clear dependence on the iron concentration (Figure 6.1) seems to suggest that it is the inhomogeneous nature of the iron distribution that most strongly influences the oxidation process on magnesium. Experiments are planned to investigate the effect of iron distribution using specimens prepared by ion implantation of iron into high-purity magnesium. It is known that iron may be inserted into the magnesium lattice by ion implantation [6.18]. By comparing the effects of implanted iron in solid solution with iron present as solid inclusions, it is hoped that the role that iron impurities play in the oxidation processes on magnesium can be further elucidated.

In order to follow the oxidation process on Mg-Fe surfaces to much higher exposures, XPS was employed. This was once again possible because of the relatively long IMFP of the energetic photoelectrons as compared to the corresponding Auger electrons (Appendix A). The thickness of the oxide films formed at various total exposures was determined by measuring the intensity ratio of the oxidic (Mg^{2+}) to metallic (Mg^{o}) XPS signals, as described in Chapter 3. Figure 6.3 shows the oxide thickness as a function of D_2O exposure for the various iron-containing specimens. The solid line in Figure 6.3 represents the line of best fit obtained previously for pure

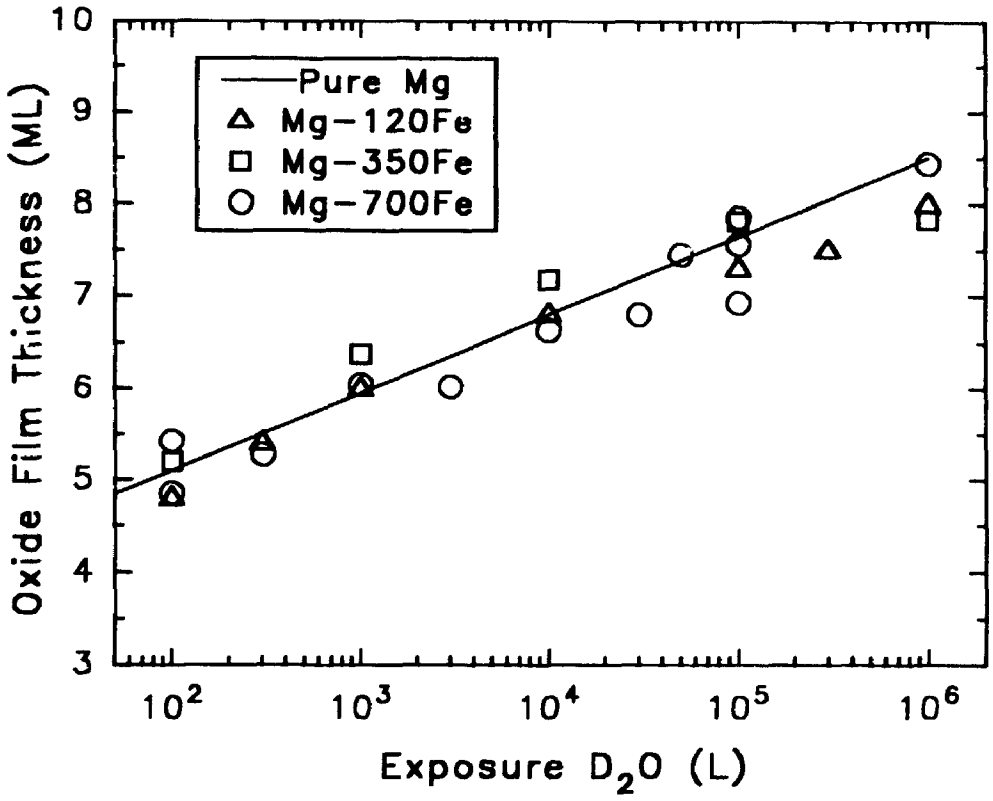

Figure 6.3: The growth of oxide during increased exposures to D_2O on Mg-Fe alloy surfaces monitored by XPS. The solid line represents the line of best fit obtained previously for pure magnesium surfaces (Chapter 3).

magnesium surfaces (Figure 3.6). From the figure, it is evident that the presence of very low levels of iron in magnesium does not influence the rate of bulk oxide thickening to any appreciable degree. The data points for the various alloys are scattered fairly uniformly about the line of best fit for the high-purity magnesium specimen.

Despite the fact that the rate of bulk oxide thickening was found to be little affected by the presence of iron in the magnesium substrate, subtle changes in the oxide film chemistry were in fact observed. It was established in Chapter 3 that the reaction of water vapour with pure magnesium surfaces results in the appearance of oxygen atoms in two distinct chemical environments within the thin oxide films that are formed. This conclusion was reached in part by a careful examination of the shape of the core-level O(1s) XPS line (Figure 3.8). The low binding energy (LBE) O(1s) component was assigned to oxygen atoms in a "normal" MgO lattice position, whereas the high binding energy (HBE) O(1s) component was assigned, at least in part, to oxygen atoms in a "defective" chemical environment. It was shown in Figure 3.8 that the ratio HBE/LBE increased with increasing exposures to D_2O during the bulk thickening regime, despite the fact that the relative hydrogen (deuterium) level in the film remained essentially constant during the same exposure range (Figure 3.10). The changes in the chemistry of the oxide films formed on iron-contaminated magnesium surfaces compared to pure magnesium surfaces were thus examined by monitoring the HBE/LBE O(1s) XPS ratio as a function of D_2O exposure. Figure 6.4 shows the evolution of this ratio for increasing exposures to D_2O on both pure magnesium and Mg-700Fe substrates. From

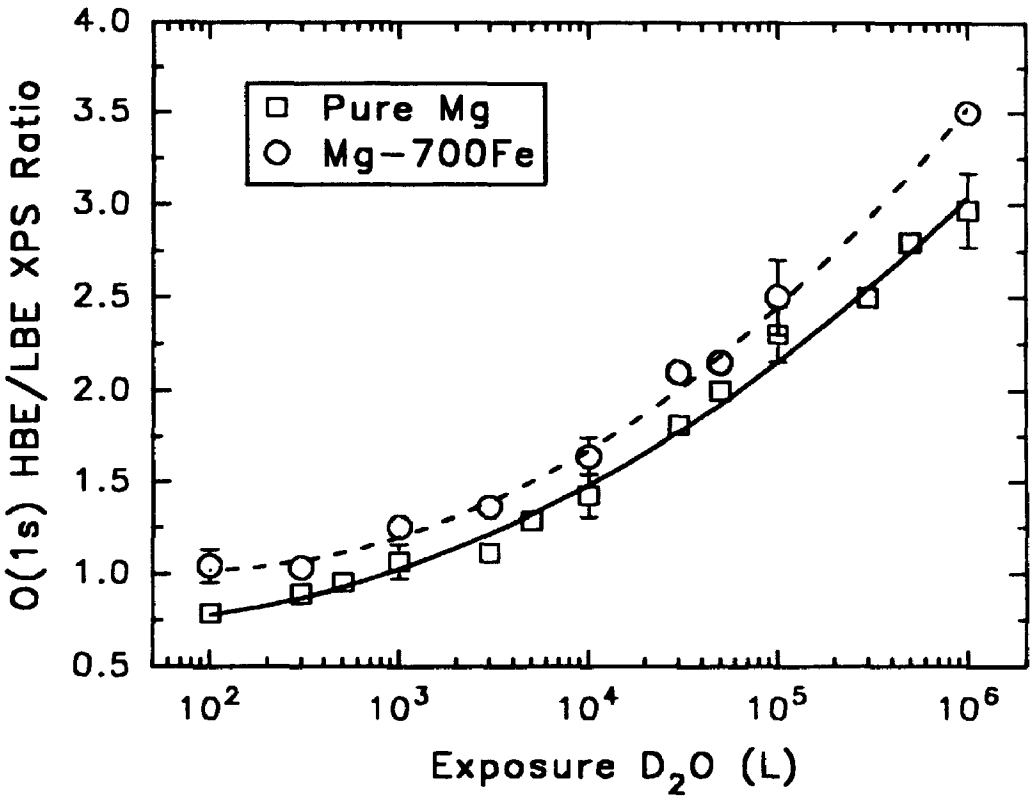

Figure 6.4: The evolution of the HBE/LBE O(1s) XPS ratio for increasing exposures to D_2O on pure magnesium and Mg-700Fe surfaces.

the figure it is clear that the HBE/LBE ratio remains higher on the Mg-700 Fe substrates across the entire bulk thickening exposure range.

Similar effects were observed for the saturated oxide films formed on the various alloy surfaces. Figure 6.5 shows the oxide film thicknesses and HBE/LBE O(1s) XPS ratios measured for the saturated oxide films on pure magnesium and the various Mg-Fe alloys. The films were formed by exposing the clean surfaces to $\approx$ 1000 L D_2O and then several minutes of air at atmospheric pressure. The error bars in the figure represent the standard error calculated from five separate experiments on each specimen. Because of the relatively large scatter in the data, an analysis of variance (ANOVA) on the HBE/LBE ratio with iron concentration as the between subject factor was calculated. In addition, since it was possible that the film thickness itself could influence the measured HBE/LBE ratio, the film thickness was subsequently added as a covariate in the statistical analysis (now an analysis of covariance (ANCOVA)). The results indicated that there was a significant main effect of iron concentration on HBE/LBE ratio ($\mathbf{F}(3,14)=2.9350$, $\mathbf{p}=0.03505$) but *no* significant effect of the covariate ($\mathbf{F}(1,13)=1.122$, $\mathbf{p}=0.309$). This then indicates that any small fluctuations in the oxide film thickness do *not* account for the differences observed for the HBE/LBE ratio with iron concentration. Increasing iron concentrations in the magnesium substrate therefore lead to a statistically significant increase in the measured HBE/LBE O(1s) XPS ratio in the saturated oxide films formed on the surfaces.

It is possible that the observed differences in the XPS spectra described above are due to the fact that iron atoms, though present in small relative amounts in the bulk, are

Figure 6.5: The oxide film thickness and HBE/LBE O(1s) XPS ratio measured for the saturated oxide films formed on pure magnesium and Mg-Fe alloy surfaces. The error bars represent the standard error calculated from five separate experiments on each specimen.

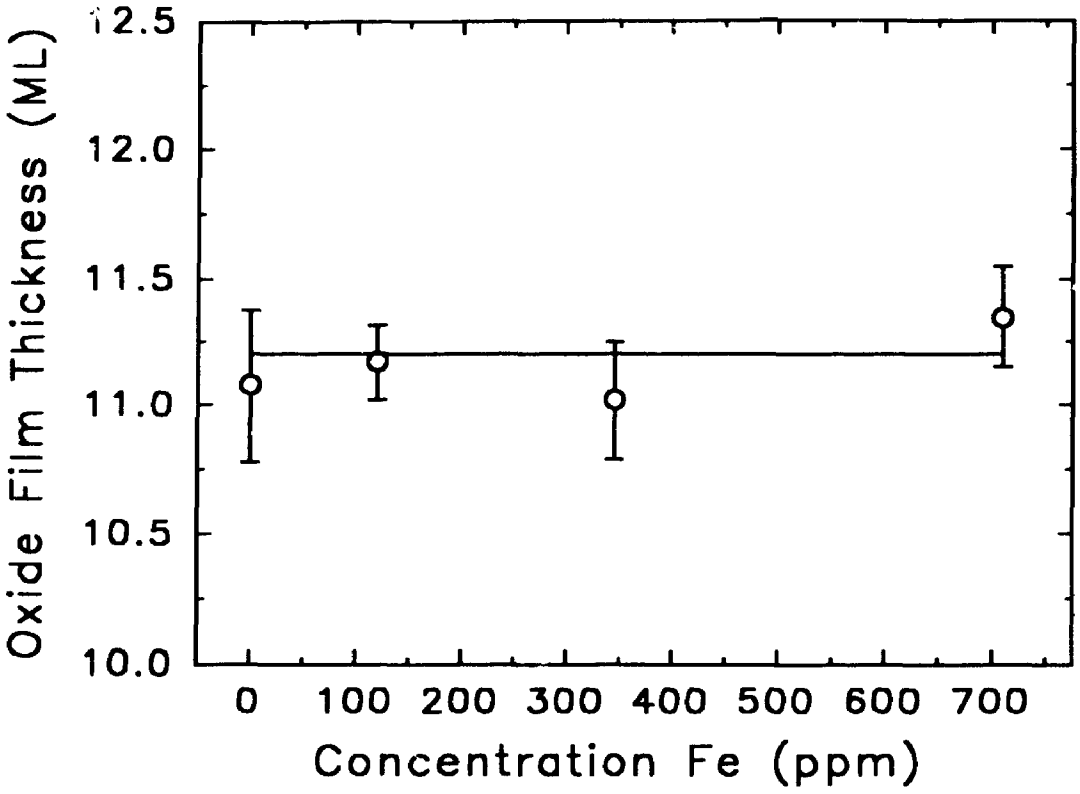
Oxide Film Thickness (ML)
12.5
12.0
11.5
11.0
10.5
10.0
0
100
200
300
400
500
600
700
Concentration Fe (ppm)

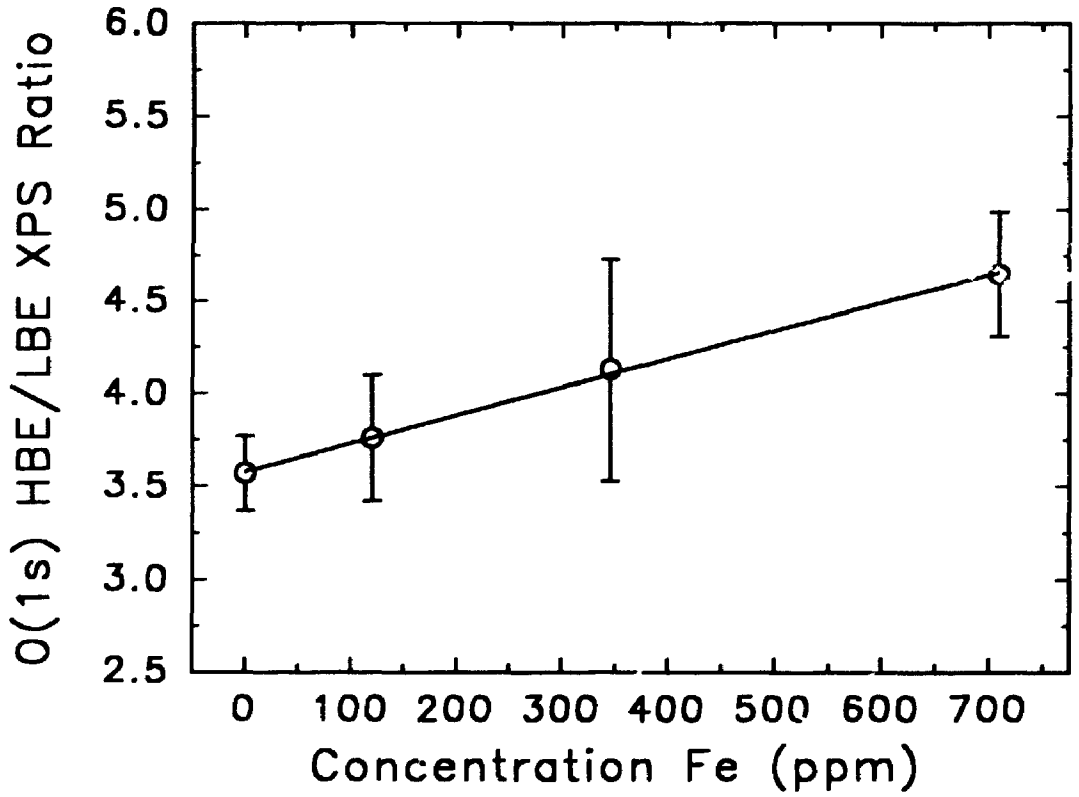
O(1s) HBE/LBE XPS Ratio
6.0
5.5
5.0
4.5
4.0
3.5
3.0
2.5
0
100
200
300
400
500
600
700
Concentration Fe (ppm)

segregated into the oxide film. It is known that iron ions can readily enter substitutional sites in MgO [6.19]. In order to examine this possiblility, static secondary ion mass spectrometry (SSIMS) was used to search for the presence of iron atoms in the thin oxide films formed on the Mg-Fe alloy surfaces. Figure 6.6 shows a representative SSIMS depth profile through the saturated oxide layer formed on the Mg-700Fe specimen. The profile was obtained using a 500 pA, 30 keV Ga^+ rastered primary ion beam, decelerated by 8 keV by passing through a secondary ion extraction field. The very low beam current permitted a sputter rate of approximately 1 nm/min to be achieved. Once again, no voltage offset was used in order to maximize the secondary ion counts. The nearly identical profiles for the $^{54}Fe^-$ and $^{56}Fe^-$ isotopes suggested that molecular interference from $^{56}MgO_2^-$ was minimal. From the figure, it is clear that the secondary ion signals from both isotopes of iron decay rapidly from the beginning of the profile and reach a steady state value, presumably indicative of the bulk, after approximately two to three minutes sputtering time (i.e. at a depth of $\approx$ 2 to 3 nm from the surface). This value corresponds roughly to the time at which the $^{16}O^-$ secondary ion signal falls to approximately one-half of its original value and is in excellent agreement with the oxide film thickness estimated by XPS ($\approx$ 11.3 ML MgO = 2.4 nm, Figure 6.5). It is evident, therefore, that the emission of secondary iron ions from the specimen is enhanced from within the thin oxide layer on the surface. The fact that the matrix ^{24}Mg secondary ion signal remains constant during this same range indicates that the enhancement of the iron signal is not due to an oxide-enhanced sputter yield [6.20]. It can be concluded, therefore, that iron atoms are segregated into the oxide film formed

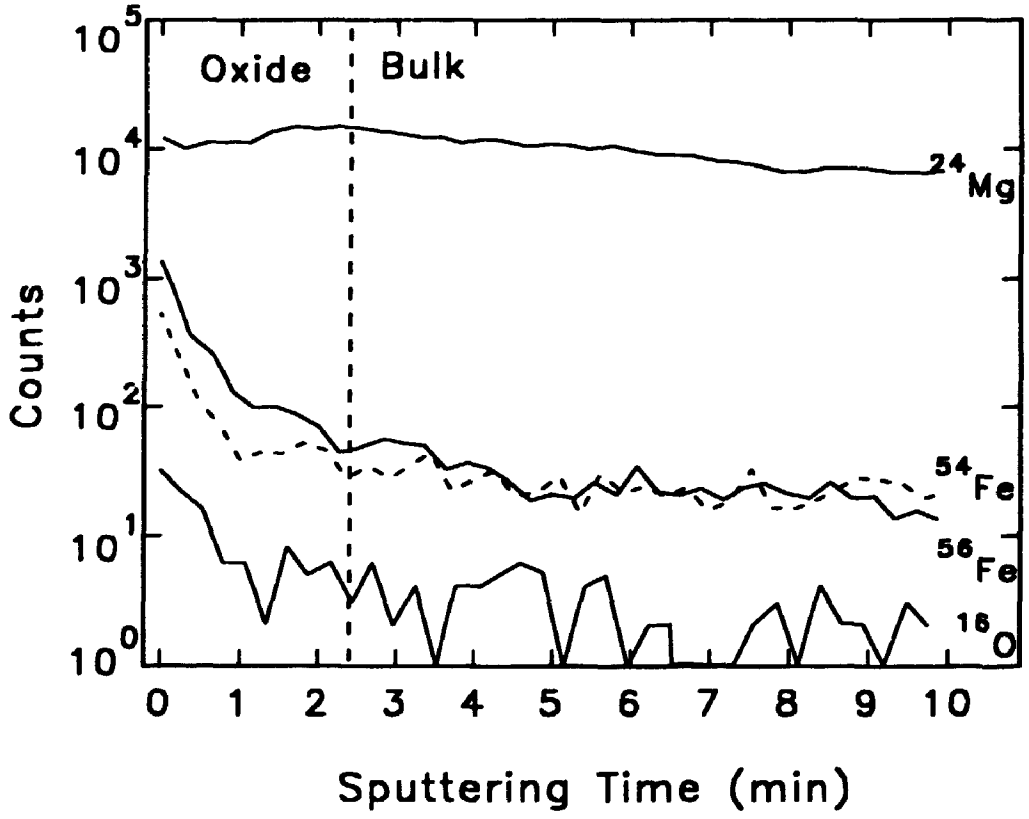

Figure 6.6: Representative SSIMS depth profile through the saturated oxide layer formed on the Mg-700Fe specimen. A sputter rate of approximately 1 nm/min was estimated.

on the iron-containing magnesium surfaces. It is worth noting here that iron was not detected on the surfaces of any of the specimens by either AES or XPS. This fact then necessarily places an upper limit on the degree of oxidation-induced segregation of iron from within the bulk. Because the detection limit of both AES and XPS is of the order of 1000 ppma [6.21], less than 1000 ppma Fe ($\approx$ 2300 wt ppm Fe) can have segregated to the surface.

The fact that the rate of bulk oxide thickening was not found to be modified by the iron content of the substrate (Figure 6.3) suggests that the iron atoms are present in the oxide films in a divalent (Fe^{2+}) oxidation state. If, conversely, significant numbers of monovalent or trivalent ions were present, then the equilibrium concentration of ionic defects (i.e. Mg interstitials) would be affected. The rate of bulk oxide thickening would therefore also be affected. In fact, the presence of trivalent Al^{3+} ions in the thin MgO films was shown in Chapter 5 to result in a significant reduction in the rate of bulk thickening. The fact that the HBE/LBE (O1s) XPS ratio was statistically higher for the oxide films formed on the iron-containing specimens, however, still suggests that the presence of iron in the films results in the formation of a more "defective" oxide layer. This is discussed below.

The increased HBE O(1s) contribution is consistent with increased numbers of oxygen atoms in a more positively charged oxidation state (i.e. the valence electron density around these oxygen atoms is decreased and hence the binding energy of the core-level O(1s) photoelectrons is increased). It is known that the presence of substitutional Fe^{2+} (or Fe^{3+}) impurity defects in MgO will result in an increased effective

charge transfer from oxygen to iron compared to a non-perturbed (defect-free) system. For example, Timmer and Borstel [6.22] performed theoretical calculations of the electronic structure of Ni, Co and Fe impurities in MgO using a Green's function method and found that Fe^{2+} and Fe^{3+} impurity defects cause the O(2p) valence states to be shifted to lower energies. The repulsive electron-electron interaction on the oxygen site is thus decreased and the oxygen anion becomes more positively charged. This is, of course, consistent with the observed increased HBE/LBE O(1s) XPS ratio. For the case of a Fe^{+} impurity defect, on the other hand, the effective charge transfer from oxygen to iron has just the opposite sign [6.22]. These considerations therefore indicate that the presence of iron impurities in the oxide films formed on magnesium result in small changes to the electronic structure of the oxide film itself. It is interesting to note that similarly small variations in the XPS spectra of the passive oxide films formed on nanocrystalline nickel substrates, compared to conventional polycrystalline nickel substrates, were recently shown to be accompanied by correspondingly large variations in the electrochemical breakdown of these same films [6.23]. The diminished stability of the films formed on the nanocrystalline substrates was attributed to a larger defect density in the oxides formed on these specimens. Studies are continuing in this laboratory using other alloy systems and various doped metal oxide single crystals in an effort to better understand the connection between the O(1s) XPS spectra and the defect nature of the oxide films.

6.4 Conclusions

The initial interaction of water vapour with dilute Mg-Fe alloy surfaces has been examined in detail using AES and XPS. The rate of oxygen uptake has been shown by AES to be retarded during the very early stages on iron-contaminated surfaces compared to on pure magnesium surfaces. It was postulated that this was due to small changes in the binding energy of water molecules on the surfaces of the Mg-Fe alloys. The influence of iron was not found to be a clear function of the iron concentration. This was likely due to the fact that the solubility limit of iron in magnesium ($\approx$ 55 wt ppm) was exceeded in each specimen. The inhomogeneous nature of the iron distribution in the magnesium matrix thus appears to be the main influencing factor in the oxidation process. The rate of bulk oxide thickening was shown by XPS to be unaffected by the iron content. Segregation of iron into the oxide films was, however, detected by SSIMS. Finally, the oxide films formed on the iron-containing magnesium specimens were shown by XPS to contain a higher concentration of oxyen atoms in a "defective" chemical environment.

References

[6.1] J.D. Hanawalt, C.E. Nelson and J.A. Peloubet, Trans. AIME 147 (1942) 273.

[6.2] F.A. Fox and C.J. Bushrod, J. Inst. Metals 70 (1944) 325; 71 (1945) 255.

[6.3] J.E. Hillis, Light Metal Age, June (1983) 25.

[6.4] O. Lunder, T.Kr. Aune and K Nisancioglu, Corrosion 43 (1987) 291.

[6.5] G.V. Raynor, The Physical Metallurgy of Magnesium and its Alloys (Permagon Press, New York, 1959) p.436.

[6.6] V. Mitrovic-Scepanovic, R.H. Packwood, G.J.C. Carpenter and R.J. Brigham, Can. Metall. Quart. 33 (1994) 61.

[6.7] M.G. Fontana and N.D. Greene, Corrosion Engineering, 2nd Edition (McGraw-Hill, New York, 1978).

[6.8] R. Schwoebel, J. Appl. Phys. 34 (1963) 2776.

[6.9] S.F. Lu, M.E.Sc. Thesis, The University of Western Ontario, 1992.

[6.10] J.K. Nørskov, Surf. Sci. 299/300 (1994) 690.

[6.11] D.A. King and P. Woodruff (Eds.), The Chemical Physics of Solid Surfaces and Heterogeneous Catalysis, Volume 6 (Elsevier, Amsterdam, 1993).

[6.12] P.A. Thiel and T.E. Madey, Surf. Sci. Rep. 7 (1987) 211.

[6.13] D. Guenzburger and D.E. Ellis, Phys. Rev. B 45 (1992) 285.

[6.14] F.P. Fehlner and N.F. Mott, Oxid. Met. 2 (1970) 59.

[6.15] E.P. Gusev and A.P. Popov, Surf. Sci. 248 (1991) 241.

[6.16] R. Smoluchowski, Phys. Rev. 60 (1941) 661.

[6.17] V. Mitrovic-Scepanovic, A Fundamental Corrosion Study of Magnesium: Progress Report No. 4 (MTL-CANMET, Report # MTL 91-12, 1991).

[6.18] D. Riegel, L. Büermann, K.D. Gross, M. Luzik-Bhadra and S.N. Mishra, Phys. Rev. Lett. 61 (1988) 2129; 62 (1989) 316.

[6.19] B. Henderson and J.E. Wertz, Defects in the Alkaline Earth Oxides (Taylor and Francis, London, 1977).

[6.20] A. Benninghoven, F.G. Rüdenauer and H.W. Werner, Secondary Ion Mass Spectrometry (J. Wiley and Sons, New York, 1987).

[6.21] D. Briggs and J.C. Rivière, in D. Briggs and M.P Seah (Eds.), Practical Surface Analysis, Volume1, Second Edition (J. Wiley and Sons, Chichester, 1990) p.85.

[6.22] G. Timmer and G. Borstel, Phys. Rev. B 43 (1991) 5098.

[6.23] R. Rofagha, S.J. Splinter, U. Erb and N.S. McIntyre, Nanostruc. Mater. 4 (1994) 69.

CHAPTER 7

SUMMARY OF RESULTS

The initial interaction of water vapour with polycrystalline magnesium and magnesium alloy surfaces has been quantitatively followed from the earliest stage using Auger electron spectroscopy (AES) and X-ray photoelectron spectroscopy (XPS).

The fitting of AES data to theoretical models suggested that the initial reaction of water vapour with pure magnesium surfaces results in a three-stage oxidation behaviour: (1) dissociative chemisorption during exposures up to $\approx$ 0.7 L; (2) oxide nucleation and growth by islands which is complete by 5 L at an average oxide island height of four monolayers of MgO; and slow, bulk oxide thickening following coalescence of the islands. The rate of oxygen uptake was found to be faster on more open-packed, higher index grain faces than on near-basal grain faces, particularly during the oxide nucleation and growth stage. The slow growth stage was monitored by XPS and was found to be adequately described by a logarithmic-type growth expression. The limiting oxide thickness was found to be approximately 11 monolayers of MgO. The effect of pressure on the rate of bulk oxide thickening was determined to be negligible, suggesting that the slow growth process is controlled by the diffusion of metal cations from the metal/oxide interface to the oxide/gas interface. Detailed XPS spectra showed the presence of two distinct types of oxygen in the thin oxide films. One of these was assigned to oxygen atoms in a normal MgO lattice position, whereas the other was ascribed to oxygen atoms in a "defective" chemical environment. Hydrogen (deuterium)

levels in the oxide films were measured by nuclear reaction analysis (NRA) and were found to be relatively low. The role of hydrogen in the film was suggested to be the provision of structural flexibility, leading to the growth of a "defective" oxide.

The influence of prior Ar^+ ion bombardment on the initial interaction of water vapour with pure magnesium surfaces was systematically studied by AES. It was estabilished that the effect of ion bombardment was most pronounced for the oxide nucleation and growth stage of the oxidation process. The dissociative adsorption and final bulk thickening stages were found to be only weakly affected by the level of prior ion bombardment. The results were interpreted based on the assumption that competition exists between the effects of radiation-induced defects (vacancies, vacancy-clusters, dislocation loops) and implanted argon atoms on the oxidation process. The effect of vacancy-type defects was speculated to be the provision of adsorption sites of high sticking probability and nucleation sites of reduced activation energy for place exchange and subsequent island growth. The effect of implanted argon atoms was speculated to be the blocking of adsorption and nucleation sites and interference with oxide island ordering. At relatively high water exposures (20 L) there was enhanced penetration of oxygen into the magnesium lattice postulated to occur along dislocation emergence points. No such enhanced penetration was observed for shorter water exposures (0.3L). The limiting thickness of the oxide layer formed on magnesium at room temperature was not found to be affected by the level of prior ion bombardment. The influence of ion-induced defects thus appeared to be confined to the first layers of growing oxide.

The interaction of water vapour with two polycrystalline Mg-Al alloy surfaces, Mg-3.0wt%Al and Mg-8.5wt%Al, was found to result in a three-stage oxidation behaviour, similar to that observed on pure magnesium. AES lineshape analysis indicated that water vapour dissociates on Mg-Al surfaces, leading to the simultaneous adsorption of oxygen atoms on both Mg and Al atoms present on the surface. Modelling results suggested that the rate of oxide nucleation and growth was enhanced on Mg-Al surfaces compared to on pure Mg surfaces, particularly at higher Al contents. In addition, it was found that magnesium oxide islands were preferentially nucleated at Mg-rich regions and subsequently grew to cover the mixed Mg-Al-O chemisorbed precursor layer. At longer exposures, XPS indicated that Al^{3+} ions were incorporated into the growing oxide film, resulting in an increased activation energy for ion movement and a pronounced decrease in the rate of bulk thickening. The surface concentration of aluminum was observed to decrease slowly during the bulk thickening regime. The results were adequately interpreted based on the Cabrera-Mott theory of low temperature oxidation.

The reaction of water vapour with magnesium specimens deliberately contaminated with very low levels of iron (120 to 700 wt ppm) was shown to be retarded during the very early stages. The influence of iron on the uptake of oxygen on magnesium surfaces was not found to be a clear function of iron concentration. This was likely due to the fact that the solubility limit of iron in magnesium ($\approx$ 55 wt ppm) was exceeded in each specimen, suggesting that the inhomogeneous nature of the iron distribution strongly influences the oxidation process. The growth rate at longer

exposures was unaffected by the iron content. Segregation of iron into the oxide film was, however, detected by static secondary ion mass spectrometry (SSIMS). Finally, the saturated oxide films formed on Fe-containing magnesium specimens were shown by XPS to be more "defective" than those formed on pure magnesium.

APPENDIX A

CALCULATION OF IMFP AND ESCAPE DEPTHS OF VARIOUS AUGER AND PHOTOELECTRONS

The inelastic mean free path (IMFP), λ_o, and corresponding escape depth, λ, of the various Auger and photoelectrons of interest to this thesis were calculated using the empirical expressions of Tanuma et al. [A.1]. It is known that the IMFP of electrons in solids is strongly dependent upon the kinetic energy of the electrons and weakly dependent upon the material in which the electrons move [A.2]. The IMFP dependence on energy is usually described by the Bethe equation for inelastic scattering in matter [A.3]:

$$\lambda_o = \frac{E}{E_p^2 \beta \ln(\gamma E)} \qquad \text{(A.1)}$$

where E is the electron energy (eV); β and γ are empirical parameters (see below); and E_p is a material-dependent term, the free-electron plasmon energy (eV). E_p can be calculated using the following expression:

$$E_p = 28.8\ (N_v \rho / M)^{1/2} \qquad \text{(A.2)}$$

where N_v is the number of valence electrons per atom or molecule; ρ is the bulk density (g/cm^3); and M is the atomic or molecular weight. Tanuma and coworkers then modified the Bethe equation by the addition of two terms as proposed by Inokuti [A.4] and Ashley [A.5]:

$$\lambda_o = \frac{E}{E_p^2[\beta \ln(\gamma E) - (C/E) + (D/E)^2]} \tag{A.3}$$

where C and D are two additional parameters. These added terms account in an empirical way for exchange effects expected to be significant at low energies and for other departures from the first Born approximation on which the Bethe equation is based [A.4]. The four parameters in equation (A.3) were then empirically related to material parameters by fitting calculated and measured IMFP data for 27 elements and 15 inorganic compounds over the 50 to 2000 eV range, yielding the following:

$$\beta = -0.0216 + 0.944/(E_p^2 + E_g^2)^{1/2} + 7.39\times10^{-4}\rho \tag{A.4}$$

$$\gamma = 0.191\rho^{-0.50} \tag{A.5}$$

$$C = 1.97 - 0.91(N_v\rho/M) \tag{A.6}$$

$$D = 53.4 - 20.8(N_v\rho/M) \tag{A.7}$$

where E_g is the band-gap energy for non-conductors (eV).

In order to calculate the IMFP of the various electrons of interest to this study, therefore, equations (A.2) to (A.3) were used with the appropriate material parameters for MgO [A.6]: ρ = 3.58 g/cm^3; M = 40.31 g/mol; N_v = 8; E_g = 7 eV. The results are presented in Table A.1. The appropriate escape depths, λ, were then easily determined using equation (2.4) (Chapter 2) for the instrument geometries. In this work, the electron take-off angle with respect to the surface normal, θ, was 54.5° for the AES experiments and 55° for the XPS experiments. To convert the λ values to ML of oxide, the thickness of one monolayer of MgO was assumed to be equal to the Mg-O bond distance, 0.211 nm [A.7]

Table A.1: Calculated IMFP's and escape depths (λ) for various Auger and photoelectrons in MgO.

	Mg(LVV) AES	Mg(KLL) AES	Al(LVV) AES	O(KLL) AES	Mg(2p) XPS	O(1s) XPS
IMFP (nm)	0.57	2.7	0.59	1.4	3.1	2.3
λ (nm)	0.33	1.6	0.34	0.83	1.8	1.3

References

[A.1] S. Tanuma, C.J. Powell and D.R. Penn, Surf. Interface Anal. 17 (1991) 911.

[A.2] S. Hoffmann, in: D. Briggs and M.P. Seah (Eds.), Practical Surface Analysis, Volume 1, Second Edition (J. Wiley and Sons, Chichester, 1990) p.

[A.3] H. Bethe, Ann. Phys. 5 (1930) 325.

[A.4] M Inokuti, Rev. Mod. Phys. 43 (1971) 297

[A.5.] J.C. Ashley, J. Electron Spectrosc. 46 (1988) 199.

[A.6] R.C. Weast (Ed.), Handbook of Chemistry and Physics, 54th Edition (CRC Press, Cleveland, 1973).

[A.7] S.A. Flodström and C.W.B. Martinsson, Surf. Sci. 118 (1982) 513.